Two and three dimensional electron backscattered diffraction analysis of solid oxide cells materials

Saowadee, Nath

Publication date:
2013

Document Version
Publisher's PDF, also known as Version of record

Two and three dimensional electron backscattered diffraction analysis of solid oxide cells materials

Nath Saowadee

7/12/2013

Energy conversion and storage department
Technical University of Denmark

Summary

There are two main technique were developed in this work: a technique to calculate grain boundary energy and pressure and a technique to measure lattice constant from EBSD. The techniques were applied to Nb-doped Strontium titanate (STN) and yttria stabilized zirconia (YSZ) which are commonly used in solid oxide fuel cell and electrolysis cell. Conductivity of STN is one of the important properties that researchers desire to improve. Grin boundary conductivity contributes to the overall conductivity of the STN. Grain boundary density controlled by mainly grain growth in material processing. Grain boundary migration in grain growth involves grain boundary mobility and net pressure on it. Thus grain boundary energy and pressure of STN were calculated in this work.

Secondary phase is undesired in STN and YSZ synthesis. The secondary phase in ceramics with the same compounds can have different lattice structure. In this case, lattice parameters analysis aid to differential the secondary phases. However lattice constant of secondary phase cannot measure by general tools such as x-ray diffraction due to its insufficiency. Point analysis in electron backscattered diffraction (EBSDX allows measuring the lattice constant. Both 2D and 3D EBSD were used in acquiring microstructure and crystallographic information of STN and YSZ.

Prior to EBSD data collection, effect of FIB milling on STN and YSZ was investigated to optimize EBSD data quality and acquisition time for 3D-EBSD experiments by FIB serial sectioning. Band contrast and band slope were used to describe the pattern quality. The FIB probe currents investigated ranged from 100 to 5000 pA and the accelerating voltage was either 30 or 5 kV. The results show that 30 kV FIB milling induced a significant reduction of the pattern quality of STN samples compared to a mechanically polished surface but yielded a high pattern quality on YSZ. The difference between STN and YSZ pattern quality is thought to be caused by difference in the degree of ion damage as their backscatter coefficients and ion penetration depths are virtually identical. Reducing the FIB probe current from 5000 to100pA improved the pattern quality by 20% for STN but only showed a marginal improvement for YSZ.

On STN, a conductive coating can help to improve the pattern quality and 5 kV polishing can lead to a 100% improvement of the pattern quality relatively to 30 kV FIB milling.

According to the study results a new technique to combine a high kV FIB milling and low kV polishing was developed for 3D-EBSD experiments of STN. A low kV ion beam was successfully implemented to automatically polish surfaces in 3D-EBSD of La and Nb-doped strontium titanate of volume 12.6x12.6x3.0 µm. The key to achieving this technique is the combination of a defocused low kV high current ion beam and line scan milling. The polishing performance in this investigation is discussed, and two potential methods for further improvement are presented.

La and Nb-doped strontium titanate (STLN) with different La contents (La = 0.000, 0.005, 0.01 and 0.02 mol%) are used in grain boundary energy and pressure calculation. 3D-EBSD of the four STLNs were collected. According to largeness of grain size in STLNs (La = 0.000 and 0.005 mol%), 3D-EBSD data of the sample contain in sufficient grains for calculation of gain boundary energy and pressure, thus only 3D-EBSD data of STLNs (La = 0.001 and 0.02 mol%) were used in the calculation. Relative grain boundary energy of STLN (La = 0.02 mol%) was successfully calculated. However in STLN (La = 0.01 mol%) the calculation was not success due to insufficiency of grain boundaries for the calculation.

In lattice constant measurement, lattice constants of cubic STN and cubic YSZ in STN-YSZ binary mixture samples were successfully measured from EBSPs collected at SEM 10 kV and EBSD detector distant 35.527 mm. The measurement error compare to the lattice constant measure from XRD peaks is in the order of 0.01 - 0.67%. Precision of lattice constant measurement by this method is limited mainly by censor resolution of EBSD detector. For a Nordlys S™ EBSD detector (Oxford Instruments, Hobro DK) used in this experiment the precision limit is in the order of 0.03-0.04 Å. The precision is not enough detect the lattice constant difference of STN and YSZ in each samples. Although both the techniques are partly success in applying to analyze STN and YSZ it will be an interesting task for future development.

Papers included in this thesis

Chapter 2 Saowadee N., Agersted K. & Bowen J.R. (2012) Effects of focused ion beam milling on electron backscatter diffraction patterns in strontium titanate and stabilized zirconia. J. Microsc. 246, 279-286.

Chapter 3 Saowadee N., Agersted K. Ubhi S. & Bowen J.R. (2012) Ion beam polishing for three dimensional electron backscattered diffraction. J. 349, 30-40.

Contents

Chapter 1. Introduction

1.1 Strontium titanate as solid oxide cells electrodes backbone

There are general requirement features for anode as following list (S.C. Singhal, K. Kendall., 2003).

- *Catalytic activity*: The anode must have high catalytic activity for electrochemical oxidation of fuel.
- *Impurity*: The anode should be tolerant to certain levels of contamination, especially sulphur which are commonly present in the fuel gas.
- *Stability*: The anode must be chemically morphologically and dimensionally stable under the fuel environment and at the operating temperature.
- *Conductivity*: High electric conductivity to reduce ohmic loss at the anode.
- *Compatibility*: It is need to be chemically thermally and mechanically compatible with other cell components.
- *Porosity*: High porosity is need for fuel transportation to reaction site.

Despite the success of the Nikle-Yttria stabilised zirconia (Ni-YSZ) anode it still has some drawbacks. Sulphur poison is a serious problem of the Ni-YSZ anode. During redox cycle nickel oxidized rapidly and form nickel oxide particles in the anode. These particles cause the cell degradation by blocking reaction sites (STEELE *et al*., 1988) and can crack the cell when it grown up (Klemenso *et al*., 2005). Alternative candidate of anode materials are perovskite base materials. A ceramic composite with doped strontium titanate and doped ceria sintering at high temperature, have been reported promising electrocatalytic and conductivity (Marina *et al*., 2002,Tsipis & Kharton., 2008). The doped strontium titanate composite anodes are tolerant to oxygen carbon and sulphur containing atmospheres with promising electrocatalytic performance similar to Ni-YSZ (Blennow., 2007). The doped strontium titanate materials have also been shown dimensional phase stable during redox cycle (Blennow., 2007).

Figure 1-1 illustrates a novel design anode utilising Nb-doped $SrTiO_3$ (STN) as backbone structure on YSZ electrolyte and Gd-doped ceria (CGO) nano particles infiltrated on the backbone surface. The main function of the backbone is to transport electron to reaction sites. CGO nano particles function is to improve catalytic performance and ionic transport to reaction

sites. STN has been reported high electronic conductivity at the level suitable for and anode backbone material (Blennow *et al*., 2008) has promising redox stability and thermal expansion coefficient math to YSZ (Blennow *et al*., 2009). However improvement of STN performance is still in research.

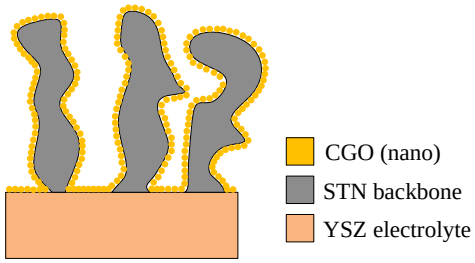

Figure 1-1 A novel anode design with STN as backbone structure and CGO nano particles infiltrated on the backbone surface.

1.2 Conductivity of STN

Conductivity of STN is one of the important properties that researchers desire to improve. Conductivity of polycrystalline material is controlled by both bulk conductivity and grain boundary conductivity (Abrantes *et al*., 2000). In large grains polycrystalline materials the conductivity is controlled by the bulk conductivity while in small grains polycrystalline materials grain boundary conductivity contributes in the materials conductivity (Abrantes *et al*., 2000). Abrantes (Abrantes *et al*., 2002) reported that overall conductivity of dense strontium titanate decreases markedly with increasing average grain size. Thus reverting the trend observed in oxidizing conditions. This suggests enhanced charge transport along multiple grain contacts in parallel with charge transport in the bulk. Therefore the conductivity of the STN in some degree can be manipulated by means of its grain size.

The final grain size in material processing is usually controlled by grain growth and optionally recrystallisation. Grain boundary migration and diffusion is the main process in grain growth and recrystallisation. Grain boundary migration rate is controlled by several parameters such as grain boundary misorientation grain boundary morphology experimental condition and

point defection (Humphreys & Hatherly., 2004). Comprehension in grain boundary migration in STN leads to a better control of the grain growth in the STN. A grain boundary moves with a velocity in response to net pressure on the boundary and mobility of the grain boundary (Humphreys & Hatherly., 2004). The mobility is temperature dependent and is usually found to obey an Arrhenius relationship. The driving pressure (p) is provided by the Gibb-Thomson relation ((Porter & Easterling., 1992)) : $p = \gamma\kappa$, where γ is grain boundary free energy per unit area and κ is grain boundary curvature. Currently there is no complete theory to explain the grain boundary energy. However it can be measured in relative manner from microstructure and crystallographic information of grain boundaries obtained by using electron backscattered diffraction (EBSD) technique as example (Adams *et al*., 1999) (Li *et al*., 2009) and (Rohrer *et al*., 2010). In this work three dimensional EBSD data of STN is used to calculate the grain boundary curvature the relative grain boundary energy and relative pressure of the STN.

1.3 Secondary phase in STN and YSZ

There are generally undesired secondary phases in STN and YSZ. The secondary phases can be identified by components analysis. However one ceramics compound can have various lattice structures. In this case, lattice parameters analysis aid to differential the secondary phases. However lattice constant of secondary phase cannot measure by general tools such as x-ray diffraction due to its insufficiency. Point analysis in EBSD allows measuring the lattice constant. Thus this work also investigates the possibility to measure lattice constant from EBSD data.

1.4 Electron backscattered diffraction

EBSD is a technique which allows crystallographic information to be obtained from crystalline samples in the scanning electron microscope (SEM). Electron backscattered diffraction pattern (EBSP) was first found in 1928 by Nishikawa and Kikuchi (Nishikawa & Kikuchi., 1928). The kinematic model describing formation of the pattern was first purposed by Kikuchi thus it is also called *Kikuchi pattern*. In 1954 Alam et al. (ALAM *et al*., 1954) used a cylindrical specimen chamber and film camera to produce high-angle Kikuchi patterns from

cleaved LiF, KI, NaCl, PbS_2 crystals. The technique became realisable in material analysis in 1992 when Dingley and Randle (Dingley & Randle., 1992) improved the technique by using a low light level TV camera. Figure 1-2 shows diagram of EBSD system components. The components are listed below.

- *Tilted sample*: A crystalline sample is tilted approximately 70° from the horizontal in the SEM chamber to obtain the maximum of backscattered electron intensity.
- *Electron beam:* The beam in the SEM.
- *Phosphor screen*: Phosphor screen is attached in front of a CCD video camera for detecting electron diffraction patterns.
- *CCD video camera*: EBSP on the phosphor screen is capture by CCD camera.
- *Vacuum interface cylinder*: A vacuum interface used for mounting CCD camera in an SEM port. It allows the CCD video camera can be inserted and retracted in the SEM chamber.
- *Electronic hardware:* Electronic hardware for control the electron beam, stage moving, and SEM magnification.
- *Computer:* A computer for controlling EBSD experiments and performing data processing.

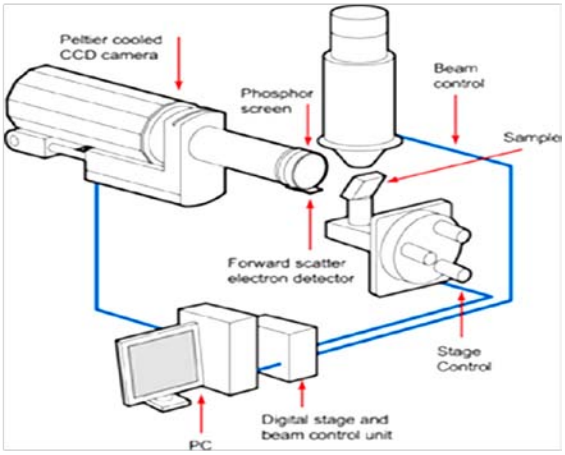

Figure 1-2 Diagram illustrates principal components of an EBSD system. (Oxford Instruments., 2005)

In EBSD, when electron beam hit the sample surface, some the electrons in the beam will penetrate into the sample. The penetration depth depends upon the beam accelerating

voltage, angle of incidence and hardness of the sample. Some of the penetrated electrons can backscatter out of the sample and the rest are adsorbed in the sample. Figure 1-3 shows a casino simulation (Drouin *et al*., 2007) of electron trajectories of 20kV electron beam, the red paths are backscattered electron trajectories. The backscattered electrons that satisfy the Bragg condition (equation 1-1) will interfere and form Kikuchi pattern on the phosphor screen.

$$n\lambda = 2dsin\theta \qquad 1\text{-}1$$

Where *n* is an integer, λ is the electron wavelength, *d* is the spacing of the diffracting planes, and θ is the scattering angle or Bragg's angle. An example of EBSD pattern is shown in figure 1-4. EBSD pattern carry out crystallographic information at the point electron beam hit the specimen. Crystallographic parameters can be related to the Kikuchi bands as described below.

- Each *Kikuchi bands* are formed by backscattered electrons which reflected from different lattice planes. The bands can be indexed by the Miller indices of the reflection plane. The red indices in Figure 1-4 are example of the indices of Kikuchi bands.
- *Kikuchi band width* is related to lattice spacing of the associated reflecting plane.
- *Intersection of Kikuchi bands* is projection of lattice zone axis of the sample on phosphor screen. It can be indexed using the zone axis indices as the white indices in Figure 1.3(a).
- *Number of symmetrical points* in Kikuchi pattern corresponds to number of symmetrical zone axis in specimen's lattice.

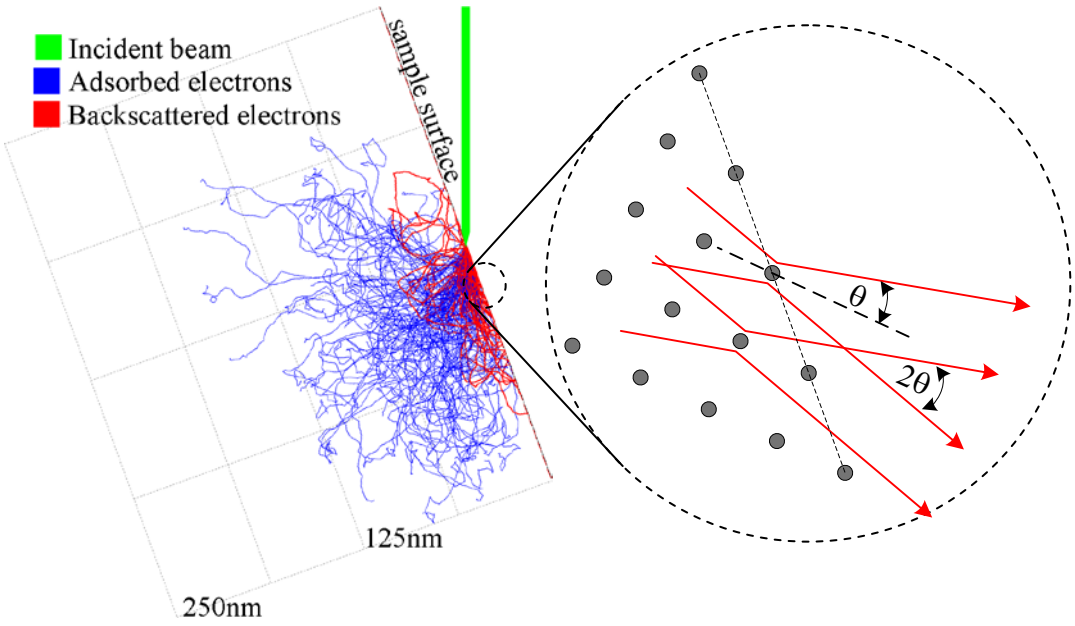

Figure 1-3 Diagram shows Casino simulation of electron beam (20kV) interaction with a specimen ($SrTiO_3$) at incident angle 70°. Trajectories of backscattered electrons are shown in red. The backscattered electrons satisfied Bragg condition form Kikuchi's pattern on phosphor screen.

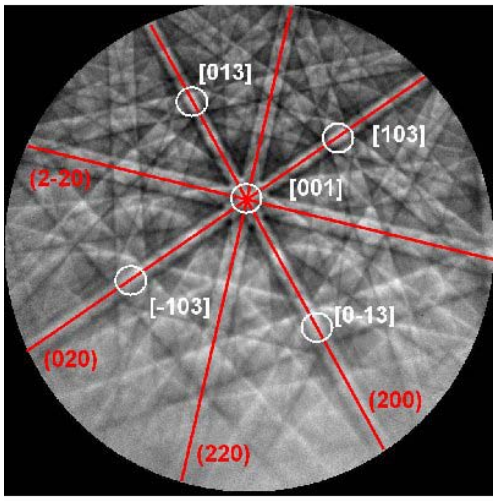

Figure 1-4 An example EBSD pattern with Kikuchi bands indices in red and zone axes indices in white (Oxford Instruments., 2005)**.**

In EBSD technique the acquired EBSD pattern is indexed i.e. Kikuchi bands and zone axes in the EBSP are labelled by Miller indices. The indexed zone axes are used to identify crystal orientation at the point electron beam hit the sample surface. The crystal orientation is utilised in material analysis such as texture analysis, crystal deformation and cracking etc. Automatic indexing allows to extent EBSD experiment from point analysis to areal analysis and volumetric analysis. Currently computer performance is enough to perform real tine automatic indexing. Unit cell parameters and crystallographic space group of specimen are required in EBSP indexing. The requirement unit cell parameters and space group of the material is also call *match unit*.

1.5 Three dimensional EBSD by FIB serial sectioning

Areal or two dimensional (2D) EBSD is widely used in metallic characterisation. Information that is almost missing in 2D-EBSD is the full crystallographic characteristic of interfaces and grain boundary. In 2D-EBSD, misorientation across a boundary can be determined however orientation of the boundary plane cannot be determined. This information is importance for the investigation of phase transformations, grain growth processes, and intergranular fracture (Zaefferer *et al*., 2008). This information can be obtained from three dimensional electron backscattered diffraction (3D-EBSD). Currently 3D-EBSD technique have been undergone intensive development and utilised in material analysis in various groups example as (Bastos *et al*., 2008,Dillon *et al*., 2011,Gholinia *et al*., 2010,Zaefferer *et al*., 2008). In principle, 3D microstructures can be obtain by two different approaches, either by serial sectioning or by observing some sort of transmissive radiation (Zaefferer *et al*., 2008). The latter technique obtains the 3D information either by reconstruction from number images taken in different directions or by a ray tracing technique which allows crystallographic information to be obtained. The serial sectioning method composes two main processes: (1) cutting a material surface by some cutting techniques and (2) recording microstructure data on the surface. Reconstructing the 3D structure can be done by stacking the recorded 2D data. Serial sectioning is applicable to a very wide range of materials the only serious disadvantage is that the method is destructive.

Serial sectioning can be done by various methods, for example mechanical cutting, grinding, polishing, chemical polishing laser or electrical discharge ablation and ion beam milling. The most convenient method seems to be implementing of focus ion beam (FIB) since the FIB is integrated in almost modern model of electron microscope. The most advantage of using FIB milling for serial sectioning is slices cutting can be done in the electron microscope chamber consequently the data collection can be continued without taking the sample off the microscope chamber. Moreover positions realignment and slice thickness are easier to control. Figure 1-5 shows sample stage positions in 3D-EBSD data collection by FIB serial sectioning of Oxford Instruments HKL and Carl Zeiss 3D-EBSD on CrossBeam® system. Data collection starts by moving the sample to the FIB milling position and start milling. Then the sample is moved to data acquisition position to collect data and the cycle is continued. A pre-tilted sample holder is used to decrease stage tilting during changing position that might cause accident inside the chamber.

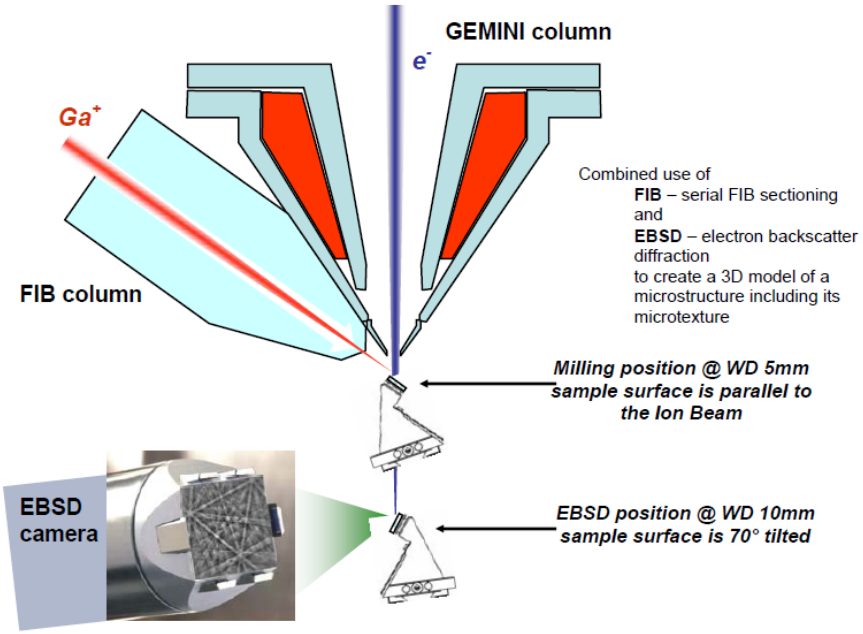

Figure 1-5 specimen stage positions in 3D EBSD data collection by FIB serial sectioning (Oxford Instruments HKL and Carl Zeiss 3D EBSD on CrossBeam® manual).

Figure 1-6 shows a schematic of the sample geometry in 3D-EBSD data collection by FIB serial sectioning. A cross marker created by FIB milling, is used for position realignment both milling and data collection positions. In Figure1-6, the red arrow indicates the FIB direction when the sample is at milling position and the blue arrow indicates the electron beam direction when the sample is at EBSD position. The dash rectangle is the EBSD mapping area. Material surrounding the area must be extra removed to prevent shadowing of the backscattered electron.

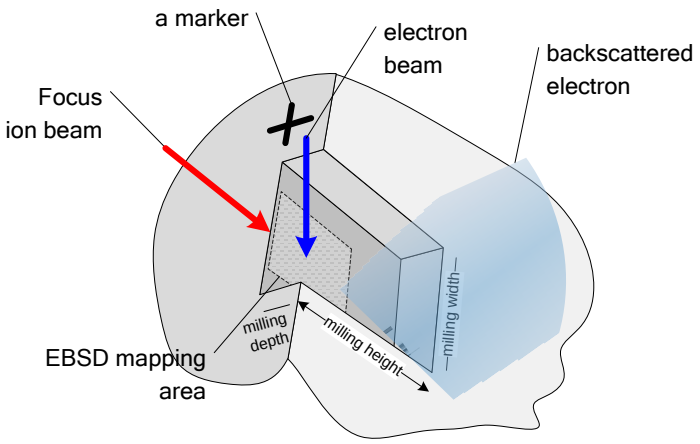

Figure 1-6 Schematic illustrates sample geometry in 3D EBSD data collection by FIB serial sectioning.

1.6 Material issues in 3D-EBSD by FIB serial sectioning

There are three important issues to be considered in 3D-EBSD system: spatial resolution, angular resolution and maximum volumes of observation with regard to the long-term stability of the instrument (Zaefferer *et al*., 2008). Material of investigation is another important issue to be considered. It is well known that FIB milling is inherently destructive to the specimen. FIB milling create amorphous layer on the milling surface and the amorphous layer reduces the intensity of back scattered beam. The amorphous layer can be reduced using low-kV ion beam polishing. This method is used in TEM sample preparation however no report on using the method in 3D-EBSD found, to the date.

In ceramics there are some challenges in performing EBSD. Charging is the most serious problem. YSZ one of the materials used in this study is principally electronic in-conductive.

Charge can be cumulated on the YSZ surface during EBSD experiment. The surface charge can obscures both SEM imaging and EBSD signal. The charge can also drift electron beam and yield distortion on EBSD mapping. Conductive coating can reduce the charging but the outcome backscattered electron intensity is reduced. In 3D EBSD by FIB serial sectioning the coating is removed by FIB milling of the first section. However the coating technique has shown that it is applicable to 3D-EBSD data collection on Nd_2O_3 doped alumina (Dillon & Rohrer., 2009), YSZ (Dillon & Rohrer., 2009,Helmick *et al*., 2011) and LSM-YSZ(Dillon *et al*., 2011). Operation at low kV is another method to reduce the charging however it needs a significantly longer time in EBSD data collection. Complexity of lattice structure is another issue to consider. Some ceramics have more than one crystallographic form but the same or nearly the same chemical composition. This leads to difficulty in select match unit. The complication can lead to data analysis trouble such as pseudosymmetry in rectangular lattice structure. Since the materials in this study are ceramics and ceramics compound the effect of FIM milling damage surface charging need to be investigated prior to 2D-EBSD and 3D-EBSD data collection.

1.7 Crystallographic structure of STN and YSZ

As mention before crystallographic information needed for creation match unit is space group and unit cell parameters (or lattice constants). The most important requirement in indexing is space group. The lattice constant can be varied to temperature and doping as long as its crystal structure still unchanged the same match unit can be used. Summary of space groups and lattice constants of STN and YSZ are provided in Table 1-1.

Table 1-1 summary of space groups and lattice constants of STN and YSZ

Materials	**Space group**	**Lattice constants**	**Temperature**
$SrTiO_3$ (*Cubic*)	221 ($pm\bar{3}m$)	a = 3.901Å	296 K
(Abramov *et al*., 1995)			
$SrTi_{0.875}Nb_{0.125}O_3$ (*Cubic*)	221 ($pm\bar{3}m$)	a = 3.9237Å (Rietveld)	300 K
(Page *et al*., 2008)		a = 3.9255Å (PDF)	
$Zr_{0.90}Y_{0.10}O_{1.95}$ (*Tetragonal*)	137 (P 42/n m c)	a = 3.6183Å c = 5.1634Å	293 K
$Zr_{0.88}Y_{0.12}O_{1.94}$ (*Tetragonal*)	137 (P 42/n m c)	a = 3.6228Å c = 5.1575Å	
$Zr_{0.86}Y_{0.14}O_{1.93}$ (*Tetragonal*)	137 (P 42/n m c)	a = 3.6258Å c = 5.1514Å	
(*Cubic*)	225 ($Fm\bar{3}m$)	a = 5.1370Å	
$Zr_{0.84}Y_{0.16}O_{1.92}$ (*Cubic*)	225 ($Fm\bar{3}m$)	a = 5.14086Å	
$Zr_{0.82}Y_{0.18}O_{1.91}$ (*Cubic*)	225 ($Fm\bar{3}m$)	a = 5.14335Å	
$Zr_{0.80}Y_{0.20}O_{1.90}$ (*Cubic*)	225 ($Fm\bar{3}m$)	a = 5.14728Å	
$Zr_{0.78}Y_{0.22}O_{1.89}$ (*Cubic*)	225 ($Fm\bar{3}m$)	a = 5.15093Å	
(YASHIMA *et al*., 1994)			

1.8 Thesis outline

In this work 2D-EBSD and 3D-EBSD by FIB serial sectioning were utilised in microstructure characterisation of STN and YSZ. FIB milling is used in both 2D-EBSD surface preparation and 3D-EBSD data collection. Since the FIB is inherently destructive to the specimen, FIB damage on STN and YSZ was investigated primarily. The investigation result will be later used in design of both 2D-EBSD and 3D-EBSD experiments. The detail of FIB damage investigation on STN and YSZ is presented in Chapter 2.

A technique to improve EBSD signal quality is developed for data collection of the specimen that has heavily damaged from FIB milling. The technique utilises low KV ion beam to improve the ENSD signal. Detail of the technique and it application on 3D-EBSD experiment is presented in Chapter 3.

In Chapter 4, a technique to measure lattice constant from was developed and applied to STN and YSZ samples. The advantage of this technique is that it's point analysis and can be

apply to secondary phase which has low amount in the sample since peaks of such secondary will not appear in other technique such as X-ray diffraction technique.

3D-EBSD data of STN samples were collected using the technique. Microstructures of the STNs were primarily investigated in both 2D-EBSD and 3D-EBSD. This content is presented in Chapter 5.

A grain boundary geometry analysis method was developed to calculated grain boundary curvature, relative grain boundary energy and grain boundary pressure of STN sample. Detail of the technique and calculation results are presented in Chapter 6. Chapter 7 is outlook of this work.

Chapter 2. Effects of focused ion beam milling on electron backscatter diffraction patterns in strontium titanate and stabilised zirconia

2.1 Introduction

The most significant challenge to performing three dimensional electron backscattered diffraction (3D-EBSD) on ceramics is specimen charging due to low electronic conductivity at room temperature. In 2D-EBSD this problem can be circumvented simply by coating the specimen with conductive material. Coating samples prior to 3D-EBSD investigations is somewhat thwarted due to the fact that the coated material will be removed after focus ion beam (FIB) milling the first slice. However this technique has shown that it is applicable to acquire 3D-EBSD data of low electric conductive ceramics such as (Nd_2O_3) doped alumina (Dillon & Rohrer., 2009), YSZ (Dillon & Rohrer., 2009,Helmick *et al*., 2011) and LSM-YSZ (Dillon *et al*., 2011). They also commented that gallium contamination and the conductive coating surrounding the working area might contribute to reduce charging from the working surface.

Another issue that requires consideration is EBSD pattern quality. It is well known that ion beam milling causes surface amorphisation (Rubanov & Munroe., 2005) and results in ion implantation at the surface. The thickness of this layer in comparison to the electron beam interaction volume will determine the extent to which the EBSP quality is reduced compared to the crystal lattice of the bulk (Randle & Engler., 2000). It is well known that damage from FIB milling is highly dependent on FIB accelerating voltage. However from the work of Mateescu *et al*. (2007), it has been reported that milling damage also depends on FIB current and it also has a dependence on material.

Apart from surface quality, electron beam accelerating voltage and the degree of sample charging for ceramics also important. In order to reduce sample charging lower accelerating voltages and smaller probe currents are logically desired, however this results in weaker and noisier EBSD patterns. To counteract this, longer frame integration times (i.e. EBSD detector exposure time) or higher frame averaging (i.e. integration of multiple EBSD patterns) is required adding significantly to data collection times – a serious drawback for 3D data collection rates.

In this study we investigate the effects of FIB (and SEM) parameters in terms of pattern quality measurements with a view to performing 3D-EBSD data collection of ceramic materials.

As examples representative of solid oxide fuel/electrolysis cell materials we compare measurements on strontium titanates and yttria stabilised zirconia to the existing literature on FIB damage in metals.

2.2 Pattern quality

The image quality of an EBSP such as band contrast is related to the number of lattice defects within the electron beam interaction volume, the specimen backscatter coefficient, the presence of contaminants/coatings on the specimen surface, and the experimental setup. To determine the FIB milling effect the experimental setup and surface coatings and/or potential contaminants have to be controlled. Furthermore, making comparisons on the same material the effect of backscatter coefficient can be neglected. Lattice defects can arise due to the state of the bulk or by sample preparation processes such as polishing or by ion beam damage due to FIB milling. FIB milling can induce a thin amorphous layer below the milling surface (Rubanov & Munroe., 2005) which can reduce the intensity of the backscattered electrons and yields a lower contrast of Kikuchi bands. Wilkinson and Dingley (1991), also showed that band edge sharpness is related to the degree of deformation of a metallic lattice. The sharpness can be measured as band slope since the sharper band will give the higher slope of the bands edge. Therefore the degree of lattice damage from FIB milling may be observed from contrast and sharpness of Kikuchi bands in an EBSP. The pattern quality parameters of an EBSP can be defined in the following way (Maitland & Sitzman., 2007).

- **Band contrast** is an EBSP quality factor derived from the Hough transform that describes the average intensity of the Kikuchi bands with respect to the overall intensity within the EBSP. The values are scaled to a byte range from 0 to 255 (i.e., low to high contrast).
- **Band slope** is an image quality factor derived from the Hough transform that describes the maximum intensity gradient at the margins of the Kikuchi bands in an EBSP. The values of are scaled to a byte range from 0 to 255 (i.e., low to high maximum contrast difference), i.e., the higher the value, the sharper the band.

The values of band contrast and slope for each EBSD pattern in this work are generated by the commercial software used to acquire the EBSD data.

2.3 Experiment

2.3.1 Materials

Three samples: $Sr_{0.94}Ti_{1.0}Nb_{0.1}O_3$ (STN94), $Sr_{0.99}Ti_{1.0}Nb_{0.1}O_3$ (STN99) and 8% mol yttria stabilised zirconia were used in this investigation. The STN94 and STN99 were synthesised into bulk pellets and by isostatic pressing and were sintered at 1500°C in air for STN94 and in 9%H_2/Ar for STN99. The YSZ was produced by tape casting. The average grain size, measured from EBSP maps, of the STN94 is 2.3 μm and STN99 is 1.2 μm while YSZ grain size is 8.9 μm. The STN94 has a lower conductivity, < 1 S/cm compared to the STN99, ~150 S/cm. YSZ, used as electrolytes in SOFCs has a very low electronic conductivity, in the order of 10^{-7} S/cm at 25°C approximated from work of Hattori et al. (2004). The samples were prepared for EBSD analysis by cutting to pieces of approximately 5x5x1 mm. Each sample was then ground on SiC paper and diamond polished on two faces to a 1 μm diamond finish to create a sharp 90° edge. The YSZ sample was carbon coated with an approximate thickness of 10-18 nm. Half of the STN94 was also coated by the same procedure in order to compare EBSP quality of the coated and uncoated surface after FIB milling.

2.3.2 Microscopy

FIB-SEM and EBSD work was performed on a CrossBeam 1540XB™ (Zeiss, Oberkochen Germany) equipped with an Nordlys S™ EBSD detector (Oxford Instruments, Hobro Denmark). The interior of the microscope chamber illustrating the FIB and EBSD sample positions is shown in Figure 1. Oxford Instruments' software was used for EBSD data collection (HKL Fast Acquisition 1.2) and analysis (Channel 5)

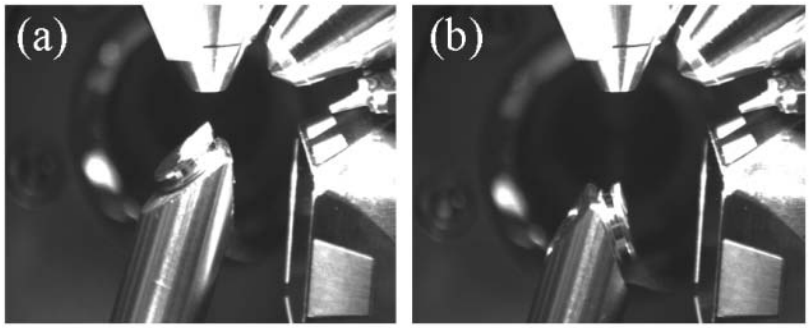

Figure 2-1 Hardware setup, (a) FIB milling position and (b) EBSD position.

2.3.3 Methods

a) Effect of FIB current

To study the effect of FIB current the following standard probe currents were chosen: 5000, 2000, 1000, 500, 200 and 100 pA at an accelerating voltage of 30 kV. Six different places on each sample were milled corresponding to these probe currents. To remove any surface contamination, damage or residual stress induced by the mechanical polishing, pre-milling with 2000 pA was used to remove a layer of 1 μm depth, as shown in Figure 2, prior to milling the surfaces with specific probe currents. These surfaces were created by milling a further 0.5 μm from the 2000 pA surface. EBSD mapping of each surface was performed with a SEM voltage of 20 kV using the 120 μm aperture and high current mode that yields the electron beam current of approximately 10 nA. The surface was mapped by 100x100 pixels with 0.2 μm step size for the STN94 0.4 μm for YSZ and 0.1 μm for the STN99, as the latter had a significantly smaller microstructural scale. EBSD data was collected at an SEM working distance of 15 mm and the EBSD camera was set to the following parameters: Integration Time 24 ms, Pixel Binning 4x4, Gain Amplification low, Frame Averaging 4, Hough Space Resolution 60x60 pixels, and Min-Max Band Detection 6-7. Band contrast and band slope of each EBSD map were measured using HKL Channel 5 Project Manager then the band contrast and band slope of each sample were compared using only indexed data points.

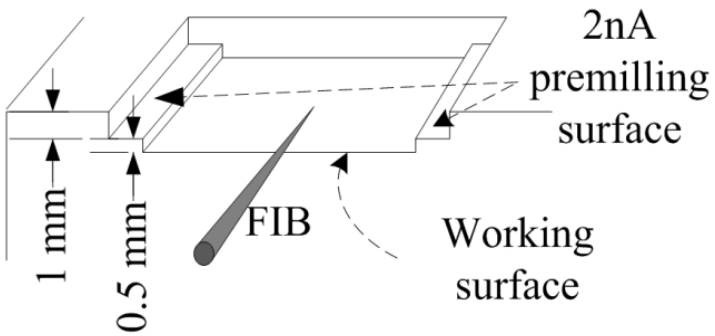

Figure 2-2 Diagram shows milling pattern for FIB damage investigation.

b) Effect of FIB voltage

The effect of FIB voltage on EBSP quality was studied on the STN99 sample. The purpose of this study is to investigate a suitable FIB voltage to perform FIB polishing during automated 3D-EBSD data collection of STN and YSZ based materials. A 5 kV FIB voltage was selected in this study as improvements in EBSP quality after low voltage milling in metals have been reported (Matteson *et al*., 2002; Michael & Kotula., 2008). Surface preparation using 2 kV FIB polishing was also reported to give a better EBSP quality (Michael & Giannuzzi., 2007) however, due to FIB alignment issues and the slow milling rate, 2 kV polishing was not investigated.

Surfaces for EBSD investigation after low kV FIB polishing were milled on the STN99 sample with 2000 pA, 30 kV probe to a 1 μm depth. Then EBSD mapping of each surface was collected using the same acquisition parameters for investigating the effect of FIB current. Subsequently surfaces were milled with a 2500 pA, 5 kV probe. EBSD maps were recollected on the same areas using the aforementioned parameters.

2.4 Results and Discussion

2.4.1 Effect of FIB current

Average band contrast and band slope of all sample are shown in Figures 3 and 4, respectively. Band contrast and band slope are in arbitrary units (0-255) on the vertical axis. The error bars represent one standard deviation of the values over an EBSP map of the indexed pixels only. Inverse pole figure (x-axis) coloured mapping combined with band contrast of STN94, coated-STN94, STN99 and coated-YSZ milling with 2000 pA, 30 kV FIB probe are shown in Figure 5.

The effect of FIB current shown in Figures 3 and 4 reveals that both band contrast and band slope of the STN samples are increased when the FIB current is decreased from 5000 to 100 pA. The band contrast at 100 pA compared to 5000 pA for each STN sample is increased about 20% while band slope is increased by between 9-18%. Although the error bars represent a relatively large spread in pattern quality for each probe current (i.e. the spread between one standard deviation above and below the mean) the mean value shows a consistent trend. The spread in pattern quality also accounts for the lower quality indexed patterns close to the grain boundaries. This is illustrated in Figure 6 where a band contrast line profile is extracted from coated STN94 (see Figure 5(b)). Here, it can be seen that band contrast decreases near grain boundaries and contributes to the spread in their values. The pattern quality is observed to vary approximately linearly as a function of FIB probe current. This trend is different from the observed effect of FIB current on pure metals, reported by Mateescu et al. (2007), where the pattern quality is increases when decreasing the current from 5000 pA to 1000 pA but decreased again at 500-100 pA. In this work no mechanism was concluded for a maximum of pattern quality at 1000 pA. The coated YSZ gives a high pattern quality for all FIB currents in the range 500 pA to 5000 pA compared to the coated STN94. EBSD on uncoated YSZ was not possible due to the heavy charging on its surface and is therefore not reported here.

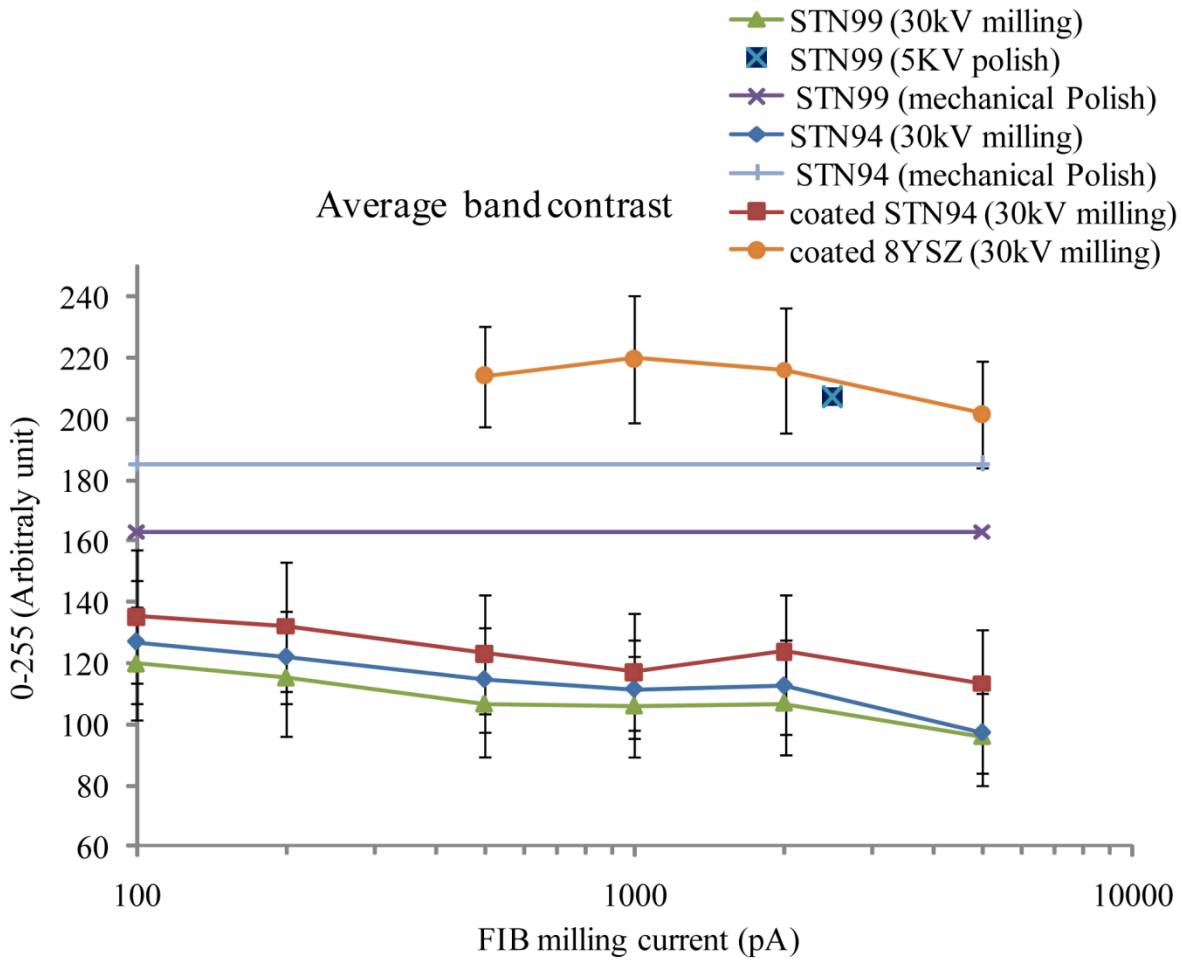

Figure 2-3 Average band contrast at different FIB currents, 100 to 5000 pA, of nonzero solution of STN99, STN94 and YSZ with different surface preparation, i.e. 30 kV FIB milling, 5 kV FIB polishing and mechanical polish.

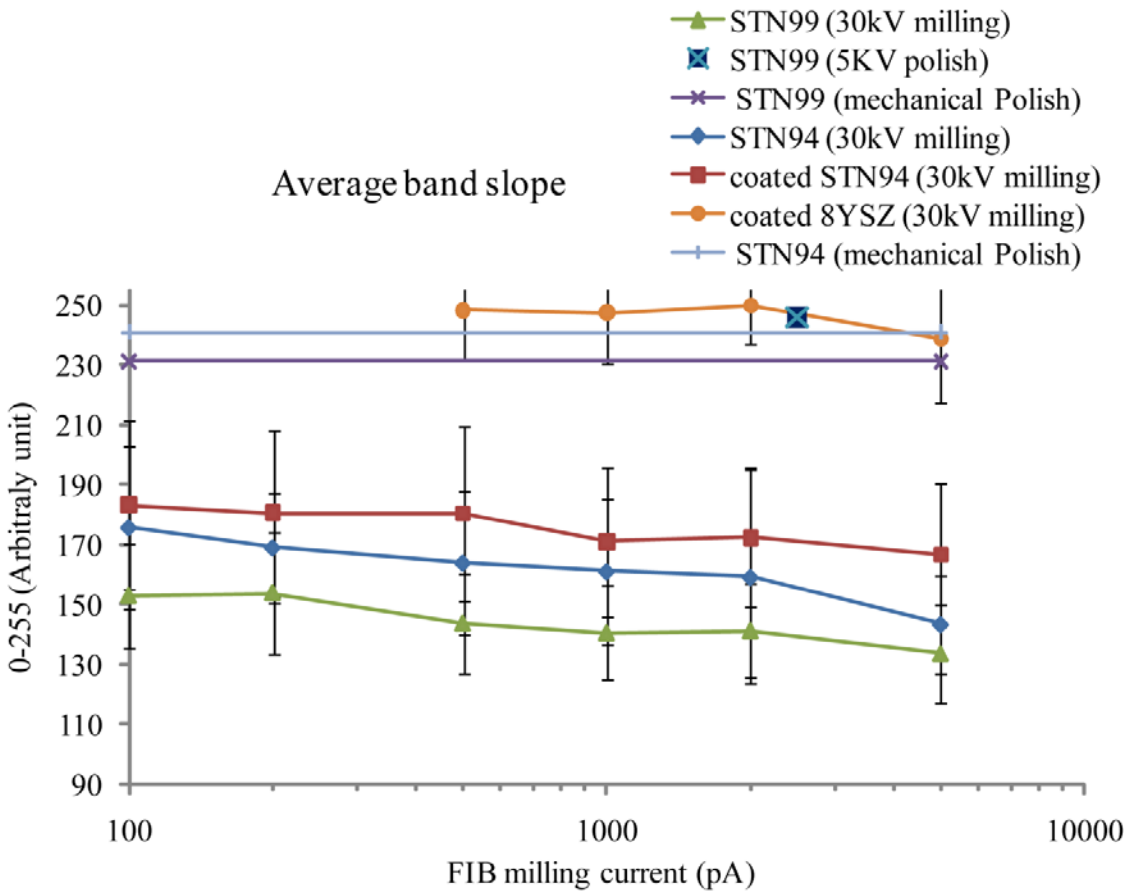

Figure 2-4 Average band slope at different FIB currents, 100 to 5000 pA, of nonzero solution of STN99, STN94 and YSZ with different surface preparation, i.e. 30 kV FIB milling, 5 kV FIB polishing and mechanical polish.

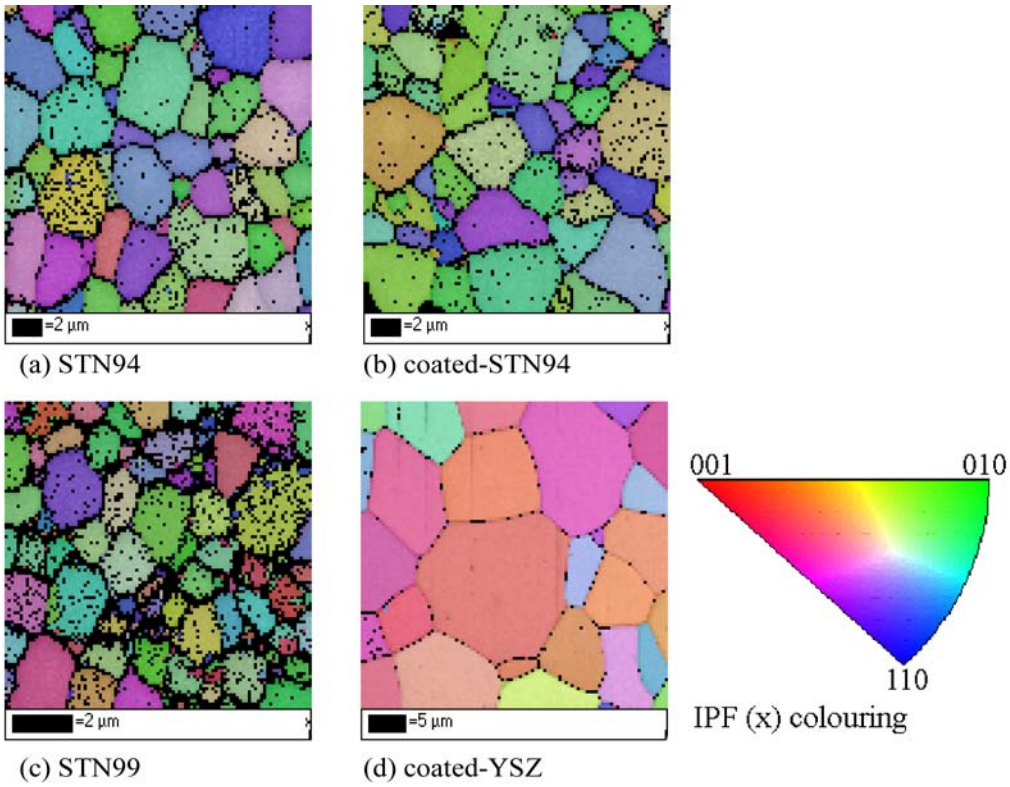

Figure 2-5 Inverse pole figure (x-axis) colour combine with band contrast mappings of STN94 coated-STN94 STN99 and coated-YSZ milling with 2000 pA, 30 kV FIB probe, black dots are non-indexed pixels.

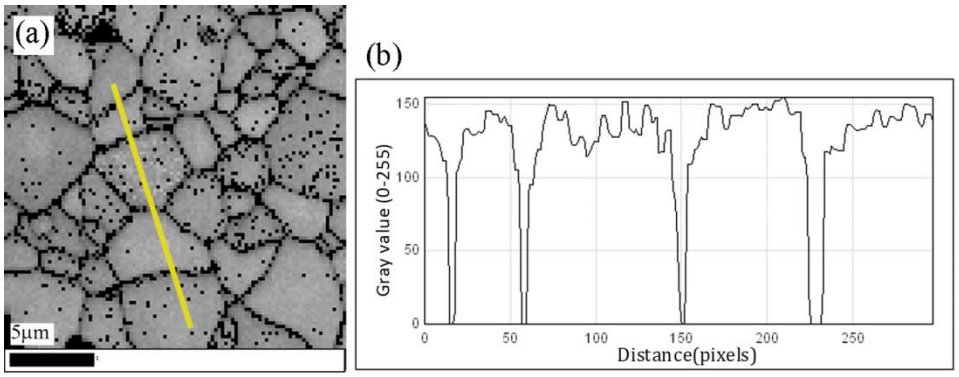

Figure 2-6 (a) Band contrast map of coated STN94 (see Fig. 5b). (b) Band contrast line profile corresponding to line in (a) illustrating reduced band contrast near grain boundaries. Points at grain boundaries with zero band contrast are non-indexed data points.

Figure 7 shows Ga ion penetration Monte Carlo simulations of a low angle beam (1° to the surface, 5000 ions) on STN and YSZ at 30 kV and STN at 5 kV using SRIM simulator (Ziegler et al., 2010). The result as shown in Figure 7, shows no significant difference in the average penetration depth (ion range) of STN (56 Å) and YSZ (54 Å). Although the penetration depths are not significantly different it is not possible to determine the degree of ion induced damage that occurs to the local crystal lattice in the electron beam interaction volume where the EBSPs are generated. The EBSD pattern quality is also generally affected by the combination of the backscattered electron coefficient and the geometric forescattering induced by the inclined specimen. Therefore to investigate this the backscatter coefficients of YSZ and STN were simulated using the Casino simulator (Drouin., 2007). Simulating a 20 kV electron beam inclined at the EBSD tilt angle of 70° to the specimen surface, the backscatter coefficient of YSZ is 0.61 and STN is 0.56. As the difference of the backscatter coefficient between the samples is only 0.05, one would not expect a significant difference in pattern quality. Thus we therefore speculate that the degree of ion damage of the specimen surface is the major contributing factor to the differences observed in the pattern quality as determined by band contrast and band slope. Ion sputtering rates, and by association ion damage, tends to correlate with atomic number, melting point, hardness, density and crystal structure (reference the book Introduction to focused ion beams... by giannuzzi). STN and YSZ show differences in hardness (STN ~25% < YSZ) and melting point (STN ~15% < YSZ) but the difference density (STN ~15% < YSZ) should be accounted for in the SRIM simulations. These differences may account for the effect of ion damage on pattern quality. In order to confirm this hypothesis high resolution transmission electron microscopy of the affected surface would be required to measure the damage depth. This however, is beyond the scope of this work.

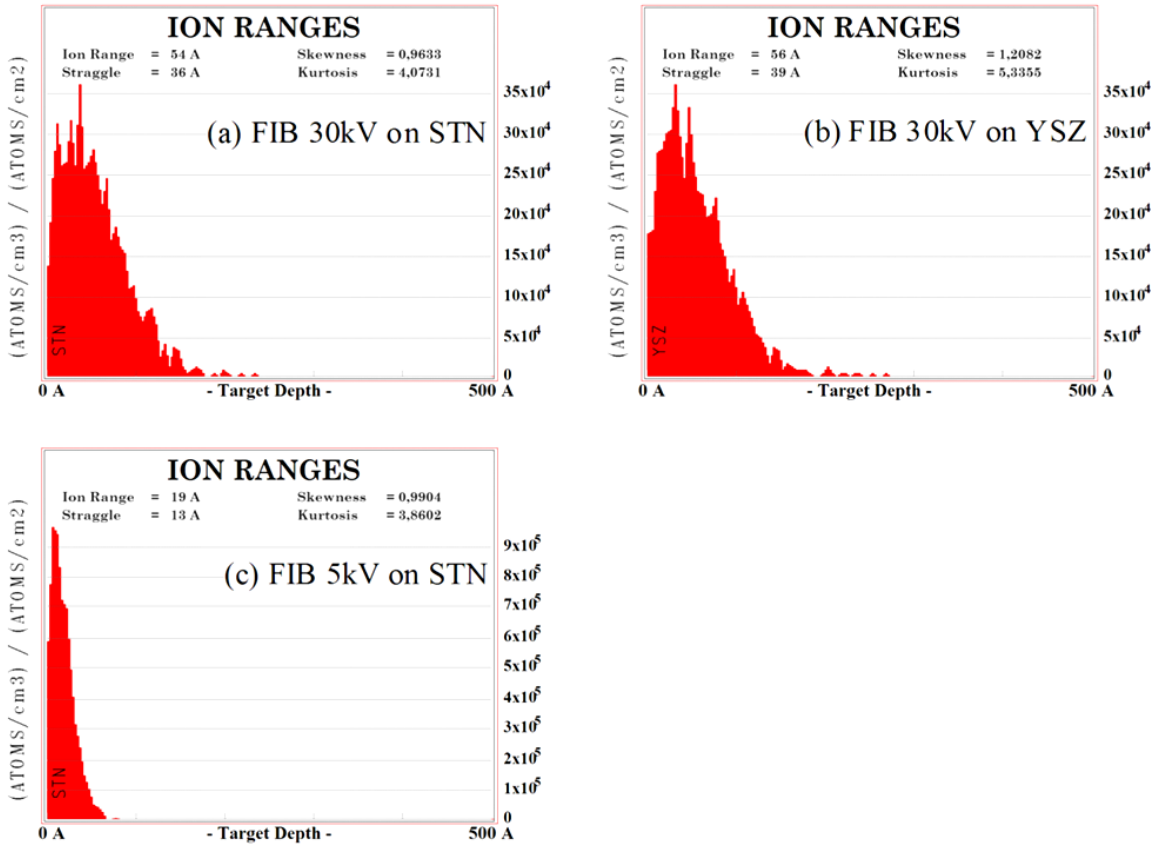

Figure 2-7 Penetration depth of Ga+ with 1◦ incident angle to specimen surface, 30 kV accelerating voltage into STN and YSZ and 5 kV into the STN sample using SRIM simulator.

Comparing the pattern quality of STN94 and STN99 it can be seen that the STN94 has higher band contrast and band slope on both mechanical polished and 30kV milled surfaces at all FIB currents. The coated STN94 also gives a better result than STN94 for all FIB currents. Since STN94 has a very low conductivity, the coating remaining around the milling area (on the top surface and the milling face) is thought help in conducting the build up of charge from the mapped area during EBSD acquisition. It can be seen that there is an anomalously low measurement of the coated STN94 at 1000 pA for both band contrast and band slope compared to neighbouring data points. This is due to the build-up of charge on a milling artefact near the mapping area.

2.4.2 Effect of FIB voltage

The SRIM simulation in Figure 7 shows that the penetration depth of Ga+ ions into STN at 5 kV (18 Å) is obviously smaller than at 30 kV(56 Å). The simulation result supports the results of prior works (Matteson *et al*., 2002; Michael & Kotula., 2008) that high accelerating FIB milling voltage can induce damage deeper than low voltage. Figure 8 shows a band contrast image of the STN99 sample where the surface has been milled with stripes of different milling conditions. The left, centre and right stripes are the original mechanically polished surface. The second stripe from the left was milled with a 30 kV beam followed by polishing with a 5 kV beam. The fourth stripe from the left was milled only with a 30 kV beam. Of the three prepared surfaces the 30 kV milled surface shows the lowest surface quality as can be seen by the relatively lower band contrast(darker grey values). The brightest column according to the highest pattern quality was achieved by the 30 kV milling and 5 kV polishing. In Table 1 it is seen that for the STN99, both pattern qualities and indexing percentage of an EBSD mapping on 30kV milling surface decreased significantly, compared to the mechanically polish surfaces. In the 5kV polished surface, compared to mechanically polished, the band contrast is clearly increased, but band slope and indexing percentage are only marginally increased, which may stem from the fact that both band slope and indexing percentage are already close to the maximum possible values.

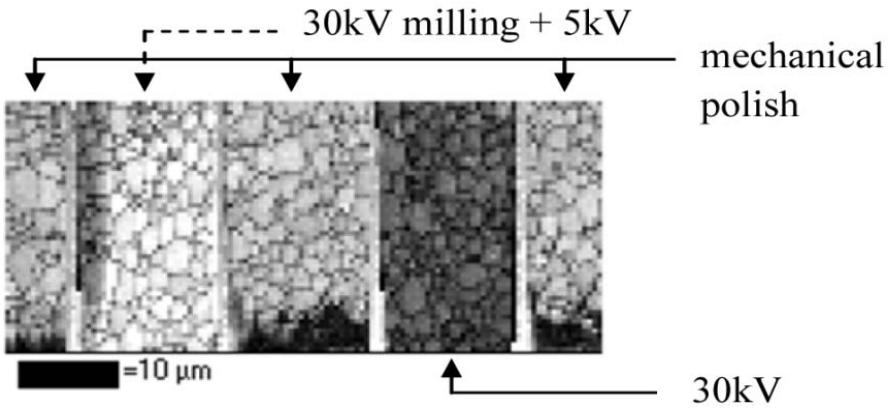

Figure 2-8 Band contrast map of a sample area on the STN99 sample with variously prepared regions. From left to right the 1st, 3rd and 5th stripes are mechanical polished, the 2nd stripe from the left is milled at 30 kV followed by 5 kV polishing and the 4th stripe from the left is a 30 kV milled surface.

Table 2 Comparison of average band contrast band slope and indexing percentage of 30kV, 5kV FIB milling and mechanical polishing surface on STN99.

FIB voltage	Average band contrast	Average band slope	Indexing %
30 kV (2000 pA)	106.9	141.2	69.5%
5 kV (2500 pA)	207.1	244.8	91.4%
Mechanical	162.9	231.1	91.1%

Inverse pole figure (x-axis) colour maps of 30kV 5kV milling and mechanical polish surface of STN99 sample without noise reduction are shown in Figure 9 to illustrate the distribution of the non indexed points. In the 30 kV map non indexed points are distributed over the map both at grain boundaries and inside the grains. It can also be seen that certain grains contain many non-indexed points in the grain interior whilst others are essentially free of non-indexed points suggesting that certain crystal orientations are more sensitive to ion beam damage than others. On the contrary in the 5 kV map almost all non indexed points are confined to the

grain boundaries where non-indexed points are almost always observed in conventionally prepared surfaces such as in the mechanically polished map. Moreover the non-indexed points at grain boundaries in the 30 kV map is significantly more than the 5kV and mechanical polished map. Comparing the 30 kV and 5kV maps, which were acquired from the same area and EBSD conditions, it can be seen that the non-indexed points inside the grains and the additional non-indexed points at the grain boundaries of 30 kV map represent the FIB damage on the surface. From this it can be concluded that a 5 kV beam is sufficient to remove high kV milling damage and restore the surface quality to at least or better than a conventional surface.

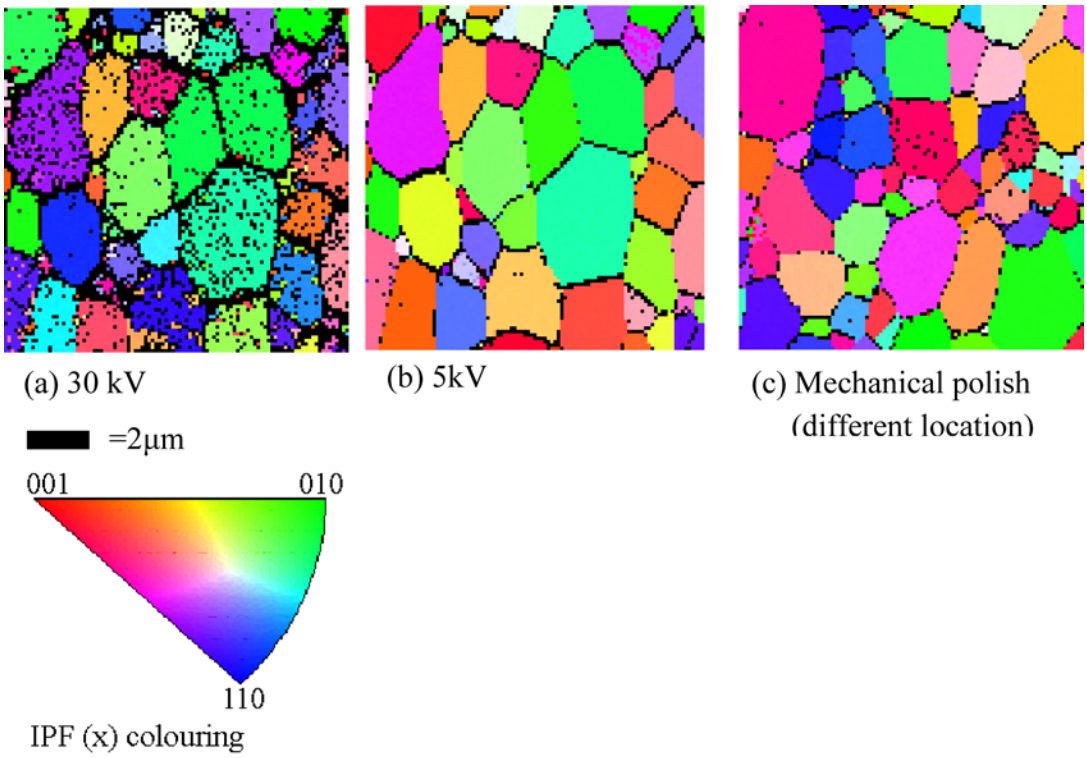

Figure 2-9 Inverse pole figure (x) colour maps of 30 kV, 5 kV milling and mechanical polished surfaces without noise reduction on the STN99 sample. The nonindexed points (black dots) in the 5 kV andmechanical polish map are almost only at grains boundaries. In the 30 kV map there are the nonindexed both at grain boundaries and inside the grains which indicates the FIB damage on the surface.

In 3D-EBSD experiments both indexing accuracy and data acquisition time are important parameters. A good quality working surface can yield a high indexing accuracy and percentage and also can reduce the acquisition time due to the shorter signal integration time of EBSD signal. Using a low voltage FIB milling for serial sectioning can produce excellent surfaces for EBSD measurement however the benefit must be balanced against the extended milling time required compared to using a high kV probe. The high kV FIB milling is to the authors' knowledge always used in 3D-EBSD experiments to reduce data acquisition time and for ease in experimental setup as most FIB's are optimised for working at 30 kV. High milling voltage is applicable for a most metals and material such as YSZ since it yields a high EBSD pattern quality. But for STN, as shown in this work, high kV milling can induce significant damage on the milling surface and yield a poor EBSD signal. Therefore, a long signal integration time is needed to improve pattern quality. For each material the longer milling time must be weighed against the longer pattern acquisition time and the consequent effects this may have, such as sample charging and surface contamination by extended exposure to the electron beam. From the results presented we believe that a combination of rapid coarse milling at 30 kV followed by a light surface polish with a high current low kV FIB beam will provide an optimal solution for many ceramic materials. Work on the combination of low and high kV FIB milling for 3D-EBSD will be reported elsewhere.

2.5 Conclusion

High accelerating voltage FIB milling (30 kV) can induce a significant reduction of the EBSD pattern quality in STN samples, but less effect is seen on the pattern quality of similarly prepared (coated) YSZ. Reducing the milling current can improve the pattern quality. As the backscatter coefficient of YSZ and STN are almost identical and the experimental conditions were identical for both materials it is concluded that the relative reduction of STN pattern quality is caused by FIB damage. By reducing the current from 5000 pA to 100 pA the band contrast and band slope of STN samples is approximately linearly increased as a function of FIB probe current by about 20% and 9-18% respectively. On STN94, coating can help to improve the pattern quality and on STN99, 5kV polishing can lead to a 100% improvement of the pattern

quality relatively to the 30 kV FIB milling. Comparing STN94 and STN99, STN94 yields a better pattern quality than STN99 at all FIB currents as well as on the mechanically polished surface. In 3D-EBSD investigations of SOCs, which have STN and YSZ as major material components, milling in combination with low kV-polishing may be a good alternative to optimise the acquisition time and data quality.

Chapter 3. Ion beam polishing for three dimensional electron backscattered diffraction

3.1 Introduction

Three dimensional electron backscattered diffraction by FIB serial sectioning enables the determination of true crystallographic orientation of grain morphology and grain boundary information in. The technique has been used for 3D material analysis in recrystallisation (Gholinia *et al*., 2010), grain boundary characterisation (Bastos *et al*., 2008,Dillon & Rohrer., 2009,Khorashadizadeh *et al*., 2011), texture analysis (Jin *et al*., 2005,Konrad *et al*., 2006,Petrov *et al*., 2007,Zaafarani *et al*., 2006), grain growth (Liu *et al*., 2008), and deformation (Lin *et al*., 2010). Even though the FIB is a powerful tool integrated in modern electron microscopes it is well known that FIB milling is inherently destructive to specimen surfaces, e.g. crystal structure damage and amorphisation of the milled surface (Pelaz *et al*., 2004,Rubanov & Munroe., 2005). The poor EBSD signal can yield a longer data acquisition time from signal averaging and/or a poor 3D-EBSD data. From our previous work (Saowadee *et al.* 2012) to study the effect of FIB milling (30kV) on Nb-doped strontium titanate and stabilized zirconia shows that EBSP quality, in terms of band contrast and band slope, is decreased by approximately 60% relative to mechanical polishing on strontium titanate but does not have any significant effect on stabilized zirconia. The damage from FIB milling can be reduced by low kV FIB polishing as it is used in transmission electron microscopy sample preparation (Michael & Giannuzzi., 2007,Michael & Kotula., 2008). Our work (Saowadee *et al.* 2012) also shows that on Nb-doped strontium titanate 5kV polishing can lead to a 100% improvement of band contrast and band slope and approximately 20% improvement of indexing percentage relative to 30 kV FIB milling. In this work the low kV FIB polishing was included in the normal 3D-EBSD process to improve data quality and is described below. La and Nb-doped strontium titanate was used in this study as it is known to suffer from Ga^+ ion beam damage and reduced EBSD pattern quality (Saowadee *et al.* 2012).

3.2 Experiment

3.2.1 Focused ion beam polishing for 3D-EBSD

Normally, 3D-EBSD data collection by FIB serial sectioning comprises of two main processes, FIB milling and EBSD data collection as illustrated in Figure 3-1(a). The sample is first moved to the FIB milling position and a designated area is milled to create a flat and smooth surface for EBSD data collection. The sample is then moved to the EBSD position to collect an EBSD map on the milling surface. Figure 3-1(b) shows a diagram of 3D-EBSD with low kV FIB polishing. The polishing process is performed at the milling position after the milling process is finished. The ion beam is switched to a low kV probe for polishing which for the present instrument involves a FIB gun shutdown between voltage changes[1]. The selected milling shape for the low kV polishing is a line scan as polishing should be restricted to the near surface and 2D scanning will increase the polishing time due to scanning of redundant areas. We observe large random beam shift (in the order of 1-2 μm) when switching to the low kV probe in our instrument. Thus a focused low kV polishing line often will not impinge on the EBSD mapping surface for each slice. Furthermore, as present 3D-EBSD systems are not designed to incorporate polishing there is no software capacity for additional drift correction. Therefore in our method, the low kV probe is defocused to broaden the beam to ensure that the polishing beam will impinge on the working surface. Figure 3-2 (a) shows a defocused line scan to the left of the alignment fiducial mark. Figure 3-2 (b) shows a working area after performing 3D-EBSD with FIB polishing and the resulting of FIB polishing.

[1] We have not observed adverse effects of repeated gun shut downs and voltage change on gallium source lifetime.

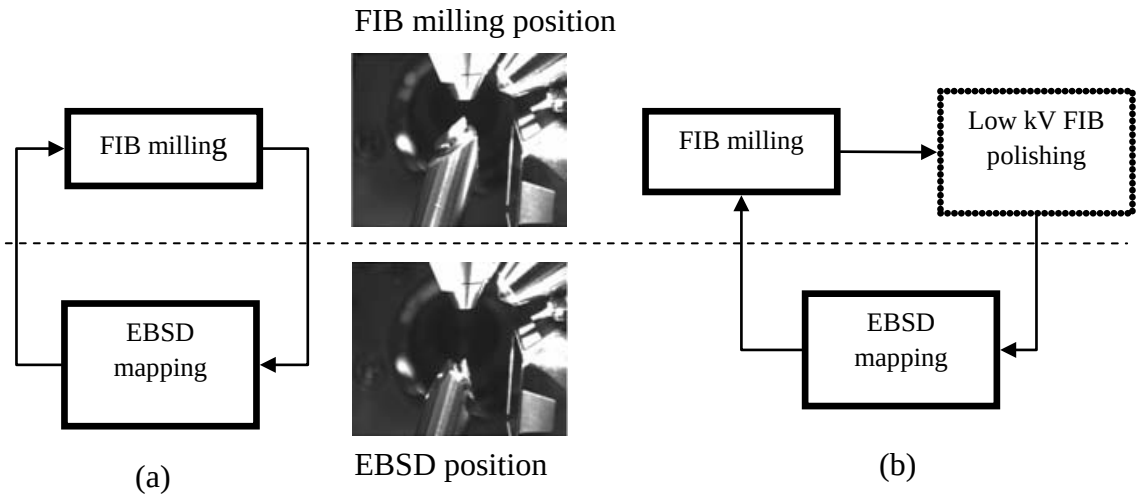

Figure 3-1 (a) Normal 3D-EBSD process by FIB serial sectioning. (b) 3D-EBSD by FIB serial sectioning with low kV FIB polishing. The processes above the dashed line are performed in the FIB milling position and the processes below the dashed line preformed in the EBSD data collection position.

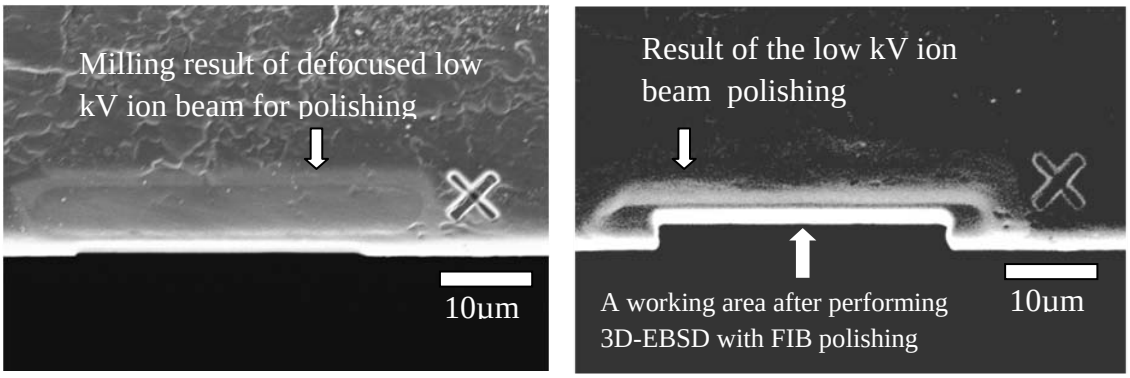

Figure3-2 a) FIB image of the milling result of a 40 μm long low kV FIB polishing line. b) FIB image of a working area after performing3D-EBSD with FIB polishing and the result of FIB polishing.

3.2.2 Sample preparation and method

$Sr_{0.96}La_{0.02}Ti_{0.9}Nb_{0.1}O_3$ (STLN) was used in this study. The STLN was synthesised into bulk pellets by isostatic pressing and was sintered at 1450°C in 9%H_2/Ar. For a detailed sample preparation see (Saowadee *et al.* 2012).

FIB-SEM and EBSD for this work was performed on a Zeiss CrossBeam 1540XB™ (Oberkochen Germany) equipped with an Oxford Instruments Nordlys S™ EBSD detector (Hobro Denmark). Oxford Instruments' software HKL Fast Acquisition 1.3 and Channel 5 were used for data collection and analysis. A FIB 30kV 2 nA probe was used for milling material and a 5kV 2.5nA probe was used for polishing. EBSD mapping was performed with a SEM voltage of 20 kV using the 60 µm aperture and high current mode that yields the electron beam current of approximately 7.17 nA. EBSD camera was set to the same parameters as used in (Saowadee *et al.* 2012). To compare the effect of signal averaging and FIB polishing on EBSP quality improvement four EBSD maps of 12.6x12.6 µm with step size 0.075 µm were performed on the same FIB milling surface with different signal averaging and polishing conditions. The first map was collected with EBSP frame average 1 where the second map was collected with frame average 2. Subsequently the surface was polished with the 5 kV probe. The third map and the fourth map were collected on the polished surface with frame average of 1 and 2 respectively. Two 3D-EBSD data sets of volume 12.6x12.6x3.0 µm were collected with EBSD step size 0.075µm and slice thickness 0.1 µm. The first data set was collected by normal 3D-EBSD process with frame average 1 and the second data set was collected by 3D-EBSD with FIB polishing and frame average 2. The polishing time for each slice was 1 minute.

3.3 Results and discussion

Table 3-1 shows indexing rate, average band contrast and average band slope of the four EBSD maps and the two 3D-EBSD maps. Increasing the number of averaged frames from 1 to 2 increases indexing rate by 23% and improves average band contrast and band slope approximately 8% and 14%, respectively. Whereas 1 minute of low kV FIB polishing can increase the indexing rate approximately 41% and improves the average band contrast and band

slope by approximately 42% and 48%, respectively. Frame average 2 on the polished surface improves indexing rate 8% band contrast 8% and band sloe 12%. Inverse pole figure (x-axis) plots of the four EBSD maps are shown in Figure 3-3. As indicated by white circles in Figure 3-3 (a) and (c), some small grains in the unpolished map are missing but can be observed in the polished map. In Figure 3-3(c) zero solutions (black dots) are significantly more prevalent in the upper area of the map compared to the lower area; note that the ion beam mills from the bottom of the image. This indicates that polishing performance decreases as the beam mills further down the working surface. Thus the heterogeneous polishing may be caused by a more broadened ion beam at areas far from milling edge. This possibly be solve by increase the polishing time. 3D-EBSD maps of the STLN sample with and without FIB polishing are shown in figure 3-4(a) and (b) respectively. The acquisition time per slice of the polishing data set is approximately 30 minutes: FIB milling time 6 minutes, FIB polishing time 1 minute and EBSD mapping time 23 minutes (frame averaging 2). For the additional polishing step the acquisition time increases modestly by 3.3% compared to the significant improvement of the indexing rate and pattern quality.

Table 3-1 Indexing rate, average band contrast and average band slope of the three EBSD maps and two 3D-EBSD maps.

Acquisition conditions	**Indexing rate**	**Mapping time /slice (m:s)**	**Band contrast (0-255)**	**Band slope (0-255)**
Unpolished , frame average 1	56.6%	11:29	98.3	127.0
Unpolished, frame average 2	69.8%	22:57	106.5	145.3
Polished, frame average 1	80.2%	11:29	139.2	188.4
Polished, frame average 2	87.5%	22:57	151.1	210.7
3D-EBSD, frame average 1	56.7%	11:29	105.0	128.7
3D-EBSD with FIB polishing, frame average 2	86.2%	22:57	148.7	198.1

During 3D-EBSD we observed that the polishing beam removes relatively more material where the ion beam first meets the sample yielding a curved edge. The depth of the curved edge was observed to increase from the first slice to the last slice. The curved edge depth at the last slice is approximately 5 µm. In this experiment EBSD data was acquired at a safe distance, i.e. approximately 10 µm from the edge. However we performed an additional EBSD map on the curved surface of the last slice and found that the mapping quality at the curved edge is better than the flat part of the polished surface as illustrated in Figure 3-5 (a). This means the polishing performance might be improved by creating a third new sample position particularly for polishing. This would be achieved by slightly increasing the sample tilt angle, thus the defocused ion beam impinges on the sample surface at a small angle as illustrated in Figure 3-5 (b). By this method the damaged or amorphous layer can be removed quicker than milling with a parallel beam. Further experiments are required to identify the optimum tilt angle. If the beam is exposed to the surface for too long or the beam angle is too large this may cause future damage on the surface. In this manner it is expected that the curved edge problem may be reduced and polishing times could be significantly reduced.

Another potential method to improve the polishing performance would be to use the focused polishing beam parallel to the sample surface. However this method requires precise position realignment (i.e. drift correction) after switching the FIB gun to low kV. For our instrument, the focused ion beam diameter of a high current probe can be in the order of a micron. If the position realignment error is less than a half micron, low kV focused ion beam polishing using a line scan of a high current beam should be achievable. Apart from the curve edge no further artefacts such as curtaining, were observed on the surface caused whilst using high current low kV FIB polishing.

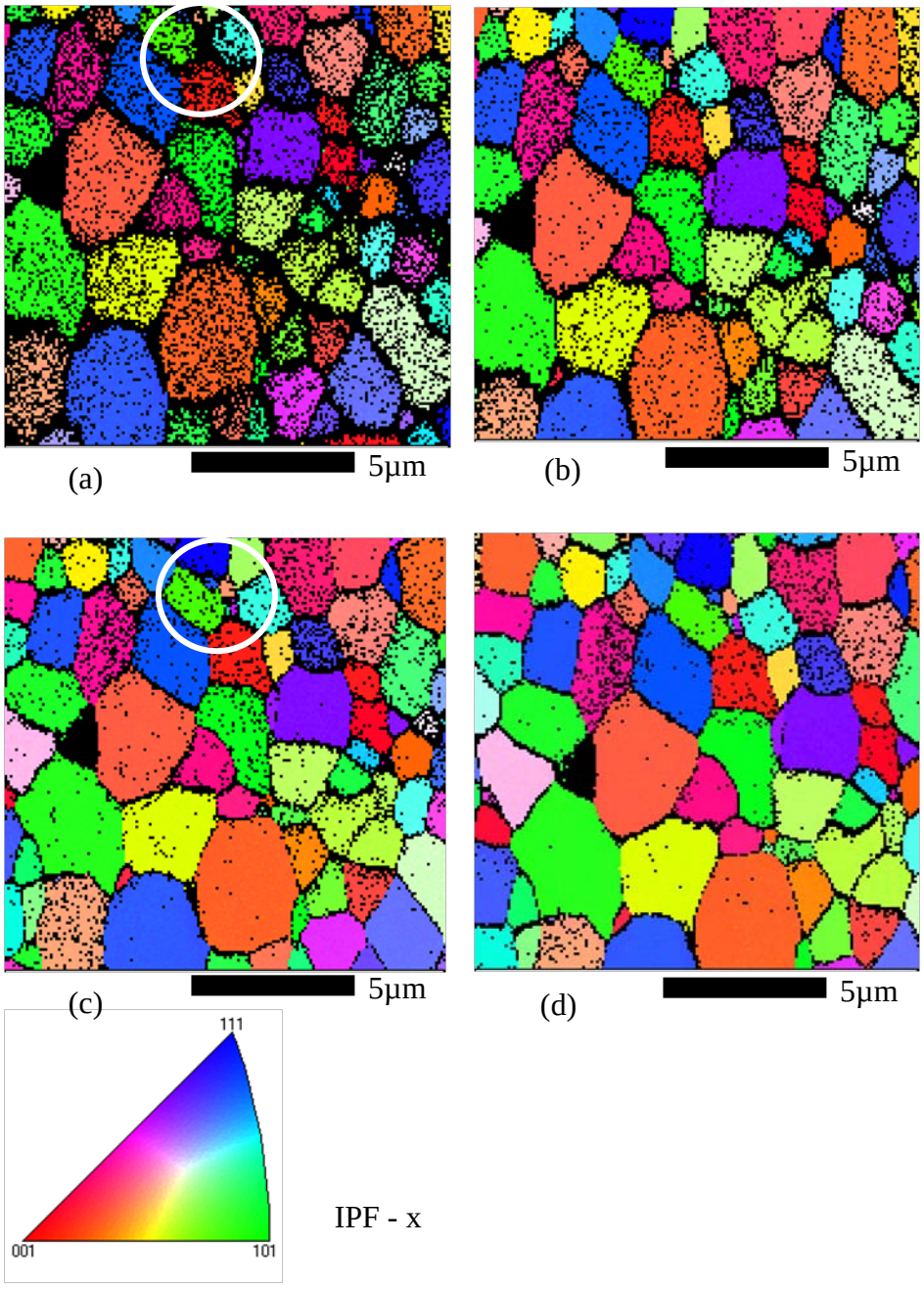

Figure 3-3 Inverse pole figure (x-axis) plot of unprocessed 2D EBSD maps (a) on 30 kV milling surface frame average 1 (b) on 30 kV milling surface frame average 2 (c) 5kV polishing surface frame average 1.

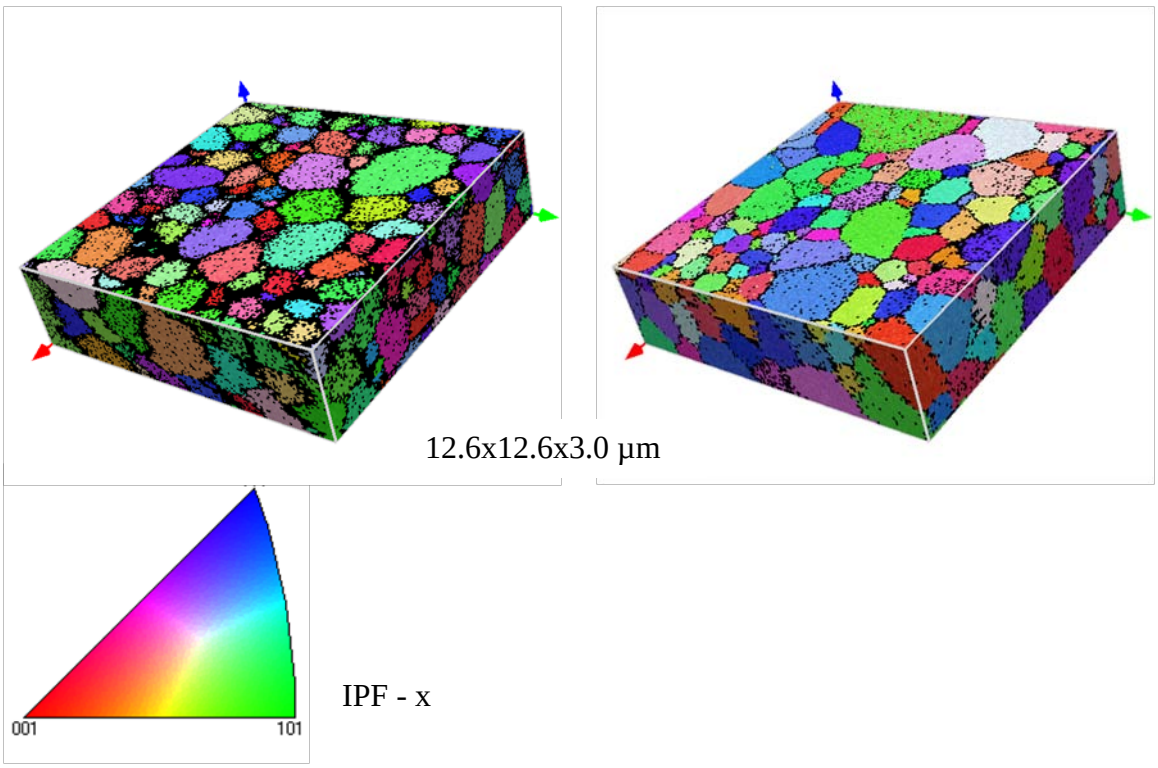

Figure 3-4 Inverse pole figure (x-axis) plot with zero solution in black of 3D-EBSD of STLN (a) by normal 3D-EBSD routine with 30 kV FIB milling and frame average 1(b) by 3D-EBSD with 5kV FIB polishing and frame average 2.

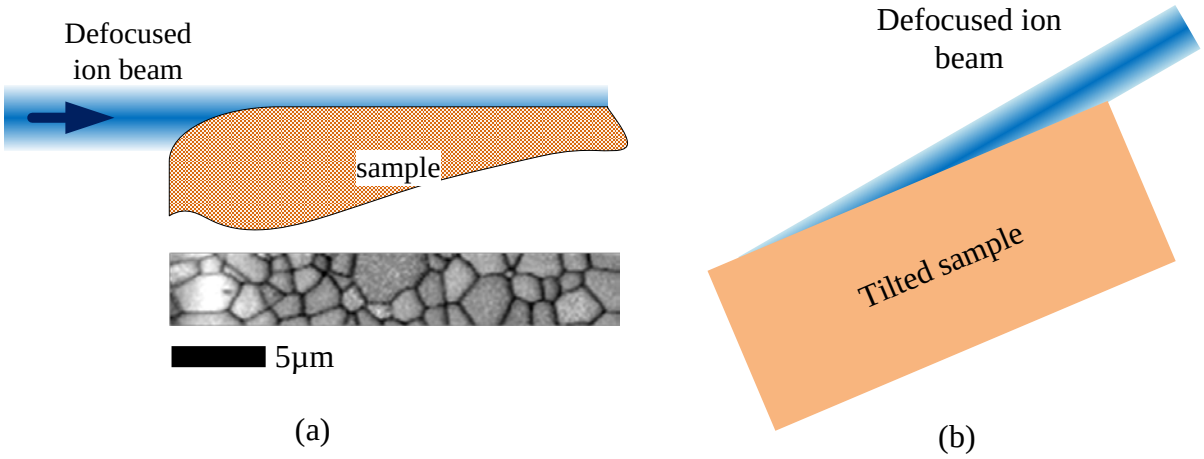

Figure 3-5 a) The additional band contrast plot of the curved edge shows a better polishing quality at the curved edge resulting from FIB polishing. b) Suggested special position for polishing in which a defocused ion beam impinges on the sample surface at a small angle.

3.4 Conclusion

Automatic low kV FIB polishing is successfully applied for 3D-EBSD of La and Nb doped strontium titanate. The selected milling shape for the low kV polishing is a line scan as polishing should be restricted to the near surface and 2D scanning will increase the polishing time due to scanning of redundant areas. The low kV beam is defocused to ensure that the polishing beam is always incontact with the working surface. The polishing time per slice used in this study (1 minute) yields a modest total acquisition time increase of 3.3% relative to normal 3D-EBSD data acquisition. Furthermore, polishing leads to a significant improvement of the index rate and pattern quality. Lastly, two methods to further improve the FIB polishing are proposed.

Chapter 4. 2D and 3D EBSD data Collection and primary investigation of strontium titanate

4.1 Introduction

La and Nb doped strontium titanate (STLN) with different La content were chosen for this study. The STLNs were observed conductivity change with the La content. 2D-EBSD was used to investigate microstructure statistic of the STLNs since 3D-EBSD is used for study in more detail in specific volume. The 3D-EBSD data in this collection were used in grain boundary relative energy and pressure calculation in Chapter 5.

4.2 Data collection

4.2.1 Materials

Four sample of STLN with different La content $Sr_{0.99-x}La_xTi_{0.9}Nb_{0.1}O_3$ (x = 0.000, 0.005, 0.01 and 0.02) were investigated in this work. For convenient the four samples are denoted by STLN1 STLN2 STLN3 and STLN4 for La = 0.000, 0.005, 0.01 and 0.02 respectively. The STLNs were synthesised into bulk pellets by isostatic pressing and was sintered at 1450°C in 9%H2/Ar. The samples were preparation for EBSD data collection as described in Chapter 2.

4.2.2 Data collection

FIB-SEM and EBSD for this work was performed on a Zeiss CrossBeam 1540XB™ (Oberkochen Germany) equipped with an Oxford Instruments Nordlys S™ EBSD detector (Hobro Denmark). Procedure for data collection is described as the following.

1) Pre-investigation of grain size

Each STLN sample was explored grain size using backscattered electron (BSE) image to design the area of data collection. BSE images of the four samples are shown in Figure 4-1 to 4-4. In BSE image of STLN4 (Figure 4-4) grains cannot be observed because electron backscattered signal from the sample is quite poor. Grain sizes observed in STLN1-3 are very heterogeneous. Some giant grains of diameter in the order of 100 μm are found in STLN1 and STLN2. An abnormal porous area is found in STLN3 (see Figure 4-3). Grains in the porous area are very fine compare to the normal area in the sample and the porous area is surrounding by big grains. Designation of collecting area size is difficult because of the heterogeneous of the grain size. Thus the size of collecting area was estimated from the grain size at the location to be collect data. To investigate STLN4 grain size FIB polishing is needed.

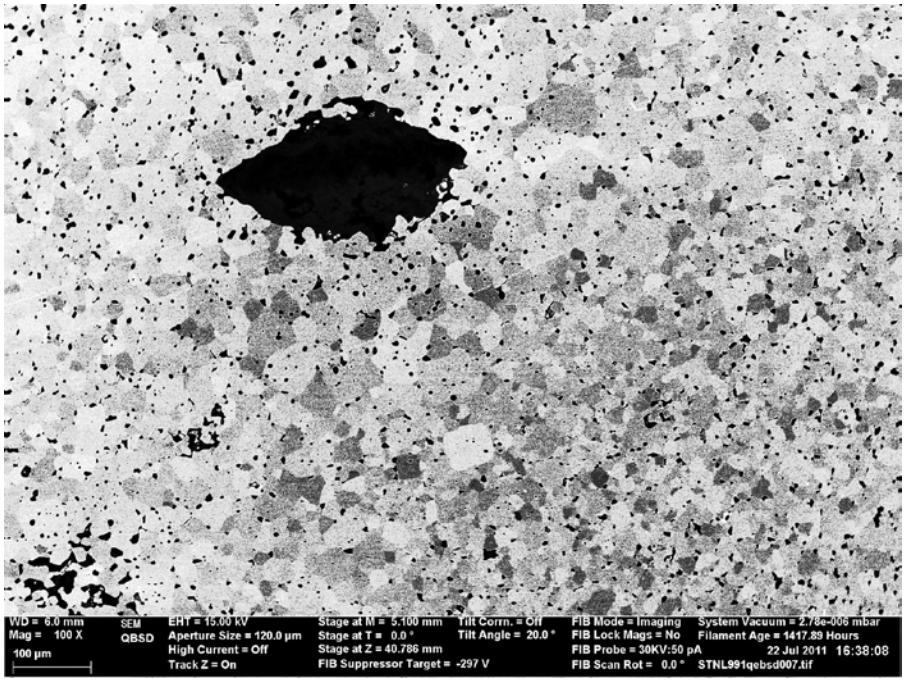

Figure 4-1 BSE image of STLN1.

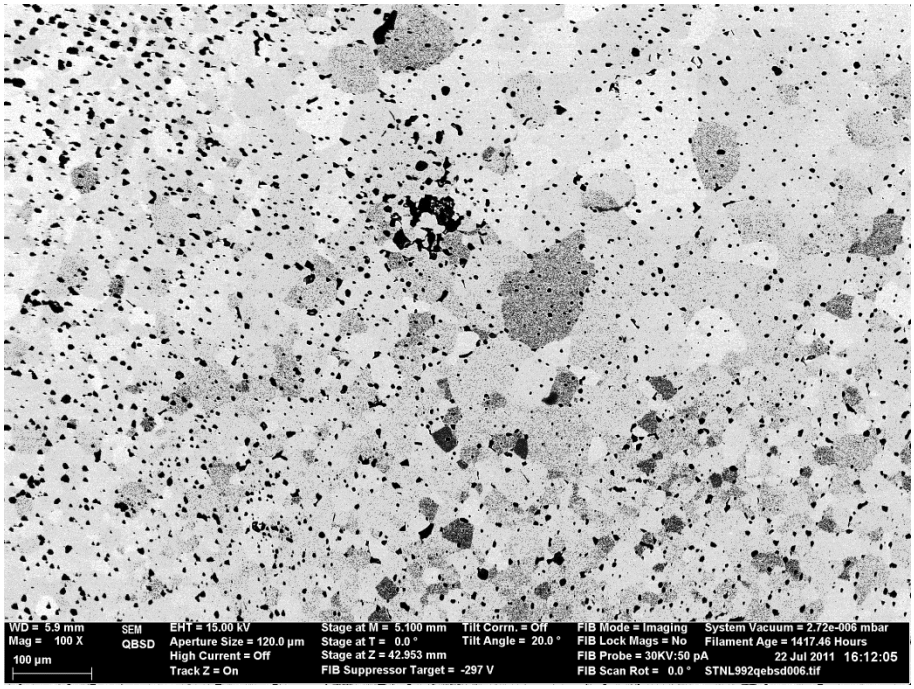

Figure 4-2 BSE image of STLN2.

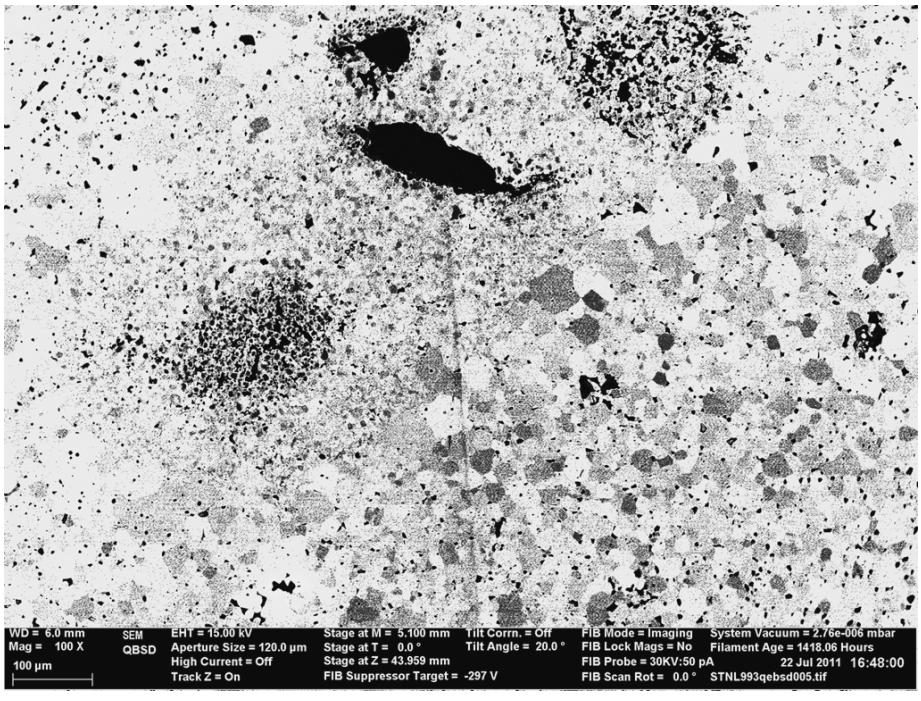

Figure 4-3 BSE image of STLN3.

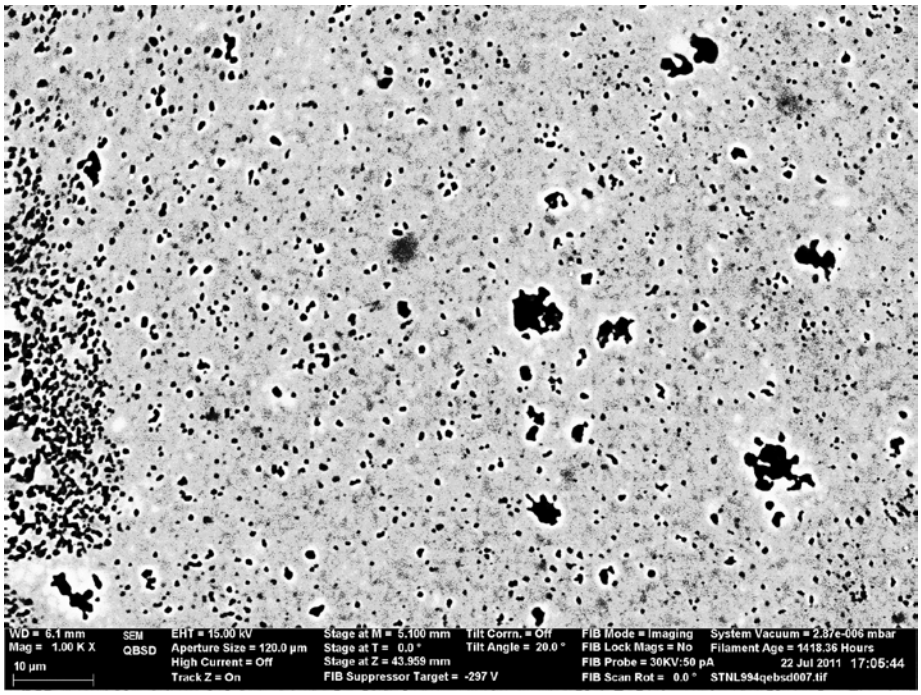

Figure 4-4 BSE image of STLN4.

2) 2D-EBSD data collection

The largeness of sample grain size and the limitation of acquisition volume of FIB 3D-EBSD make the 3D-EBSD cannot provide enough number of complete grains to analyse statistical grain characteristic. Each STLN sample was polished using the 5 kV ion beam. Polishing area of each sample is approximately 350x350 μm on the top surface of the sample. In the polishing, sample tilt angle was 5 degree greater the angle which its top surface parallel to the FIB. Ion beam was defocus as described in chapter 3 but milling pattern is change from milling line to milling box of width 350 and height 30 μm in order to polish the large area. Mapping area of STLN1 and STLN2 is 300x300 μm with step size 1 μm. Mapping area of STLN3 is 300x250 μm with step size 0.5 μm. A quick EBSD map on STLN4 after polishing shows its grain size is very heterogonous as in the others. STLN4 grain diameter is approximately in the range of a fraction of micron to 10 μm. The mapping area of STLN4 is selected to be 30x30 um with step size of 0.05 μm. EBSD maps of the four STLNs were collected using Flamingo version

1.3 (Oxford instrument, London UK) at SEM 15 kV, signal binning 4x4, integration time 12.4 ms and signal averaging 2.

3) 3-D-EBSD data collection

- Collection of STLN1 and STLN2

Since the grain size of STLN1 and STLN2 are very large the author designed to collect the larger volume by targets the volume at 100x100x50 μm. To achieve the data collection of such large volume with reasonable time FIB 20nA 30kV was utilised according to the result of FIB damage investigation in chapter 2. However the FIB 20 nA with a normal beam profile cannot yield a smooth milling surface since condensing a high current beam is difficult. Figure 4-5-(a) bellow shows the cross section beam profile of the FIB 20nA by spot milling for 10 seconds at the bottom and it milling result on the top. While the inner high intensity beam removes material from the milling surface the outer low intensity beam below destroy the surface. To make the FIB 20 nA available for milling smooth surface the beam profile was realignment by shift the high intensity part to the bottom of the beam as shown in Figure 4-5(b) bellow. Thus there is no low intensity beam below the high intensity beam to destroy the milling surface. Compare to the FIB 2 nA that normally used in 3D-EBSD data collection to mill a slice of area 100x100 μm slice thickness 0.75 μm on STLN sample, the FIB 20nA needs approximately 1.33 hours while the FIB 2nA needs approximately 4 hours. The FIB 20nA with the new beam profile was used to collect 3D EBSD data of STLN1. However after finish data collection of STLN1 it found that the new beam profile made damage on the FIB device thus the new beam profile was cancelled. FIB 2 nA was used in data collection of STLN2. Other acquisition parameters of STLN1 and STLN2 are listed in table 4-1.

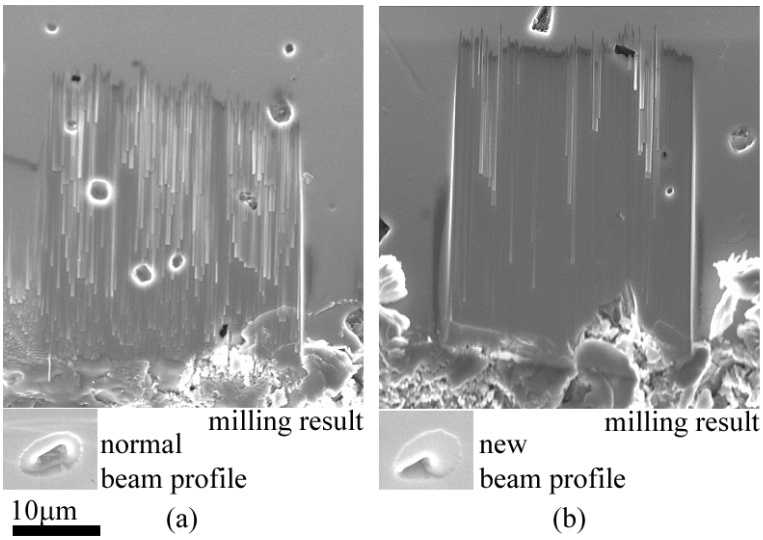

Figure 4-5 (a) below is normal cross section beam profile of the FIB 20 nA by spot milling for 10 seconds and its milling result on the top. (b) A new cross section beam profile of the FIB 20 nA with the high intensity beam at the bottom and its milling result.

- Collection data of STLN3 and STLN4

FIB 2nA 30kV was used in data acquisition of STLN3. Target data volume is 50x50x15 μm. FIB polishing described in Chapter 3 was implemented to collect EBSD data of STLN4 since EBSD from 30kV FIB milling of the sample is very poor. Target data volume is 15x15x5 μm. Data acquisition parameters are list in table 4-1.

Table 4-1 3D-EBSD acquisition parameters of STLNs

Sample	SEM kV	Frame averaging	Binning	Gain Amplification	EBSD step size	Slice thickness
STLN1	15kV	2	4x4	Low	0.75μm	0.75μm
STLN2	15kV	2	4x4	Low	0.50μm	0.50μm
STLN3	15kV	2	4x4	Low	0.40μm	0.40μm
STLN4	15kV	2	4x4	Low	0.075μm	0.10μm

4.3 Data analysis

4.3.1 Two dimensional EBSD analysis

2D EBSD analysis of grain size and grain boundary was performed by using program Tango of Channel 5 software suit (Oxford Instruments, London UK). Texture analysis was analysed in the Salsa of the channel 5 software.

4.3.2 3D-EBSD data reconstruction and primary analysis

3D-EBSD data of STLNs were reconstructed using the HKL 3D-viewer program (Oxford Instruments, London UK) using threshold misorientation angle 3° and minimum grain size 27 voxels. Grain volumes, grain diameters, grain boundary area per volume and grain roughness of the four data sets were measure using the HKL 3D-viewer program.

4.4 Results and discussion

4.4.1 Two dimensional EBSD analysis

2D-EBSD map of STLN1-4 are shown in Figure 4-6 to 4-9 respectively. Number of grains (edge touch excluded) in the maps are 520, 426, 982 and 696 respectively. Grain size, grain boundary and texture analysis of the 2D-EBSD map were presented next to the four maps.

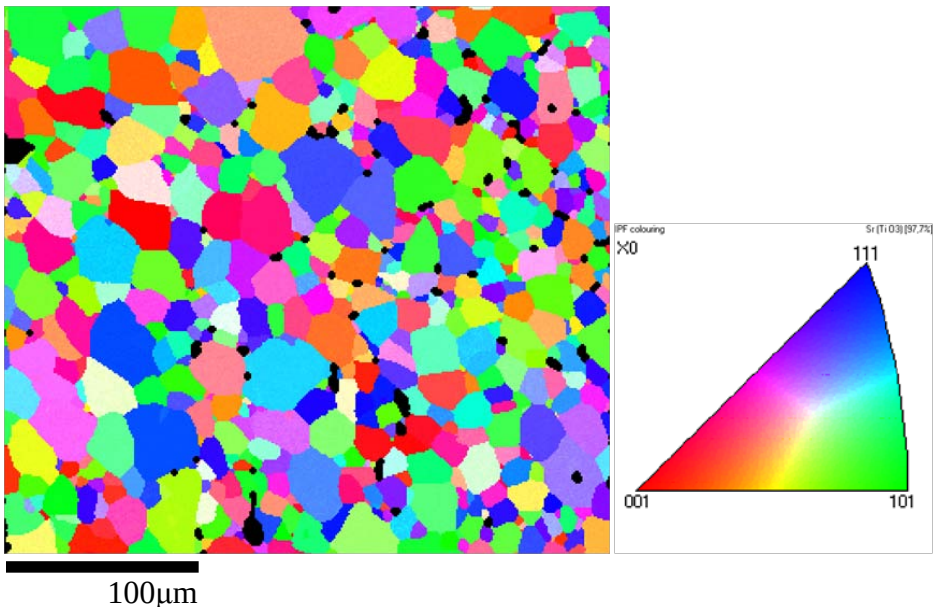

Figure 4-6 Inverse pole figure (x-axis) mapping of STLN1.

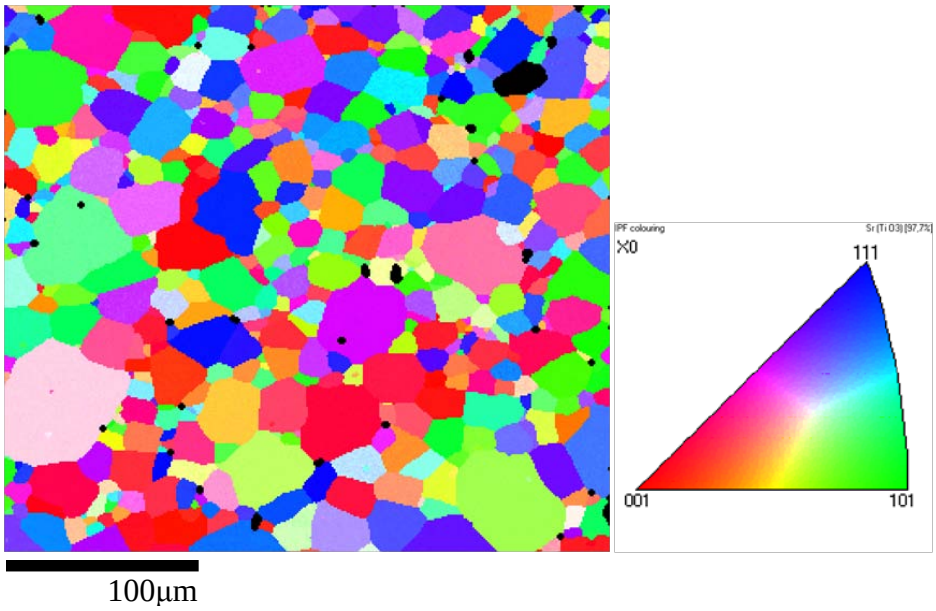

Figure 4-7 Inverse pole figure (x-axis) mapping of STLN2.

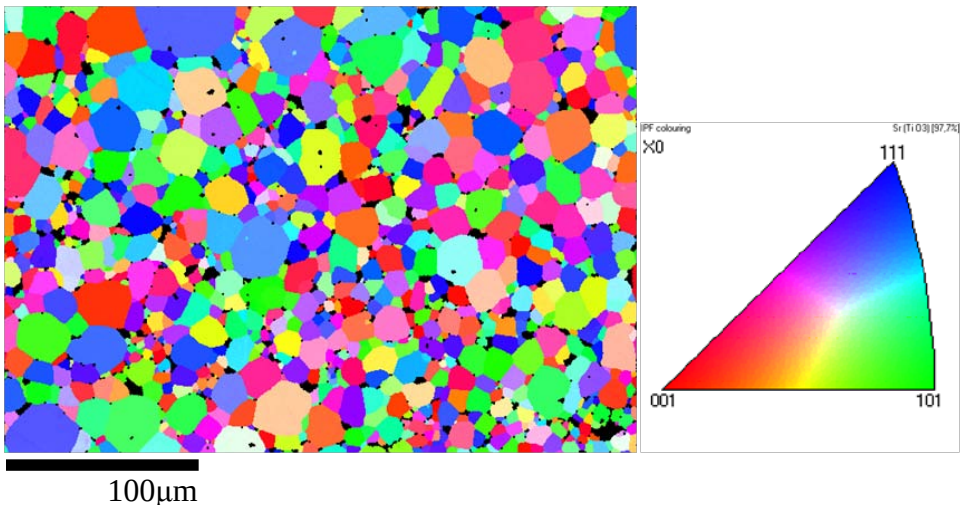

Figure 4-8 Inverse pole figure (x-axis) mapping of STLN3.

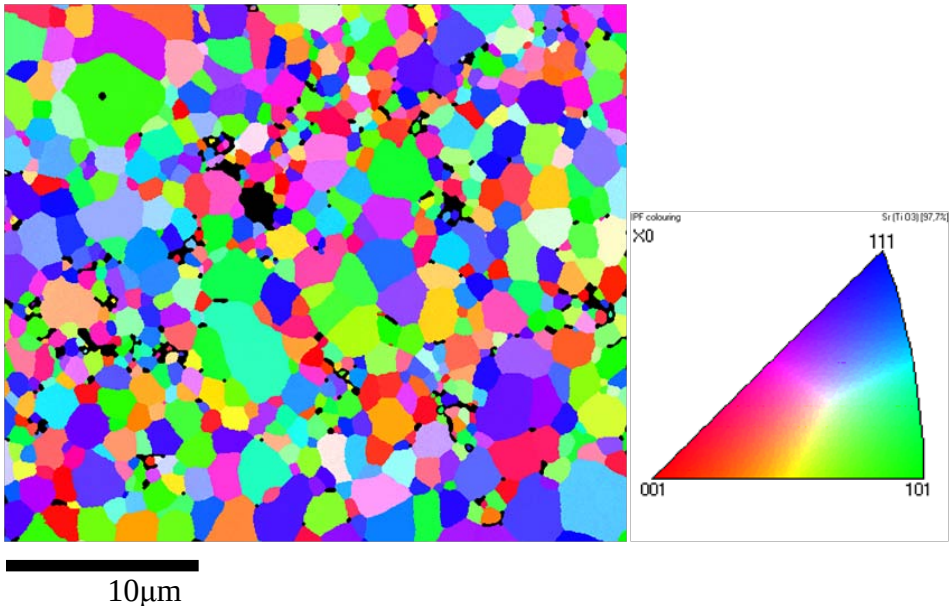

Figure 4-9 Inverse pole figure (x-axis) mapping of STLN4.

1) Grain size

Average grain diameter of STLN1-4 measured form the 2D-EBSD maps are plotted in Figure 4-10. Trend of average grain diameters is decrease as Nb% increase. However grain size of STLN1 and STLN2 are nearly equal. In STLN2 (La = 0.005) it is possible that there is sufficient A site for the La in the strontium titanate lattice. Thus the grain growth of STLN1 and STLN2 can be quite similar. In STLN3 and STLN4 the doped lanthanum is increase and exceed lanthanum can slow down grain growth in STLN3 and STLN4 by segregation at grain boundary. Grain size standard deviation of each sample is approximately 65% of its average grain diameter. The standard deviation is quite high since abnormal grain growth is often happen in strontium titanate. Figure 3-11 shows grain perimeter per area of the STLNs. Trend of the graph is similar to the trend of conductivity.

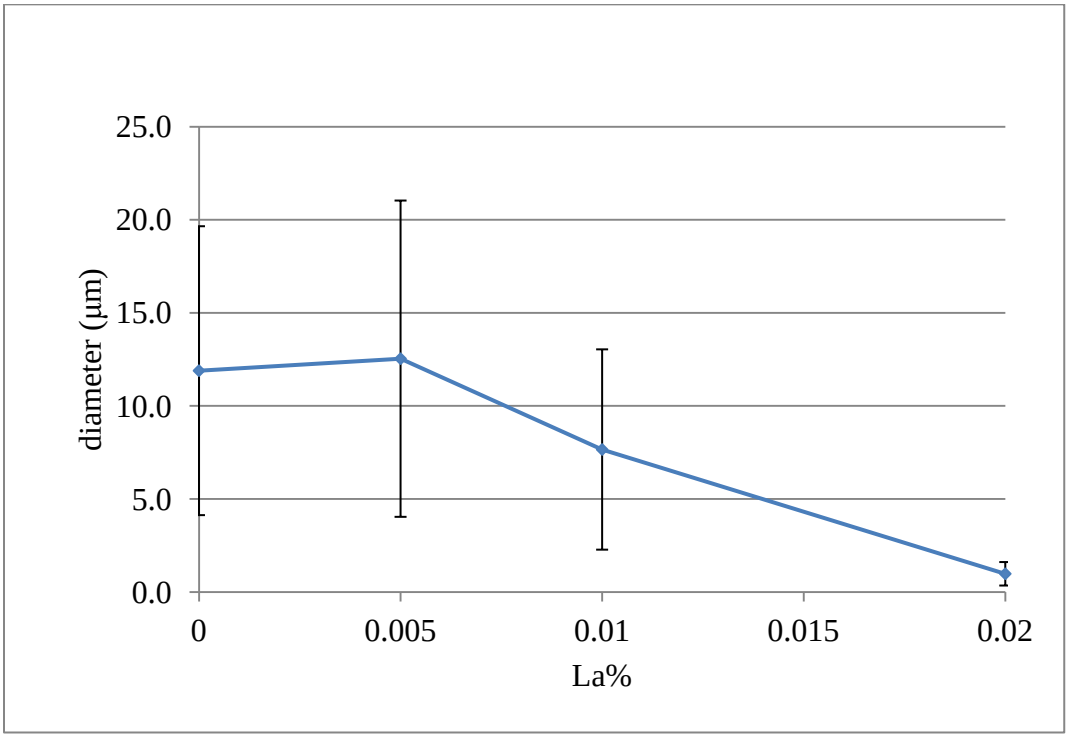

Figure 5-10 average grain diameters of STLN1-4 (La = 0.0, 0.005, 0.01 and 0.02 respectively)

2) Grain perimeter per unit area

Figure 4-11 shows a plot of perimeter per unit area and conductivity of the STLN samples. Conductivities of the STLN1-4 at room temperature are 290, 320, 830 and 1100 s/cm respectively (private communication, Agersted K.). The plot shows that trend of the conductivity graph agrees to trend of the perimeter per unit area except at the point La content = 0.02.

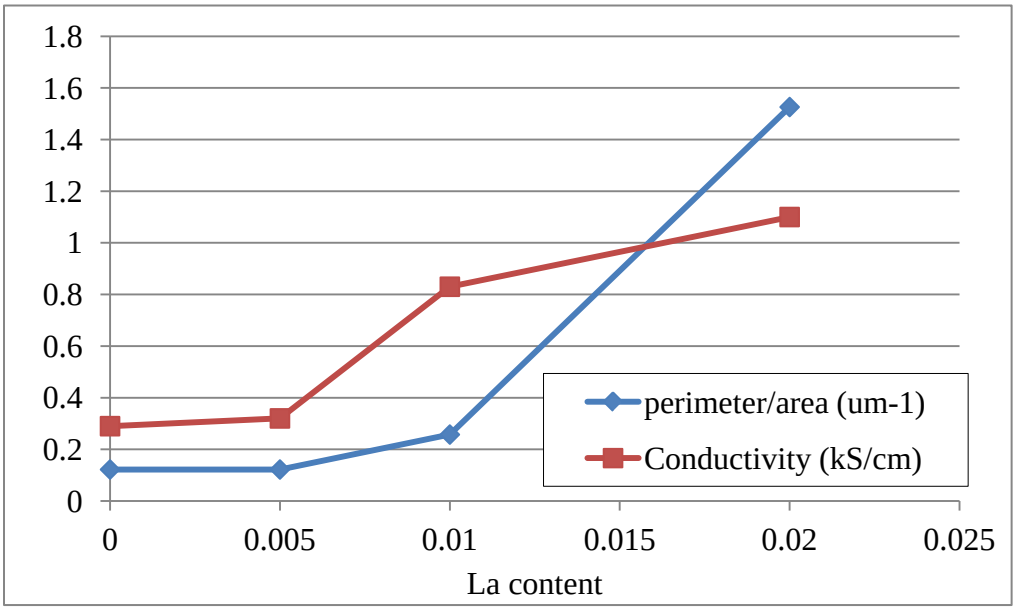

Figure 4-11 grain perimeter per unit area of STLN1-4 (La = 0.0, 0.005, 0.01 and 0.02 respectively)

3) Grains boundaries

Figure 4-12 shows percentage of Σ3 and Σ5 grain boundary of STLN1-4 and low angle boundary in Figure 4-13. There is no significant difference in the percentage of special grain boundaries in the four STLNs. Figure 3-14 shows percentage of low angle grain boundary (15°) in the STLN samples and there is no significant different found. Trend of the low angle grain boundary percentage similar to the trend of grain size i.e. decrease as Nb% increase. Figure 3-15 shows misorientation distribution of the STLNs. It shows that the distributions of all the STLNs are random.

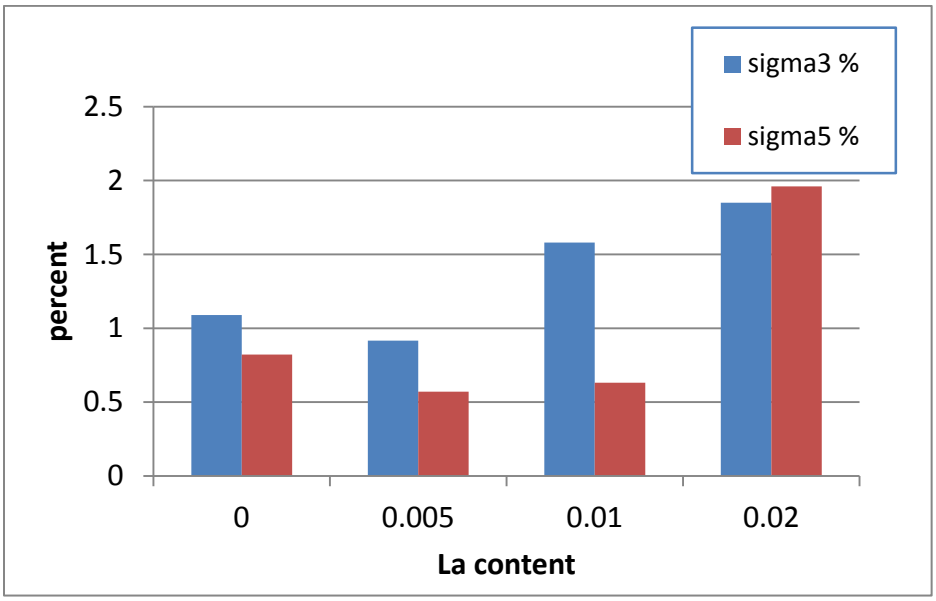

Figure 4-12 percentage of Σ3 and Σ5 grain boundary of STLN1-4 (La = 0.0, 0.005, 0.01 and 0.02 respectively).

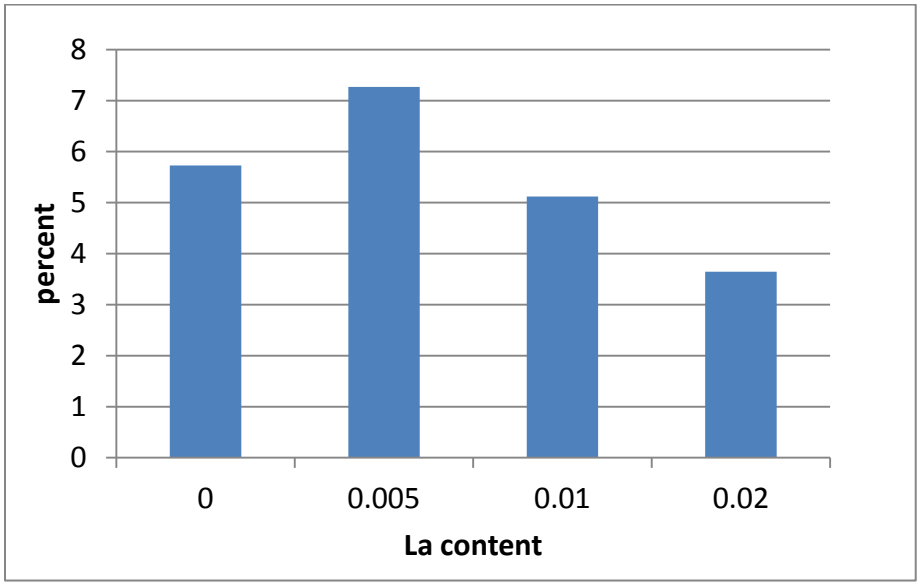

Figure 5-13 Pecentage of low angle grain boundary (3-15°) of STLN1-4 (La = 0.0, 0.005, 0.01 and 0.02 respectively).

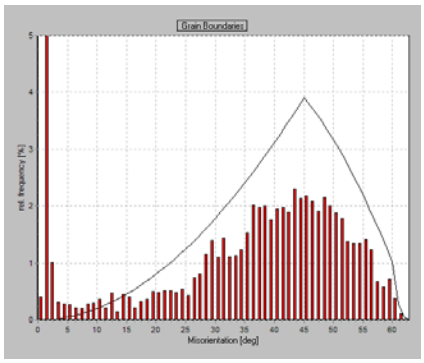

STLN1

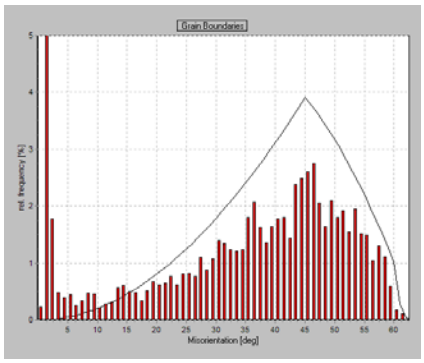

STLN2

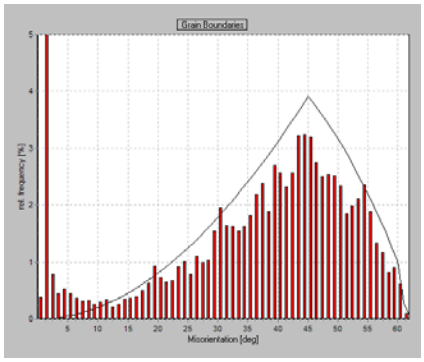

STLN3

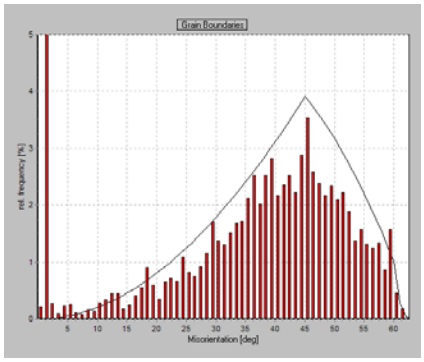

STLN4

Figure 5-14 Misorientation distribution of STLN1-4 (La = 0.0, 0.005, 0.01 and 0.02 respectively).

4) Texture

Pole figure contour plots of direction {100} {110} and {111} of STLN1-4 are shown in Figure 4-15. The pole figure plot of each STLN shows random texture as expectation since the STLN samples were prepared by powder processing.

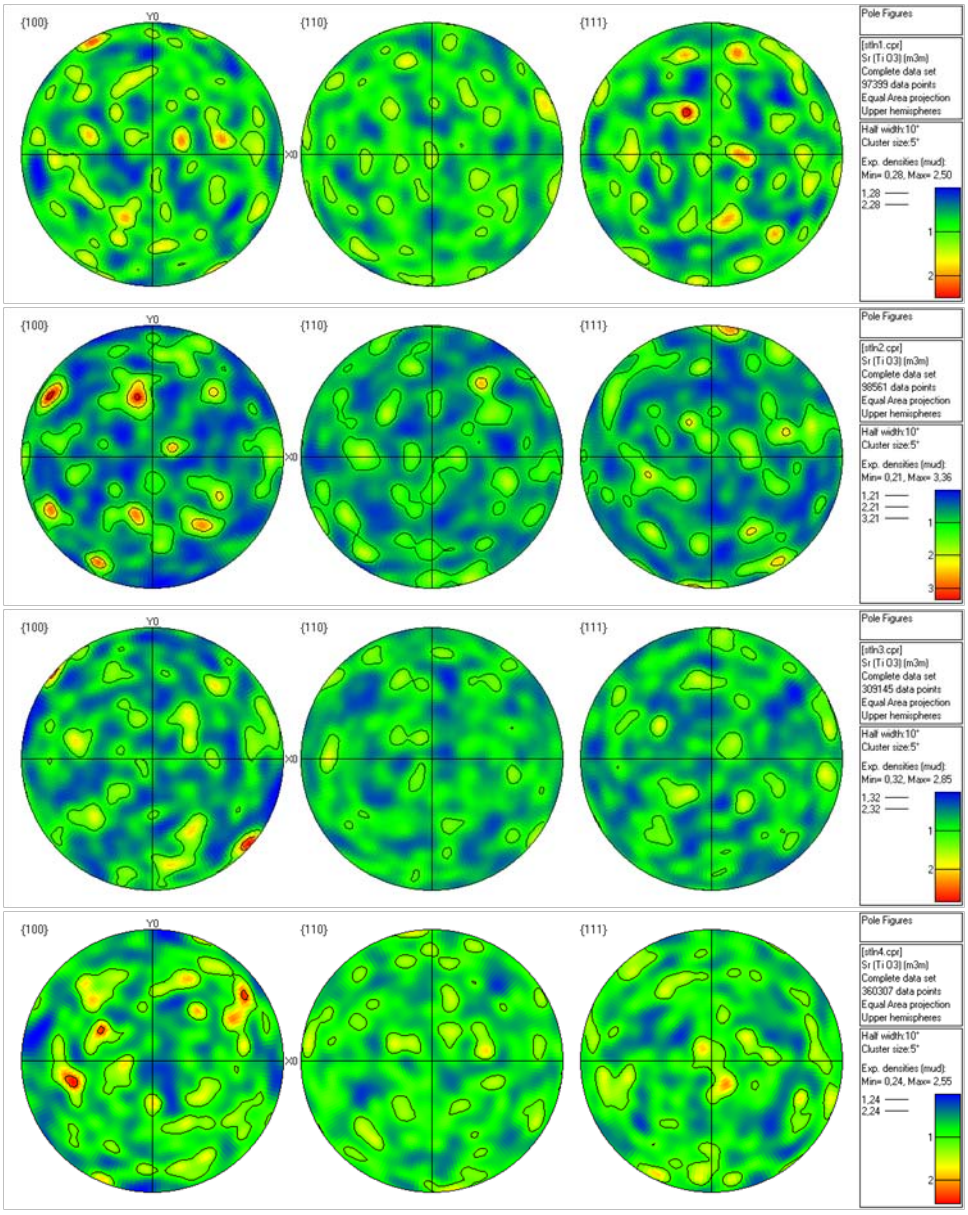

Figure 4-15 pole figure contour plots direction {100} {110} and {111} of STLN1-4.

4.4.2 Three dimensional EBSD analysis

1) Data reconstruction and noise reduction

Figure 4-16 to4-19 show inverse pole figure colour maps of 3D-EBSD of STLN1-4 respectively. 3D-EBSD of STLN1 and STLN2 were collected in multi-sessions according to the long acquisition time of the huge data volume. The data of STLN1 consists of two sub-data sets while 3D-EBSD of STLN2 in Figure 4-17-(a) consists of five sub-data sets. Two sub-data sets at the middle of STLN2 are poor according to milling position re-alignment error and the FIB damage the working surface. The whole data of STLN2 cannot be used in data analysis thus the largest sub-data set at the bottom of the data set was cropped for data analysis (see figure 4-12 (b)). 3D-EBSD data volume number of grains and number of complete grain in each data set are listed in Table 4-2. Data collection cannot reach the target volume mainly due to the position re-alignment error and the acquisition process stopped. In STLN1 and STLN2 curtaining pattern appears on the working area deeper than approximately 60 μm in milling direction. However grain size of STLN1 and STLN2 are very large un-indexing points due to the curtaining can be extrapolated.

Table 4-2 data volume, number of grains and number of complete grain of SLN1-4

samples	volume	grains	complete grains
STLN1	88.5 x 63.0 x 15.75 μm	121	19
STLN2	100.0 x 89.0 x 9.0 μm	50	1
STLN3	40.0 x 38.8 x 10.4 μm	381	105
STLN4	12.2 x 12.2 x 3.3 μm	275	55

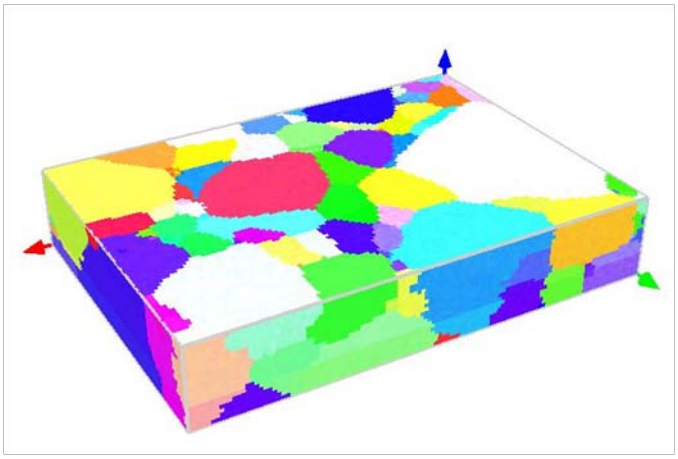

88.5 x 63.0 x 15.75 µm

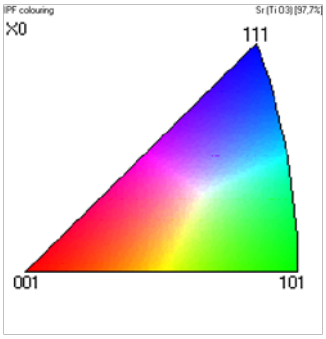

Figure 4-16 Inverse pole figure (x-axis) colour mapping of 3D-EBSD data of STLN1 of volume 88.5 x 63.0 x 15.75µm. Number of grains in the data set is 121 grains with 19 complete grains.

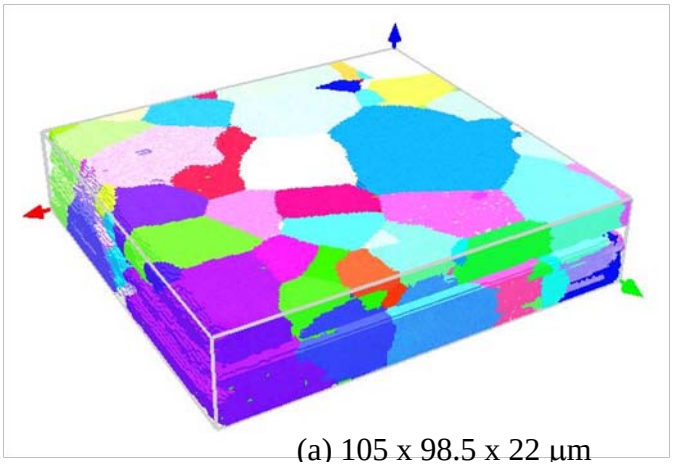

(a) 105 x 98.5 x 22 μm

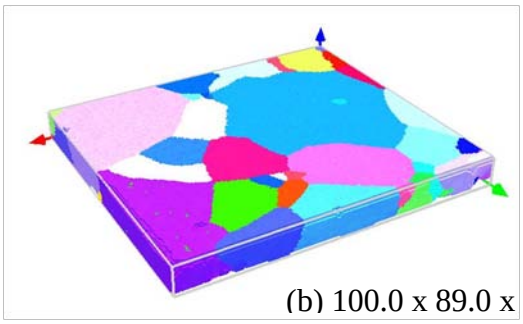

(b) 100.0 x 89.0 x 9.0 μm

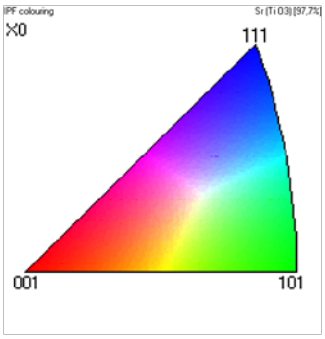

Figure 4-17 Inverse pole figure (x-axis) colour mappings of 3D-EBSD data of STLN2. The large data set (a) of volume 105 x 98.5 x 22 μm has five poor slices at the middle. The small data set (b) of volume 100.0 x 89.0 x 9.0 μm is cropped from the lower part of (a) to obtain a good data for analysis. Number of grains in the data set (b) is 50 grains with 1 complete grain.

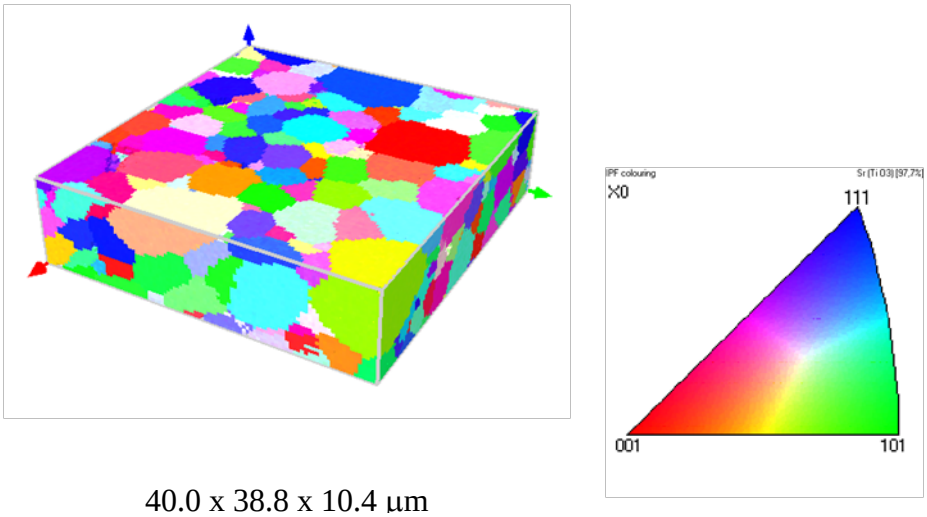

40.0 x 38.8 x 10.4 μm

Figure 4-18 Inverse pole figure (x-axis) colour mapping of 3D-EBSD data of STLN3 of volume 40.0 x 38.8 x 10.4 μm. Number of grains in the data set is 381 grains with 105 complete grains.

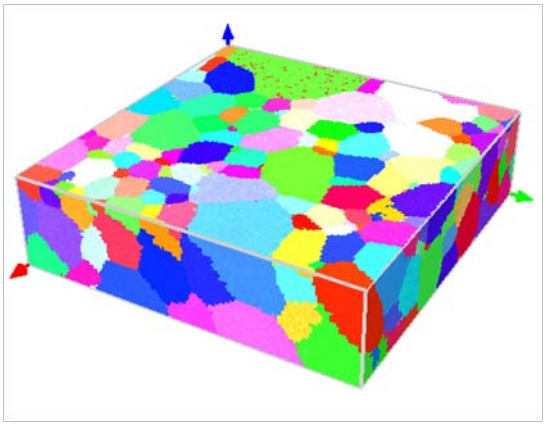

12.2 x 12.2 x 3.3 μm

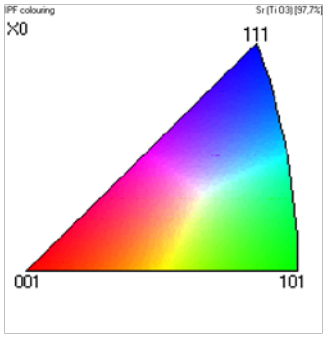

Figure 4-19 Inverse pole figure (x-axis) colour mapping of 3D-EBSD data of STLN4 of volume 12.2 x 12.2 x 3.3 μm. Number of grains in the data set is 279 grains with 55 complete grains.

2) Grain analysis

3D grain information was extracted from the 3D viewer to calculate average grain volume, spherical equivalent diameter, Grain boundary area per unit volume and average roughness. The calculated values are listed in Table 4-3. Since 3D-EBSd data volumes of STLN1 and STLN2 are very small compare to its grain size the average grain volume and spherical equivalent diameters cannot represent grain size of the samples. In STLN3 diameter measured from 3D-EBSD data (3.65 μm) is smaller than the value measured from 2D-EBSD data (7.51μ) because some 75% of grains in the 3D data are cut thus the remaining completed grains are small grains. Grain diameter of STLN4 in the 3D data is larger than the value measured from 2D data. This

might because high heterogeneous of grain size of the sample. Grain roughness of the four samples as in the same order.

Table 4-3 List of average grain volume spherical equivalent diameter grain boundary area per volume and roughness of STLNs

	STLN1	STLN2	STLN3	STLN4
Average grain volume (μm^3)	723.2	1594.8	42.2	1.73
Spherical equivalent diameter (μm)	8.2	10.3	3.65	1.20
Grain boundary area/volume (μm^{-1})	0.16	0.20	0.56	1.68
Average roughness	0.99	1.05	0.98	1.02

4.5 Conclusion

BSE images of the STLNs heavily heterogynous of the STLNs grain size. There was trouble in 3D-EBSD data collection of STLN1 and STLN2 due to its Largeness of grain size, average grain diameter 11.9 μm and 12.5 μm in STLN1 and STLN2 respectively. To obtain data volume of 5x5x1 grains of STLN1 and STLN2, it need approximately 9 days experiment and consumes a huge ion beam source. The most time consumption is for FIM milling. Using a modified beam profile high current ion beam can produce smooth surface in some degree available in the 3D-EBSD data collection. However it can damage the FIB device as occurred in this work. Signal quality of STLN4 is quite low thus the polishing technique in Chapter 3 was used in 3D-EBSD data collection. There is no dominate characteristic found in both 2D and 3D-EBSD investigation of grains and grain boundary. 3D-EBSD data of STLN3 and STLN4 were used in grain boundary relative energy and pressure calculation in Chapter 5.

Chapter 5. Relative grain boundary energy and pressure of strontium titanate

5.1 Introduction

One of the most frequently controlled microstructure parameters in materials processing is the grain size. The final grain size in materials is usually controlled by grain growth and optionally recrystallisation. Grain boundary migration and diffusion is the main process in grain growth and recrystallisation. Two types of grain boundary migrations may be distinguished (Upmanyu *et al*., 1998). The first type, the rate of grain boundary movement is controlled by diffusion flux of chemical species across the interface. In the second type, there is no net flux across the interface such that the composition on both sides of the boundary is unmodified by the motion of the boundary. It is known as conservative grain boundary migration (Sutton & Balluffi., 1995). The conservative grain boundary migration depends upon grain boundary structure, driving force and temperature (Sutton & Balluffi., 1995). The driving force involves grain boundary free energy and grain boundary curvature (Sutton & Balluffi., 1995). Grain boundary curvature can be expressed as radius of the circle best fitted to the grain boundary. More accurate grain boundary radius can be measure as radius of the sphere best fitted to the grain boundary in 3D.

Currently there is no complete theory to explain the grain boundary energy. However it can be measured in relative manner from microstructure and crystallographic information of the grain boundaries. EBSD is a tool to obtain such information of the grain boundaries. Examples of calculation of the relative energy using EBSD data are (Adams *et al*., 1999) (Li *et al*., 2009) and (Rohrer *et al*., 2010). From 3D-EBSD data, both grain boundary curvature and relative energy can be quantify generally using line segment method in combination with triangular surface mesh method (Khorashadizadeh *et al*., 2011,Khorashadizadeh *et al*., 2008).

A new 3D-EBSD grain boundary analysis technique called *elementary facet method* was purpose by Chou and Gholinia (Chou & Gholinia., 2010). The advantages of the method over the line analysis method is that the elementary facet method is simple to implement and is capable of generating more detailed grain boundary information. In this work, the technique to apply the elementary facet method to calculate relative grain boundary energy and pressure in 3D- EBSD data of STLN samples collected in Chapter 5.

5.2 Relative grain boundary pressure

The conservative grain boundary migration depends upon grain boundary structure, driving force and temperature (Sutton & Balluffi., 1995). Change in free energy of the system associated with the reduction in grain boundary area provides the driving force for the grain boundary migration. This driving force leads to the well-known result that grain boundaries migrate perpendicularly to their centre of curvature. The relationship between the driving force (p) grain boundary curvature (κ) and the grain boundary free energy per unit area (γ) is provided by the Gibbs-Thomson relation (Porter & Easterling., 1992):

$$p = \gamma\kappa \qquad 5\text{-}1$$

Assuming there is a best-fit spherical surface of radius R that fits the grain boundary, the curvature term in equation 6-1can be expressed in the form of R (Humphreys & Hatherly., 2004)

$$\kappa = \frac{2}{R} \qquad 5\text{-}2$$

Section 5.2.1 and 5.2.2 explain methods to measure grain boundary equivalent radius and relative grain boundary energy.

5.2.1 Grain boundary equivalent radius

In the elementary facet method each grain boundary is paved with facets parallel to x-plane y-plane and z-plane. Each facet has its own normal vector point outward the considering grain. At the beginning facets normal vectors are parallel to x y and z axes. By performing convolution of the normal vectors their directions are changed to the local averaging direction and this direction defines a new facet plane normal. More detail of the elementary facet method can find in (Chou & Gholinia., 2010). Direction distribution of facet normal vectors of a grain boundary after convolution contains information of curvature of the grain boundary. Figure 5-1 shows two grain boundaries of a grain of STLN exported from the program 3D grain boundary prototype version 1.0.0.2 (Oxford Instruments, London UK). The pole figure plot of normal vectors of a flat grain boundary, Figure 5-1(a), shows narrower distribution than the distribution of a curved grain boundary in Figure 5-1(b). The equivalent spherical radius (R) of a grain boundary can be determined from the direction distribution as explain bellow.

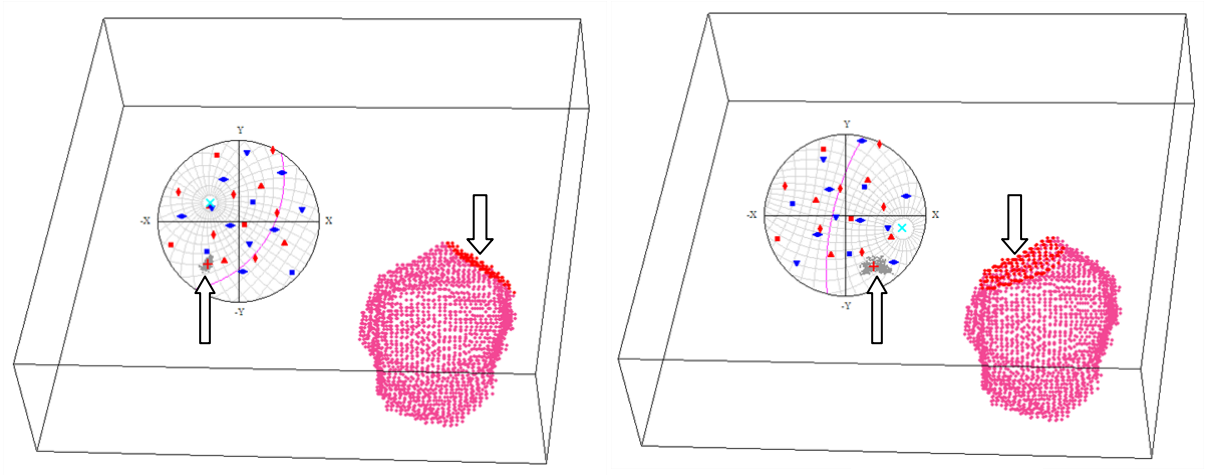

(a) (b)

Figure 5-1 Pole figure plot of facet normal vectors of a flat grain boundary in (a) shows condense direction distribution near the averaging direction that the plot of a curve grain boundary in (b). Both pictures were capture from the program 3D grain boundary prototype version 1.0.0.2 (Oxford Instruments, London UK).

Given $\bar{\boldsymbol{n}}$ to be the average unit normal vector of a complete grain boundary after convolution and $\boldsymbol{n_i}$ to be a unit normal vector of a facet *i* in the grain boundary after convolution as depicted in Figure 5-2. A deviation angle θ_i of the vector $\boldsymbol{n_i}$ from $\bar{\boldsymbol{n}}$ can be determined from arc cosine of their dot product.

$$\theta_i = \arccos\left(\bar{\boldsymbol{n}} \cdot \boldsymbol{n_i}\right) \qquad 5\text{-}3$$

The mean deviation angle ($\bar{\theta}$) of all normal vectors in the boundary around the average normal vector is

$$\bar{\theta} = \frac{\sum_i \theta_i S_i}{\sum_i S_i} \qquad 5\text{-}4$$

S_i is a surface area of a facet *i*.

A circular arc length (L_i) with radius *R* and subtending the angle θ_i is $R\theta_i$. The mean arc length ($\bar{L}$) of the grain boundary can be calculated by

$$\bar{L} = \frac{\sum_i R\theta_i S_i}{\sum_i S_i} = \frac{R\sum_i \theta_i S_i}{\sum_i S_i} \qquad 5\text{-}5$$

Equation 5-5 divided by equation 5-4 give the radius of curvature (*R*).

$$R = \frac{\bar{L}}{\bar{\theta}} \qquad 5\text{-}6$$

Detail to measurement of $\bar{L}$ and $\bar{\theta}$ is explained in section 6.3.2.

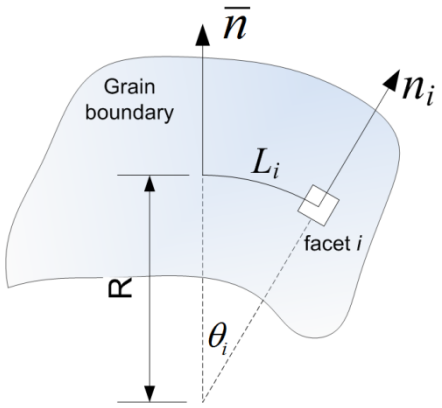

Figure 5-2 Diagram shows the average unit normal vector ($\bar{\boldsymbol{n}}$) a unit normal vector of a facet *i* ($\boldsymbol{n_i}$) a deviation angle (θ_i) a circular arc length (L_i) and the spherical equivalent radius *R* in 3D of a grain boundary.

5.2.2 Relative grain boundary energy

Adams et.al, (Adams *et al*., 1998) purposed a method to determinate relative grain boundary energy in 2D grain boundary map. The method in this study follows the trend in the paper but in 3D grain boundary map. Figure 5-3 shows parameters involving the calculation of relative grain boundary energy in 3D. g_a g_b and g_c are three grains that forming a triple junction line. γ_1 γ_2 and γ_3 are grain boundary energies of grain boundaries 1 2 and 3 respectively. $\boldsymbol{n}_1$ $\boldsymbol{n}_2$ $\boldsymbol{n}_3$ and $\boldsymbol{t}_1$ $\boldsymbol{t}_2$ $\boldsymbol{t}_3$ are normal vectors and tangential vectors of the grain boundaries near the triple junction line respectively. Force and torque balance at equilibrium described by Herring's equation (Herring., 1951):

$$\sum_{i=1}^{3}\left(\gamma_i \boldsymbol{t}_i + \frac{\partial \gamma_i}{\partial \emptyset_i}\boldsymbol{n}_i\right) = \mathbf{0} \qquad 5\text{-}7$$

Where $\emptyset_i$ is Grain boundary inclination of grain boundary *i*, measured anti-clockwise with respect to a reference direction.

The first term in equation 5-7 is force balance resulting from surface tension and the second term is torque balance involving grain boundary inclination. The surface tension mainly involves grain boundary free energy due to disorientation. The torque term involves grain

boundary plane inclination and it dominates in low angle grain boundary and some coincident site lattices grain boundaries. Five grain boundary parameters needed in calculation the torque term. Thus it can be computed only from 3D-EBSD data. However in this work there is limited period in developing program and calculation of the grain boundary energy and pressure due to the trouble of 3D-EBSD data collection. This work simplifies the calculation by neglecting the torque term in equation 5-7 since. The force balance term can be written in sine law form (Young's equation):

$$\frac{\gamma_1}{\sin\chi_1} = \frac{\gamma_2}{\sin\chi_2} = \frac{\gamma_3}{\sin\chi_3} \qquad 5\text{-}8$$

At any triple junction, in rectangular coordinate system equation 5-8 gives three linear homogeneous equations.

$$\begin{aligned} \gamma_1 \sin\chi_2 - \gamma_2 \sin\chi_1 &= 0 \\ \gamma_1 \sin\chi_3 - \gamma_3 \sin\chi_1 &= 0 \\ \gamma_2 \sin\chi_3 - \gamma_3 \sin\chi_2 &= 0 \end{aligned} \qquad 5\text{-}9$$

Thus for *N* triple junctions 3*N* system of linear homogeneous equations is obtained. Solving the linear homogeneous system quantifies the relative grain boundary energy. In 3D the situation is more complicated. Computing relative grain boundary energy from 3D-EBSD data is described in section 5.3.3.

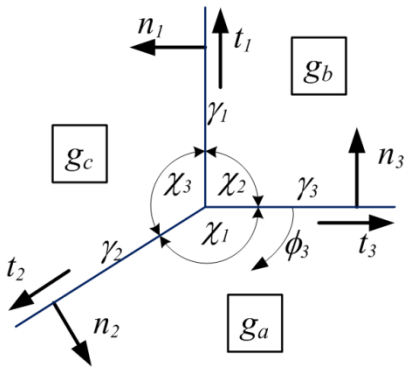

Figure 5-3 Diagram show a triple junction line formed by grain g_a g_b and g_c. γ_1 γ_2 and γ_3 are grain boundary energies. $\boldsymbol{n_1}$ $\boldsymbol{n_2}$ $\boldsymbol{n_3}$ and $\boldsymbol{t_1}$ $\boldsymbol{t_2}$ $\boldsymbol{t_3}$ are normal vectors and tangential vectors of grain boundaries 1 2 and 3 respectively. $\emptyset_3$ is inclination angle of grain boundary 3 with respected to crystal orientation of grain g_a.

5.3 Materials and methods

5.3.1 Materials

3D-EBSD data of STLN3 and STLN4 from Chapter 4 are used in this calculation. 3D-EBSD data of STLN3 and STLN4 were reconstructed using HKL 3D-viewer (Oxford Instruments, London UK) using threshold misorientation angle 3° and minimum grain size 27 voxels. Grain boundaries of the two data sets were reconstructed using the HKL 3D-viewer program (Oxford Instruments, London UK) and exported to Channel Text Files (*.CTF) for later analysis. A *3D grain boundary analysis program* (Oxford Instruments, London UK) was used to measure grain boundary misorientation in the CTF files. The misorientation will be used in calculation of grain boundary energy and pressure.

A program for performing facets convolution and calculation the grain boundary energy and pressure was developed using Microsoft visual C++ 2008 express edition.

5.3.2 Convolution radius and minimum number of facets

Convolution radius strongly affects the result of facets elements convolution especially from smaller grain boundaries that have few facets. Too large convolution radius can destroy the detail of the grain boundary. Figure 5-4 shows the effect of convolution radius. Colour red green and blue represent direction parallel to x y and z axes respectively. Colour components of mixed colour represent vector component of facet normal vector. In Figure 5-4 bottom right convolution radius is 15 steps yield a flat output while convolution radius 1 step colour gradient is not smooth. To determine the appropriate convolution radius and the minimum number of facets the following experiment is setup.

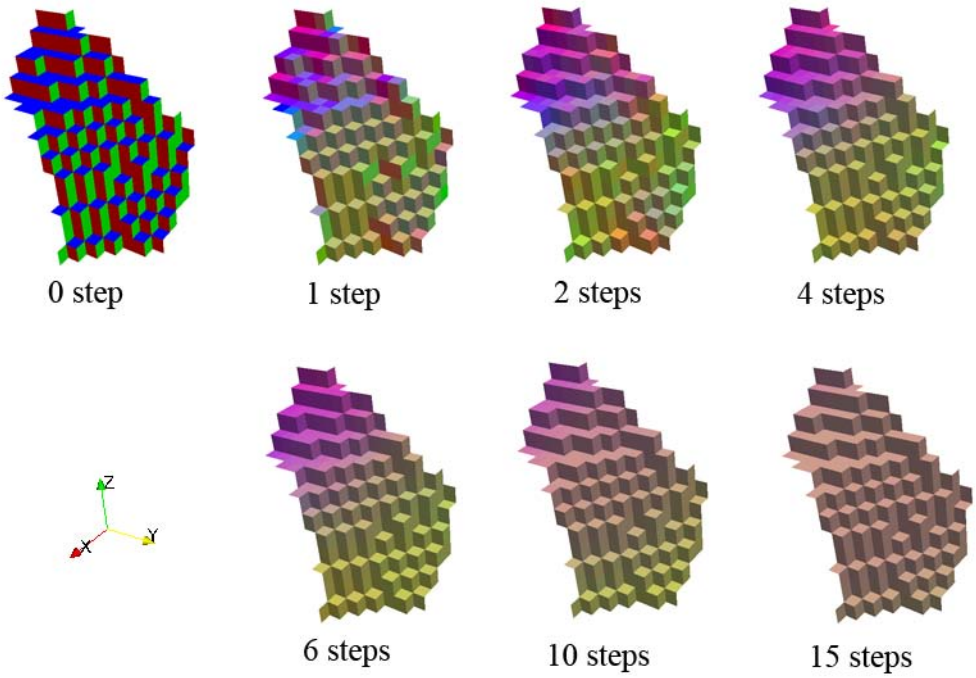

Figure 5-4 Picture shows effect of convolution radius 0 (no convolution), 1, 2, 6, 10 and 15 steps. Colour red green and blue represent direction parallel to x y and z axes respectively. Colour components of mixed colour represent vector component of facet normal vector.

A set of half sphere grain boundaries with radius 2, 3, 3.5, 4, 5, and 10 steps of voxels were generated (see Figure 5-5) to study appropriated convolution radius and minimum number of facets for facet convolution. Average deviation angle (equation 5-4) and grain boundary smooth area (equation 5-10) defined by Chou (Chou & Gholinia., 2010) are used as evaluation parameters.

$$Smooth\ area = S_{x0}\sum_i n_x(i) + S_{y0}\sum_j n_y(j) + S_{z0}\sum_k n_z(k) \qquad 5\text{-}10$$

S_{x0}, S_{y0} and S_{z0} are facet areas perpendicular to x, y and z axes respectively and $n_x(i)$, $n_y(j)$ and $n_z(k)$ are x, y and z component of normal unit vectors of facet *i*, *j* and *k* respectively. The term $S_{x0}n_x(i)$ in equation 5-10 is a projection of S_{x0} on the plane perpendicular to the normal vector $\boldsymbol{n}(i)$ after convolution. Thus the term $S_{x0}\sum_i n_x(i)$ is the total projection area of all x-facets on the plane perpendicular to their normal vectors. For more information about smooth area please see (Chou & Gholinia., 2010).

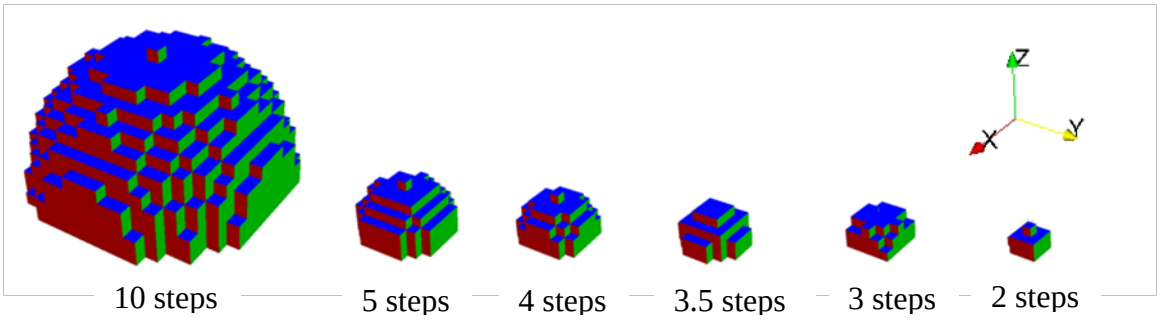

Figure 5-5 The half sphere grain boundaries of radius 2, 3, 3.5, 4, 5 and 10 steps of voxels used in determination of an appropriate convolution radius and its corresponding minimum facet numbers.

5.3.3 Grain boundary curvature measurement

To compute spherical equivalent radius of a grain boundary (equation 5-6) we need to know its mean deviation angle ($\bar{\theta}$) and mean arc length ($\bar{L}$). The mean deviation angle can be computed from equation 5-4 however the mean arc length cannot be computed directly since the radius of curvature (R) is unknown. Iteration method is used to determine the radius of curvature as described below.

1) Determination the average position of all facets in the boundary.
2) Compute the average normal vector (see Figure 5-6(a)).
3) Determine the central facet of the boundary by calculating the distance (a_i) from each facet centre to the line passing the average position and parallel to the average normal vector. The facet that has its centre closest to the line is the central facet.
4) Since the radius R is unknown, use distance (d_i) (see Figure 5-6(a)) from centre of the central facet to centre of a facet i as starting arc length.
5) Calculate mean arc length of the boundary using equation 5-11 instead of equation 5-5.

$$\bar{L} = \frac{\sum_i d_i S_i}{\sum_i S_i} \qquad 5\text{-}11$$

6) Calculate the radius of curvature from equation 5-6.
7) Use the resulting radius to recalculate mean arc length $\bar{L}$ from equation 5-5.
8) Repeat 6) and 7) until the radius no longer change as the flowchart in Figure 5-6 (b).

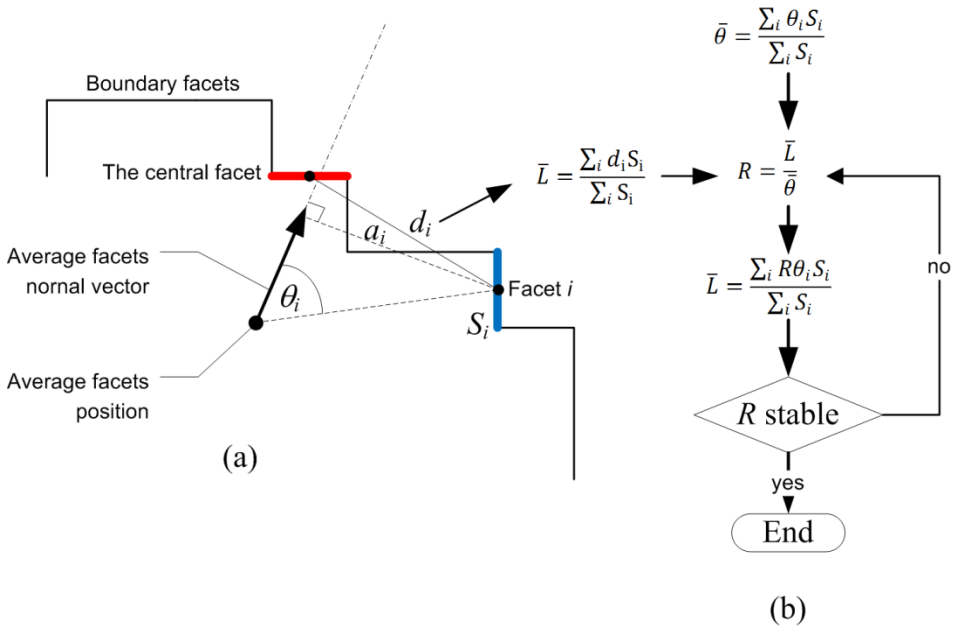

Figure 5-6 Schematic shows (a) parameters in calculate the starting arc length $\bar{L}$. (b) is a flowchart for calculation R.

5.3.4 Relative grain boundary energy measurement

Process to computed relative grain boundary energy from 3D grain boundaries is described below.

1) Search for triple junction lines.

In 3D triple junctions become lines. Voxel scan in the whole data set is performed to check if any facet of any voxel connects to any triple junction line. As an example in Figure 5-7(a), where a triple junction found, facets that connect to the junction (blue facets) are marked as triple junction facets. The red facet in Figure 5-7(a) is an internal grain facet thus it isn't mark. In the case of quadruple junction found (see Figure 5-7(b)) no facet is marked.

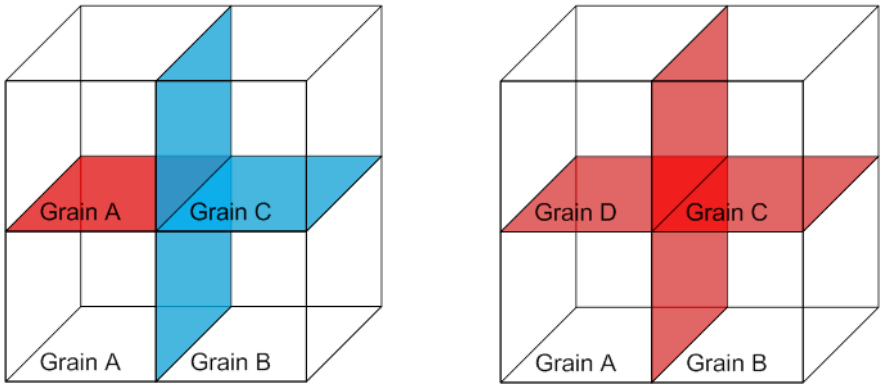

(a) (b)

Figure 5-7 Diagram (a) shows an example of four voxels at a triple junction of grain A B and C. In this case, blue facets are marked as triple junction facets while the red facet is not marked. In the case of quadruple junction (b) no facet is marked.

2) Determination of average normal vectors.

At each triple junction line, normal vector of the marked facets in each grain boundary are averaged. Blue band in Figure 5-8 indicated the region of facets that have been marked as triple junction facets in each grain boundary. Width of the bands is 1 facet. $\boldsymbol{n_1}$ $\boldsymbol{n_2}$ and $\boldsymbol{n_3}$ are the averaged normal vectors in each band.

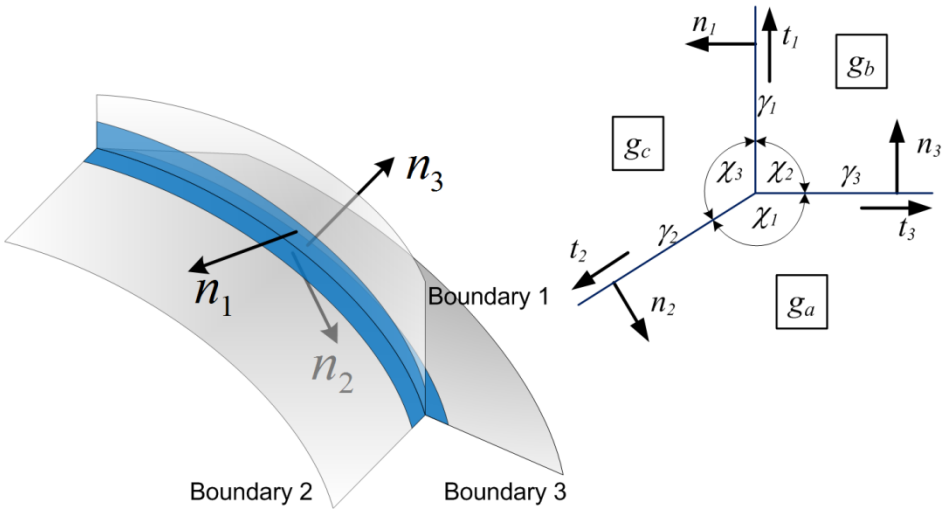

Figure 5-8 Picture shows a triple junction line in 3D. The blue bands in each grain boundary indicated the region of facets that are marked as triple junction facets. $\boldsymbol{n_1}$ $\boldsymbol{n_2}$ and $\boldsymbol{n_3}$ are average normal vector of the marked facets.

3) Determination of relation equations of grain boundary energies.

Young's law (equation 5-8) apply for three forced balancing in 2D. In 3D, three forces are not need to lie on the same plane. However at equilibrium it can be assumed that three surface tensions act on a triple junction are lie on or nearly on the same plane. By this assumption the dihedral angles in equation 5-8 and 5-9 can be computed from normal vectors instead of tangential vectors. As illustrated in Figure 5-9(a) and (b) when three tangential vectors $\boldsymbol{t}_1$ $\boldsymbol{t}_2$ and $\boldsymbol{t}_3$ lie on the same plane their associated normal vectors $\boldsymbol{n}_1$ $\boldsymbol{n}_2$ and $\boldsymbol{n}_3$ can be used to form the same configuration of force directions. Therefore the dihedral angles are calculated from dot product of the normal vectors.

$$\begin{aligned} \chi_1 &= \cos^{-1}(\boldsymbol{n}_2 \cdot \boldsymbol{n}_3) \\ \chi_2 &= \cos^{-1}(\boldsymbol{n}_1 \cdot \boldsymbol{n}_3) \\ \chi_3 &= \cos^{-1}(\boldsymbol{n}_1 \cdot \boldsymbol{n}_2) \end{aligned} \qquad 5\text{-}12$$

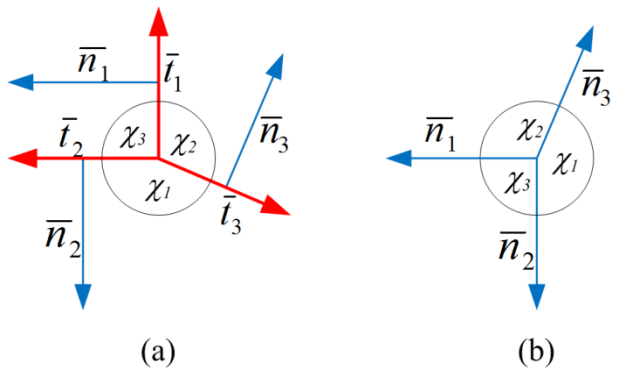

Figure 5-9 Diagram illustrate that normal vectors $\boldsymbol{n}_1$ $\boldsymbol{n}_2$ and $\boldsymbol{n}_3$ of grain boundaries at triple junction from (a) can form the same direction configuration (b) as formed by the tangential vectors $\boldsymbol{t}_1$ $\boldsymbol{t}_2$ and $\boldsymbol{t}_3$ when the three tangential vectors are on or nearly on the same plane.

4) Averaging of energy relations.

Neglecting the effect of grin boundary inclination then assume that relative grain boundary energy depends upon only misorientation, grain boundaries with the same misorientation have the same energy. By binning misorientation, assuming *n* bins, the system have *n* values of grain boundary energies. Each triple junction gives three linear relations of grain boundary energies (equation 5-9). Since the relation is linear, relations the same energy pairs found in different triple junction can be added and averaged. Assuming relations of energies γ_a and γ_b are found in *K* triple junctions the averaging relation of the energies γ_a and γ_b is

$$\gamma_a \overline{\sin}\chi_b - \gamma_b \overline{\sin}\chi_a = \gamma_a \sum_{k=1}^{K} \sin\chi_b^k - \gamma_b \sum_{k=1}^{K} \sin\chi_a^k = 0 \qquad 5\text{-}13$$

For *n* bins of energies, there are *n*(*n*-1)/2 possible average energy relations as illustrated in Table 5-1. Relation between energies $\gamma_a - \gamma_b$ and $\gamma_b - \gamma_a$ are treated as the same relation. Some relation might be missing if number of triple junction is not enough.

Table 5-1 List of possible averaging relations of grain boundary energy in *n* energy bins

Relations of γ_1 and the others	Relations of γ_2 and the others (exclude γ_1)	. . .	Relation of γ_{n-1} and the others γ_n
$\gamma_1\overline{\sin}\chi_2 - \gamma_2\overline{\sin}\chi_1 = 0$ $\gamma_1\overline{\sin}\chi_3 - \gamma_3\overline{\sin}\chi_1 = 0$ . . . $\gamma_1\overline{\sin}\chi_{n-1} - \gamma_{n-1}\overline{\sin}\chi_1 = 0$ $\gamma_1\overline{\sin}\chi_n - \gamma_n\overline{\sin}\chi_1 = 0$	$\gamma_2\overline{\sin}\chi_3 - \gamma_3\overline{\sin}\chi_2 = 0$ $\gamma_2\overline{\sin}\chi_4 - \gamma_4\overline{\sin}\chi_2 = 0$ . . . $\gamma_2\overline{\sin}\chi_n - \gamma_n\overline{\sin}\chi_2 = 0$	. . .	$\gamma_{n-1}\overline{\sin}\chi_n - \gamma_n\overline{\sin}\chi_{n-1} = 0$
No. Equations = *n*-1	No. Equations = *n*-2		No. Equations = 1
Total No. Equation = *n*(*n*-1)/2			

5) Solve of system linear equation.

The final step is to solve the system of linear equations in Table 5-1 by setting up and solving matrix equation. Kaczmarz iteration method is used to solve the equation. There are many literatures about Kaczmarz iteration method found in internet such as (Anonymous , 2013). More detail of Kaczmarz iteration in computing of grain boundary energy in 2D can be found in Adams et.al, (Adams *et al*., 1998) Consequently relative grain boundary pressure can be computed from equation 5-1.

$$\mathbf{AE} = \mathbf{0} \qquad 5\text{-}14$$

A is $\frac{n(n-1)}{2} \times n$ matrix, **E** is energy vector and **0** is zero vector as shown below.

$$\mathbf{A} = \begin{bmatrix} \overline{\sin}\chi_2 & -\overline{\sin}\chi_1 & 0 & ... & 0 \\ \overline{\sin}\chi_3 & 0 & -\overline{\sin}\chi_1 & 0 & 0 \\ ... & ... & ... & ... & ... \\ 0 & 0 & \overline{\sin}\chi_n & 0 & \overline{-\sin}\chi_{n-2} \\ 0 & 0 & 0 & \overline{\sin}\chi_n & -\overline{\sin}\chi_{n-1} \end{bmatrix} \qquad 5\text{-}15$$

$$\mathbf{E} = \begin{bmatrix} \gamma_1 \\ \dots \\ \gamma_n \end{bmatrix} \qquad 5\text{-}16$$

$$\mathbf{0} = \begin{bmatrix} 0 \\ \dots \\ 0 \end{bmatrix} \qquad 5\text{-}17$$

5.4 Result and discussion

5.4.1 Convolution radius and minimum number of facets

The 6 half sphere grain boundaries (Figure 5-5) were convoluted with convolution radius 1 to 10 steps. Then the mean deviation angle (equation 5-4) and smooth areas (equation 5-10) of the convoluted boundaries were calculated. The mean deviation angles were used to indicate degree of curvature of the boundaries. The lower mean deviation angle the flatter boundary and zero mean deviation angle means totally flat boundary. Figure 5-10 shows the mean deviation angle plotted as a function of convolution radius. The theoretical value of mean deviation angle of half sphere is 1 radian or 57.29°. The dashed lines in the graph in Figure 6-10 indicate ±10% deviation from 57.29°. In the graph mean deviation angles of smaller boundaries decreased more rapidly than larger boundaries while the convolution radius increased. Considering smallest half sphere boundaries (radius 2 steps), to keep the error of mean deviation angle in the interval ±10% the convolution radius must be smaller than approximately 2 steps while for the half sphere boundary radius of 10 steps the convolution can be increased to approximately 7.5 steps. Therefore the appropriated convolution radius depends upon boundary size (in steps).

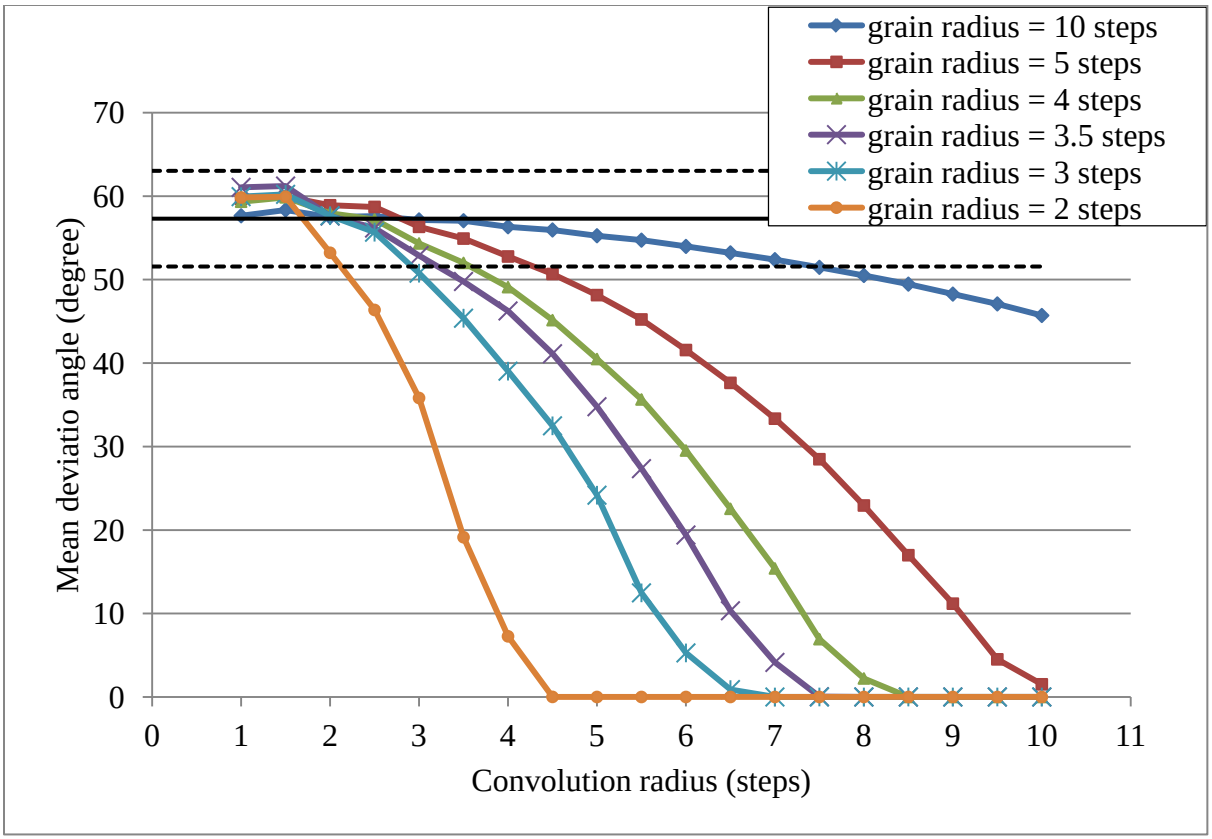

Figure 5-10 Mean deviation angle plots as a function convolution radius of the half sphere grain boundaries of radius 2, 3, 3.5, 4, 5 and 10 steps.

Figure 5-10 shows plot of the ratio of smooth area per real area of the half sphere boundaries as a function of convolution radius. The real surface area of half sphere is $2\pi r^2$, r is radius of the half sphere. The dashed lines indicate 10% error interval of the ratio. Consider boundary radius 10 steps in the region convolution radius between 2 to 3.5 steps where its mean deviation angle best match to the real value (see Figure 5-9), its smooth area in Figure 5-10 is higher than its real area in the whole region. The same situation happens to the other boundaries in the region that their mean deviation angle best fit to the real value. This mean that the smooth area is over-estimated as defined by (Chou & Gholinia., 2010) (equation 5-10). Since the models in this study are half sphere boundaries the over estimation in this study cannot be used to compensate in the real grain boundary analysis. In the real situation where almost all grain boundary curvatures likely are less than the half sphere curvature, the over estimation of smooth area should smaller. In the grain boundary radius 10 steps the smooth area is approaching the real value while the convolution radius increased. However the mean deviation angle in Figure 5-9 indicates its shape getting away from half sphere.

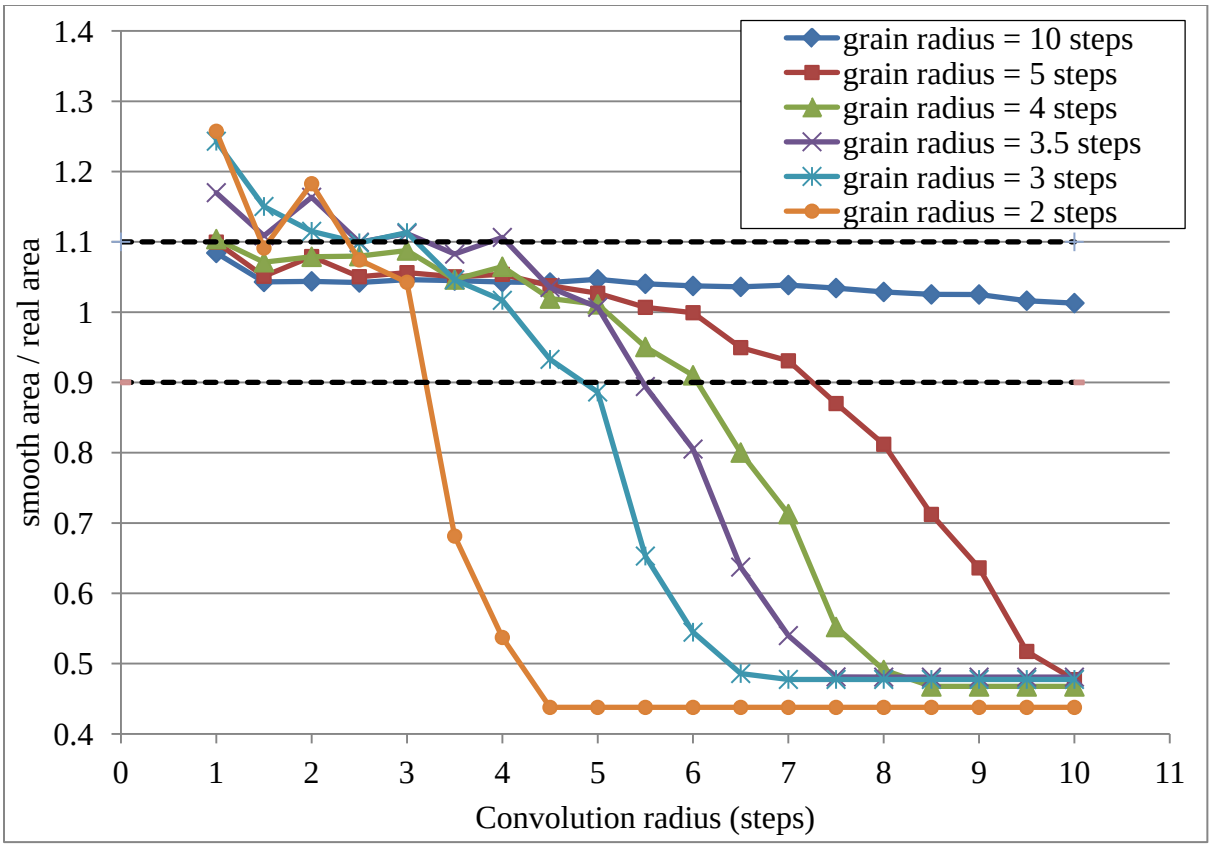

Figure 5-11 Plot of ratio of smooth area and real area of the half sphere boundaries as a function of convolution radius.

Since grain sizes of STLN3 and STLN4 are quite heterogeneous the convolution are chosen to match a wide range of grain boundary sizes. There are no possible convolution radius to keep the mean deviation angle (Figure 5-10) and smooth area (Figure 5-11) within 10% error for boundary radius 2.0 and 3.0 steps. Thus in this study the boundary radius 3.5 steps is selected as a threshold size. The convolution radius that maintains the mean deviation angle and smooth area errors of boundary radius 3.5 steps within 10 % is in the range 2.5 to 3.5 steps. Surface area of half sphere radius 3.5 steps is 77 steps^2. Thus in this study the convolution radius is chosen in the range 2.5 to 3.5 steps and the minimum number of facets in grain boundary is 75 facets.

5.5 Determination of radius of curvature

Six half sphere grain boundaries radius 2.0 2.5 3.0 4.0 5.0 and 10 steps (see Figure 5-5) were used to determine error of grain boundary radius calculation. The six boundaries were convoluted with convolution radius 2.5 steps. Figure 5-12 is a plot of calculated radius divided by real radius of the six boundaries. The error in the half sphere radius 2.0 is almost 63% and reduces significantly to 14% in the half sphere radius 2.5 steps. In real grain boundaries it is

expected to be less curvy than the half sphere boundaries. The error of radius of curvature computed by this method should lower that shown in the graph. Based on the half sphere boundary model, grain boundaries with a diameter equal to or larger than $2 \times convolution\ radius$ might be expected to have an error lower than 10 %. The calculation error reduces while boundary size increase since the larger boundary can maintain detail better.

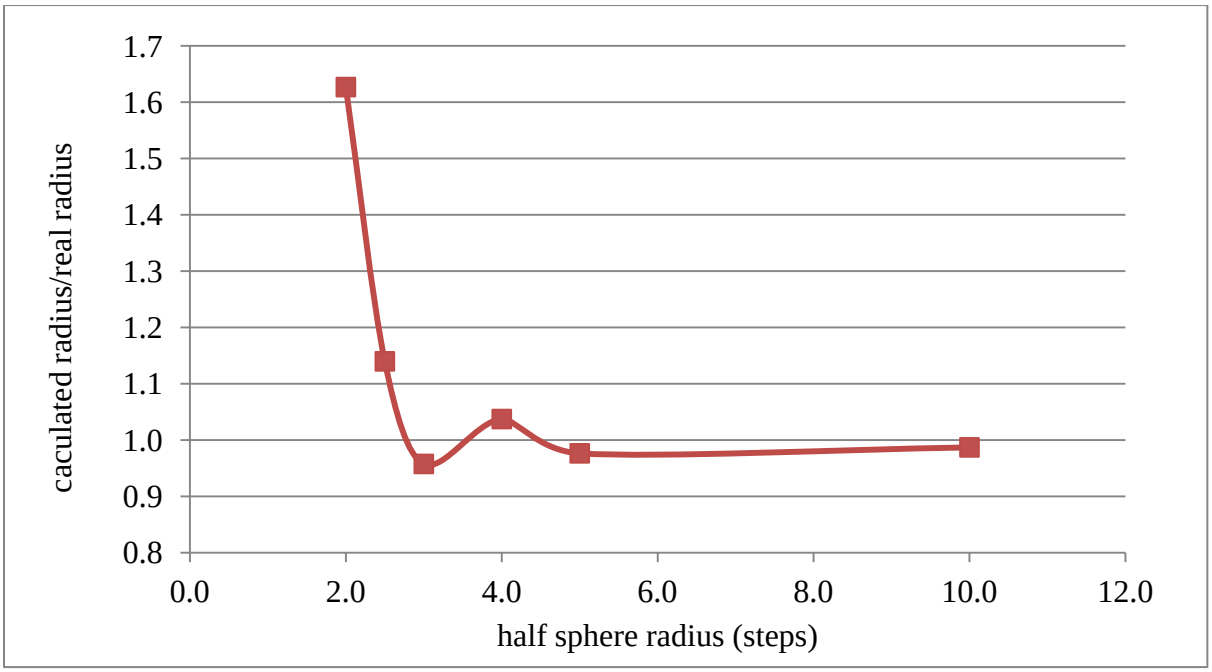

Figure 5-12 A plot shows calculated grain boundary radius divided by real radius of six half sphere boundary radius 2.0 2.5 3.0 4.0 5.0 and 10 steps.

There are 3890 and 2700 grain boundaries in STLN3 and STLN4 3D-EBSD datasets. There are 642 and 853 boundaries have more than 75 facet in the data set of STLN3 and STLN4 respectively. Spatial resolution in STLN3 data set is quite low compare to STLN4 data set thus there are only 642 boundaries that larger than the threshold. In this study all edge contacted boundaries in the dataset are treated as complete boundaries in the dataset. Thus radius of curvature of the edge contacted boundaries theoretically larger than its real radius. In contrast its surface area is smaller than the real area. Figure 5-13 and Figure 5-14 are histograms of grain boundary equivalent radius of STLN3 and STLN4 and Figure 5-17 and Figure 5-18 are histograms of grain boundary equivalent radius of STLN3 and STLN4 respectively. Average grain boundary equivalent radius of STLN3 and STLN 4 are 9.11 μm and 1.81 μm with standard deviation 3.2 μm and 0.72 μm respectively. Average smooth area of STLN3 and STLN4 are 10.22 μm^2 and 0.87 μm^2 with standard deviation are 5.14 μm^2 and 0.73μm^2 respectively.

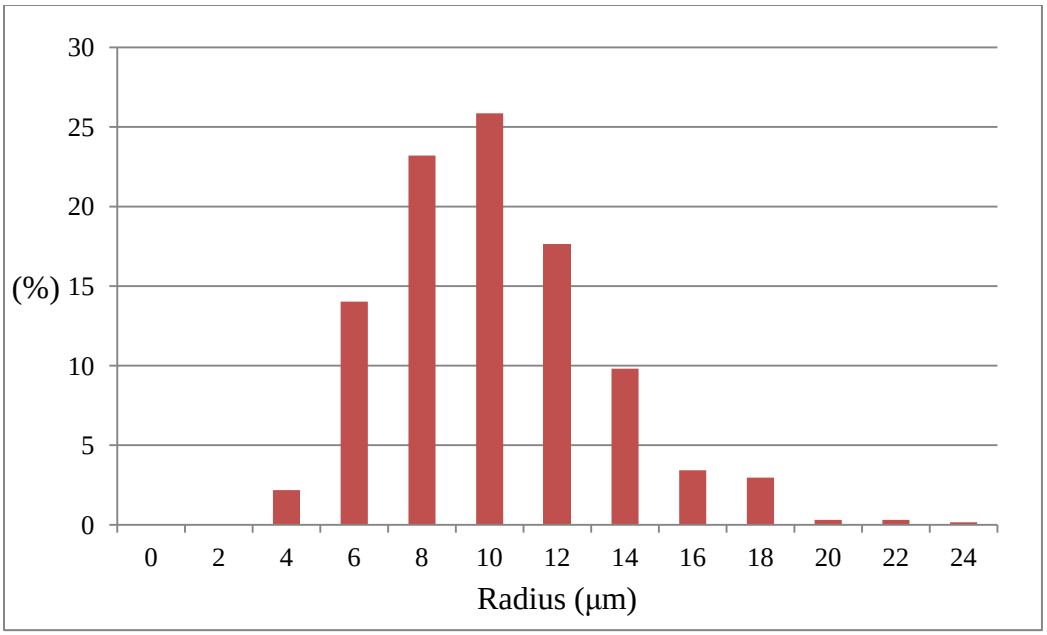

Figure 5-13 Histogram illustrates distribution of grain boundary spherical equivalent radius of STLN3.

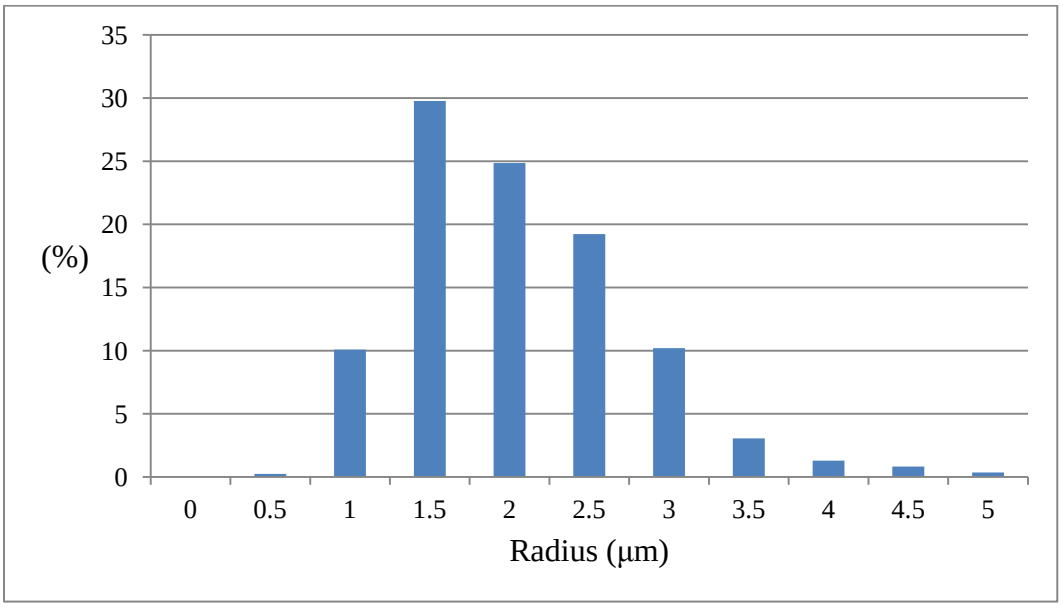

Figure 5-14 Histogram illustrates distribution of grain boundary spherical equivalent radius of STLN4.

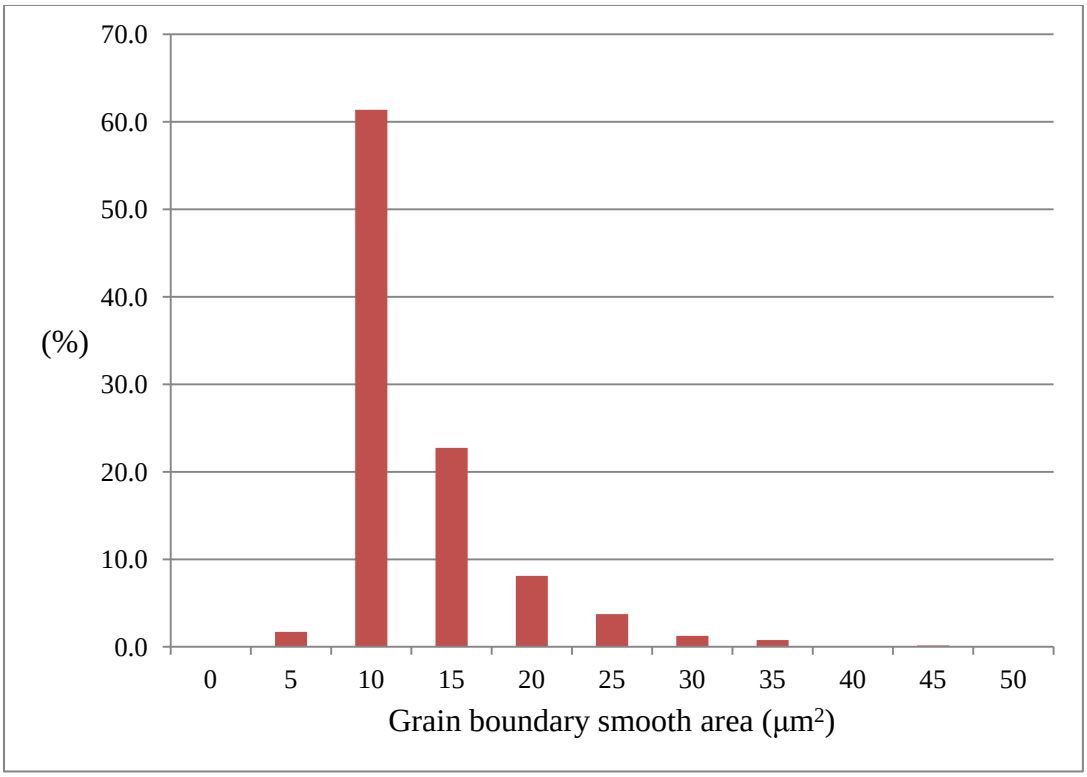

Figure 5-15 Histogram illustrates distribution of grain boundary smooth area of STLN3.

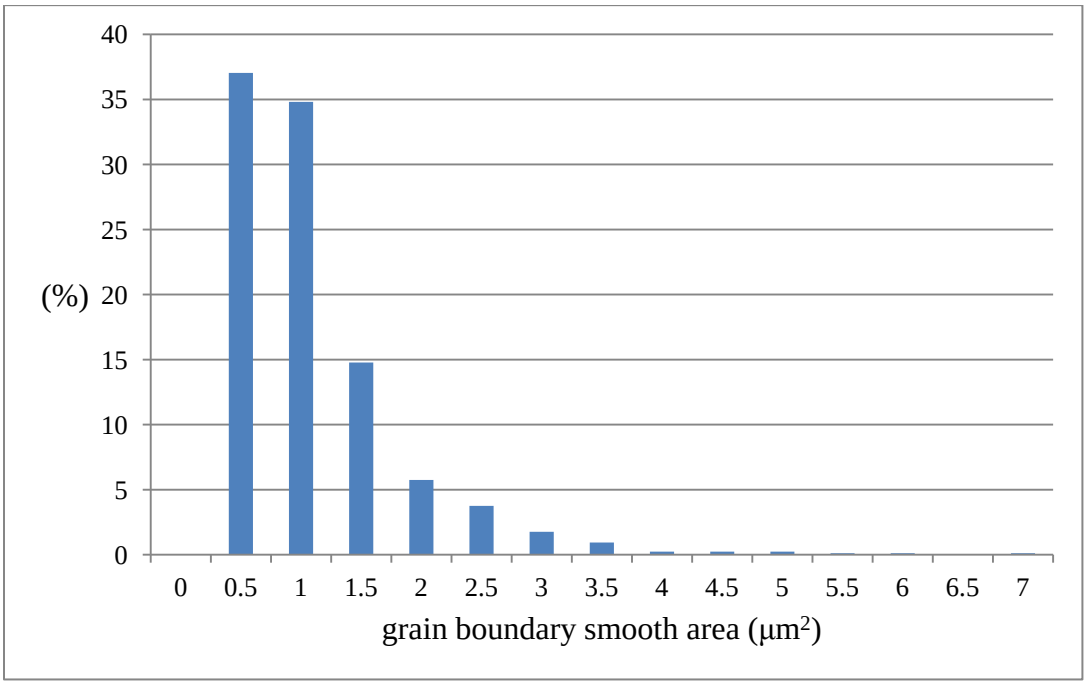

Figure 5-16 Histogram illustrates distribution of grain boundary smooth area of STLN4.

5.5.1 Grain boundary energy and pressure

Dihedral angles play an important role in grain boundary energy calculation using Young equations. In 2D, the angular sum of dihedral angles around a triple junction is 360°. However in 3D angular summation of angles between three tangential vectors (or normal vectors) of grain boundaries at triple junction is equal or less than 360°. The sum is 360° when the three tangential vectors (or normal vectors) are laying in the same plane otherwise the summation is less than 360°. Figure 5-17 is a plot of the angular sum of three grain boundary normal vectors around 1993 junctions in 3D-EBSD data set of STLN4 in order from small to large. The value close to 360° indicates that the three normal vectors are nearly on the same plane while the value far from 360° means the three vectors form a cone. Triple junctions that give the best and the worst angular summation in the graph sum are shown in Figure 5-16 (a) and (b) respectively. In Figure 5-18 three grain boundaries at each junction are separated by colour red green and blue. The angular summation of the junction (a) is 357.8° and the junction (b) is 264.8°. It can be observed that three boundaries forming the junction (a) are quite flat while the boundaries forming the junction (b) are heavy curvy. Mean deviation angle of red green and blue boundaries of the junction (a) are 6.8° 9.7° and 5.5°, respectively, and in the junction (b) are 16.7° 15.6° and 17.2°, respectively. In the junction (b), normal direction of facets contacted to the junction can be heavy distorted by convolution while the distortion in the junction (a) must be smaller. In this study to be available the energy calculation using the Young's law, the angular summation is cut off at 350° since the Young's law is apply to force balance in 2D.

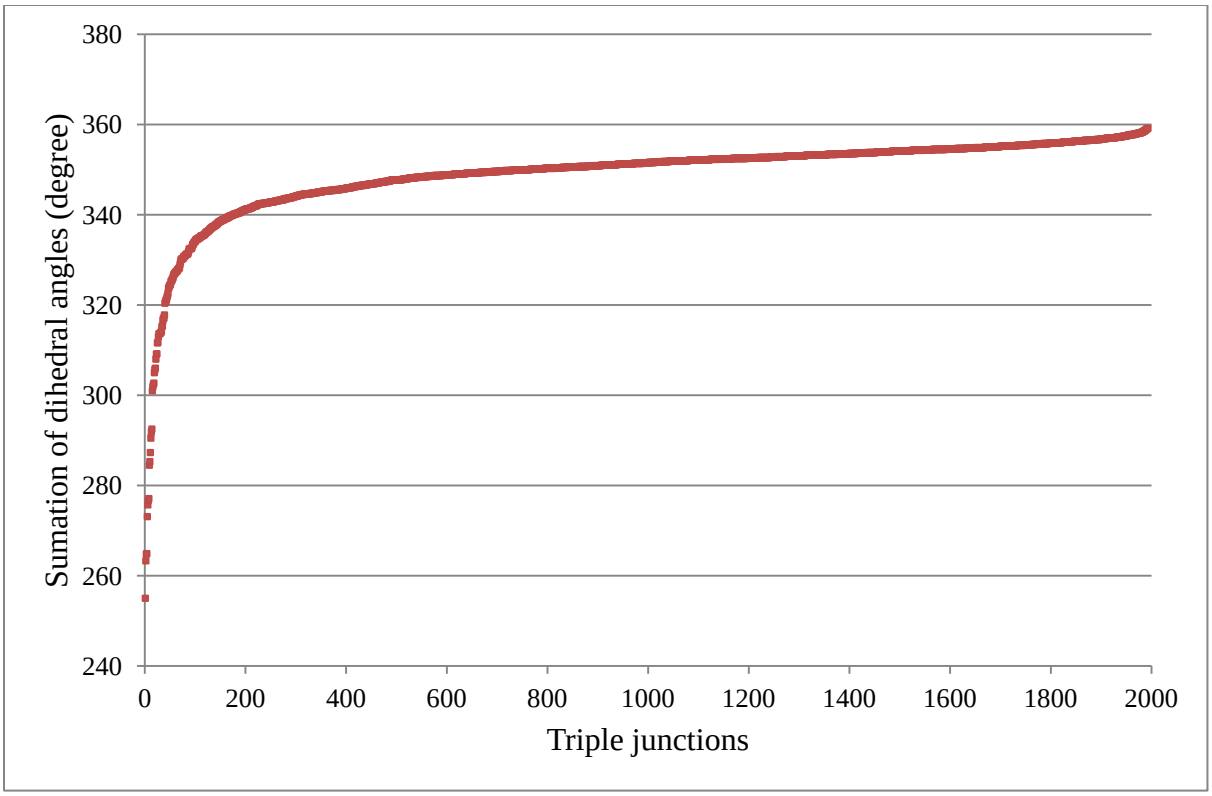

Figure 5-17 Plot of angular summation of angles between three normal vectors of grain boundaries at 796 junctions in 3D-EBSD data set of STLN4 in order from small to large.

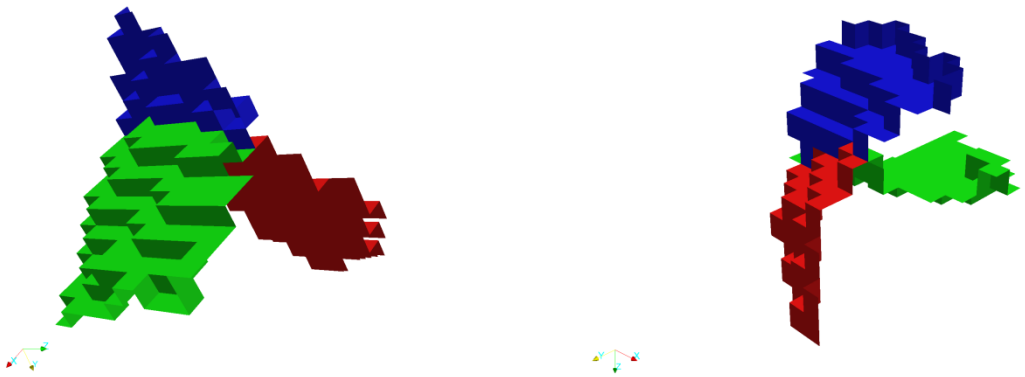

(a) (b)

Figure 5-18 Picture shows two triple junctions in 3D-EBSD data set of STLN4. Three grain boundaries in each junction are separated by colour red green and blue. (a) is the junction that gives the highest summation of dihedral angles at 357.8° and (b) is the junction that give the lowest summation of dihedral angles at 264.8°.

There are 1993 and 2904 triple junctions in 3D grain boundary maps of STLN3 and STLN4. After filtering out by grain boundary size (greater than 75 facets) and dihedral angular summation (greater than 350°), there are 472 and 232 triple junctions remaining in the data set of STLN3 and STLN4 respectively. Energies are grouped in to 32 misorientation bins with the bin size 2°. Thus the energy range covers 0° to 64° misorientation. Figure 5-17 and Figure 5-18 show the calculated relative grain boundary energies versus misorientation with convolution radius 2.5 3.0 and 3.5 steps of STLN3 and STLN4 respectively. In both data sets, there are rare energy relations in the matrix **A** in the region that misorientation lower than approximately 30° especially in STLN3. This can be explained by random misorientation distribution of the samples. Figure 5-19 (a) and (b) are the misorientation distributions of STLN3 and STLN4 without filtering by grain size and diheral angular summation. Since there is low amount of grain boundaries at low misorientation (in this case smaller than 30°) and even lower amount due to the filtering many of energy relations at low misorientation are missing. Therefore in the region of misorientation lower than approximately 30° the calculation results are not reliable.

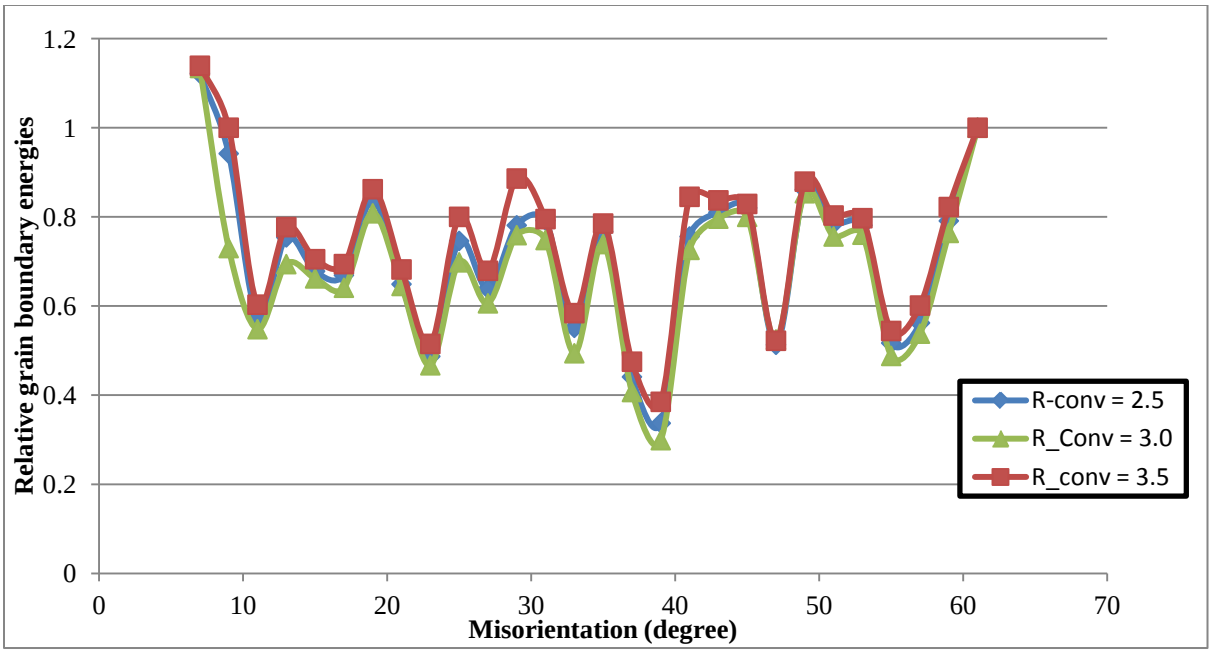

Figure 5-19 Relative grain boundary energy of STLN3 with convolution radius 2.5 3.0 and 3.5 steps.

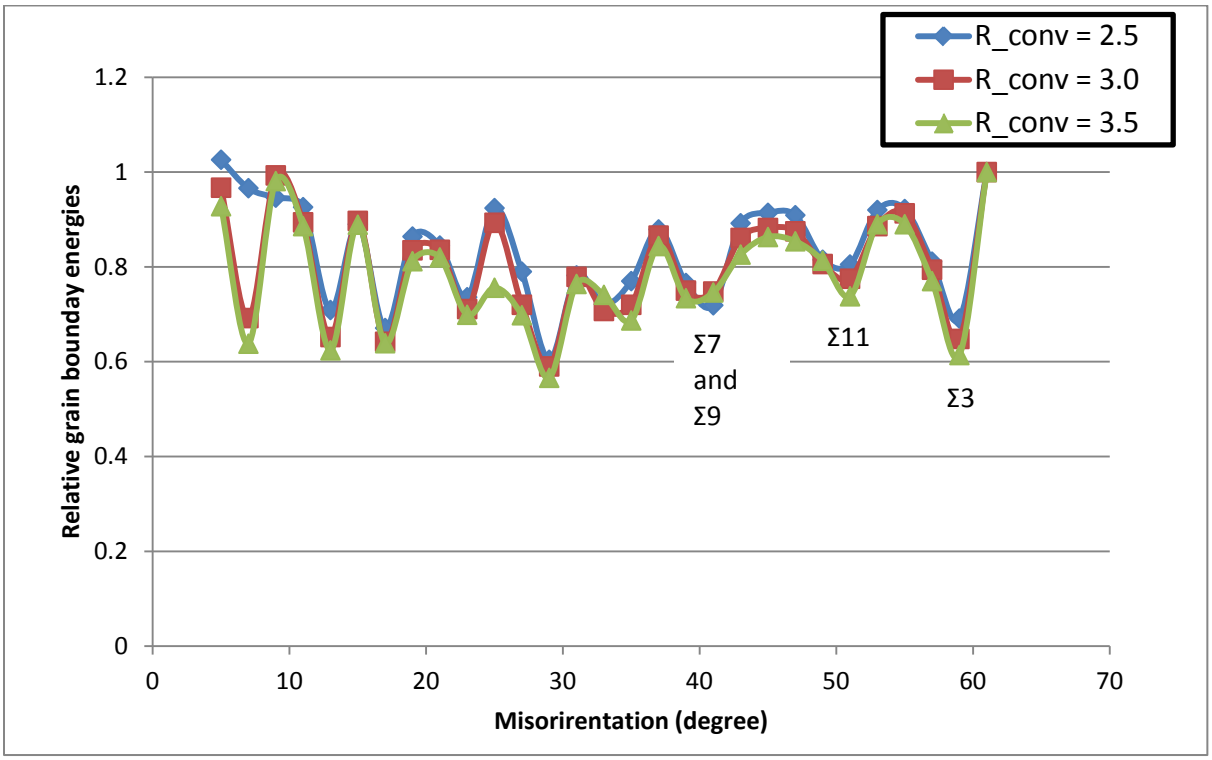

Figure 5-20 Relative grain boundary energy of STLN4 with convolution radius 2.5 3.0 and 3.5 steps.

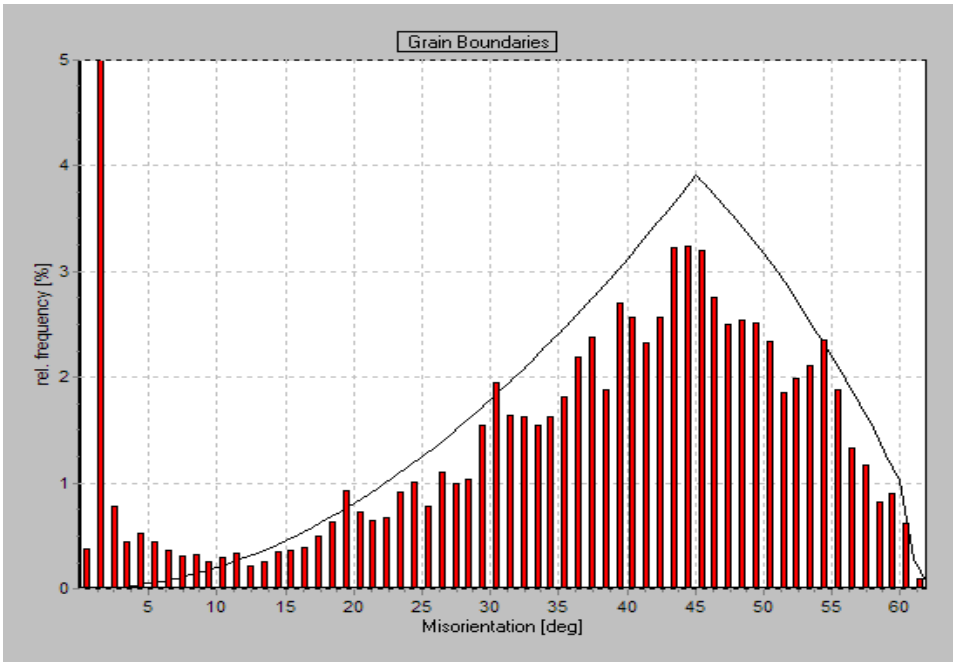

(a)

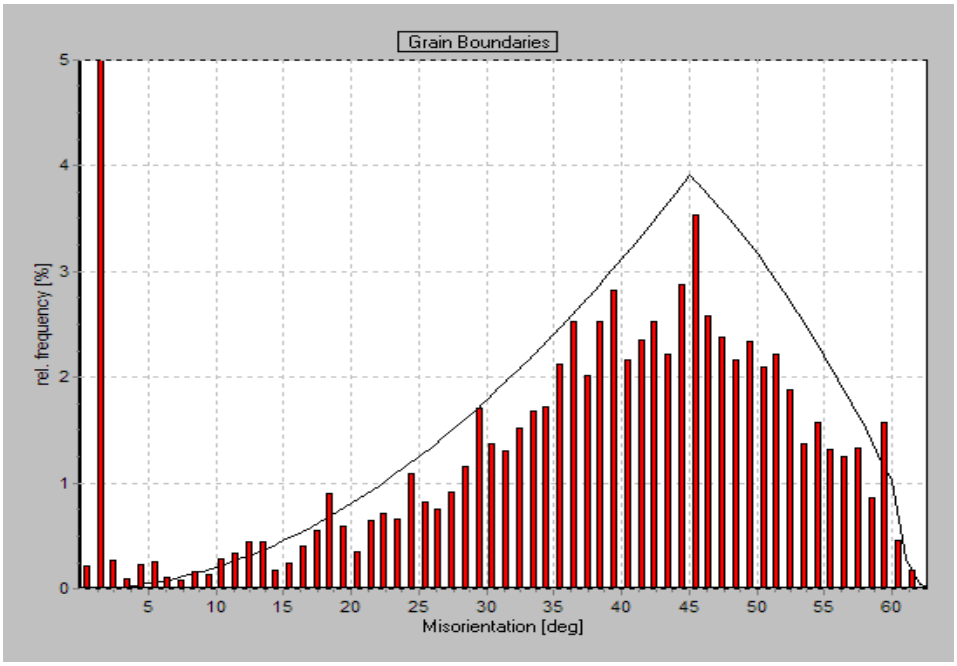

(b)

Figure 5-21 Graphs illustrate random misorientation distribution of (a) STLN3 and (b) STLN4.

Consider the region that misorientation is higher than 30° in STLN4, there are three notches (labelled as Σ3 Σ7 Σ9 and Σ11in Figure 5-20) that are corresponding to position of coincidence site lattice (CSL) boundaries. Table 5-2 shows the CSL boundaries, Σ3 Σ5 Σ7 Σ9 Σ11 and Σ15, found in STLN4. Column two of the table is a list of their positions in a misorientation distribution plot. Column three and four are numbers of grain boundaries and CLSs boundaries found in the region ±5° from the center positions. The last column is percentage of the CSL boundaries in the regions. Since energy of the CSL boundaries is lower than normal boundaries at the same misorientation, averaged energies at the positions are decreased. In contrast, In STLN3 (Figure 5-19), the CSL positions cannot be identified even in the region misorientation greater than 30°. Insufficiency of triple junctions in the data set cans cause the unreliable result. Angular summation of diheral angle less that 360° can involve the calculation error. Therefore in calculation of grain boundary pressure only energies of STLN4 in the region misorientation higher than 30° were used.

Table 5-2 List of Coincident Site Lattices found in 3D-EBSD data set of STLN4.

CSLs	Misorientation angles (degree)	No. GBs In [MO±5°]	No. CLS GBs in [MO±5°]	CLS% in [MO±5°]
Σ3	60.0	90	20	22.2%
Σ5	36.8	232	13	5.6%
Σ7	38.2	258	7	2.7%
Σ9	38.9	258	13	5.0%
Σ11	50.5	260	11	4.2%
Σ15	48.2	278	4	1.4%

Figure 5-22 shows three histograms in the same plot of relative grain boundary pressure of STLN4, of only the boundaries that have misorientation higher than 30°, using convolution radius 2.5 3.0 and 3.5 steps. There is no significant difference of the three cases. Triple junctions in both STLN3 and STLN4 are quite low in this calculation.

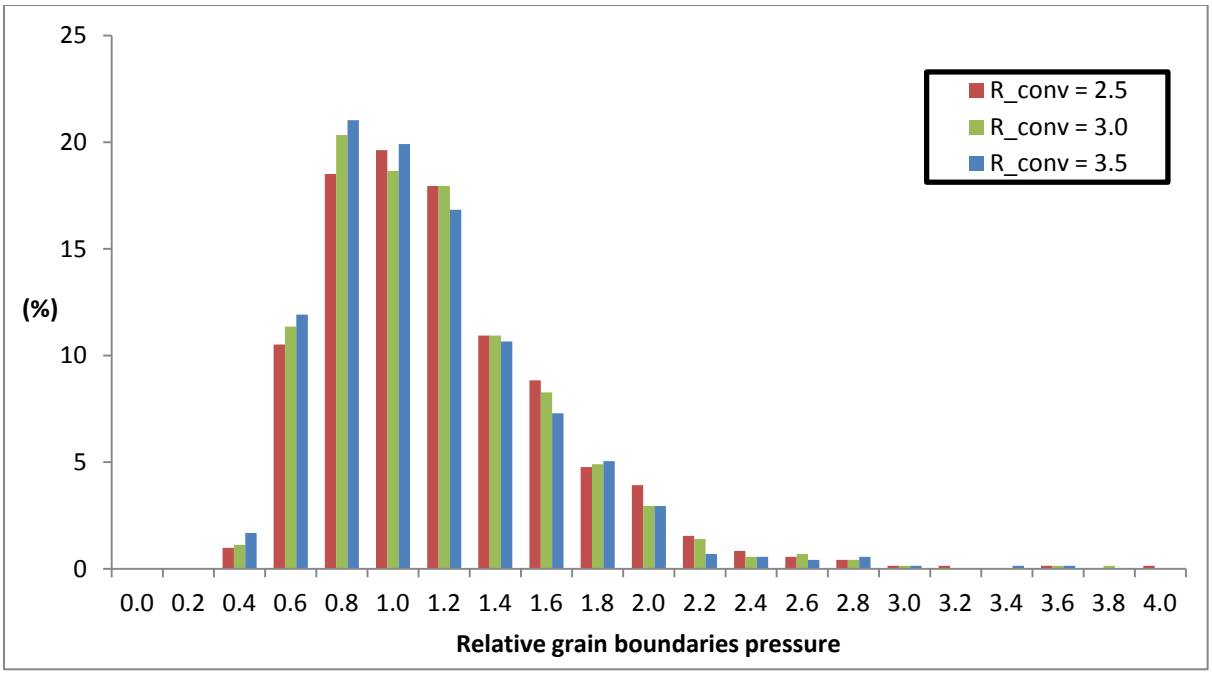

Figure 5-22 Histogram of relative grain boundary pressure of STLN4 with convolution radius 2.5 3.0 and 3.5 steps.

5.6 Conclusion

Elementary facet method was used in calculation of grain boundary equivalent radius relative energy and pressure STLN3 and STLN4. Effect of convulsion radius on mean deviation angle of facet normal vectors and surface area of was investigated. Base on half sphere boundary models, to maintain the errors of mean deviation angle and surface area in 10% the appropriate convolution radius should be in the range 2.5 to 3.5 steps for grain boundaries that contain at least 75 facets. Calculation error of grain boundary equivalent radius was studied using half sphere boundary models. Using convolution radius 2.5 steps, grain boundaries larger than 75 facets maintain the error lower than 10%. In general real grain boundaries are flatter than the half sphere boundaries and lower error can be expected. Calculation of relative grain boundary energy from 3D-EBSD data using Young's law encounters the problem that angular summation of diheral angle less that 360° since the average normal vectors, used in Young's equation, in 3D can off planar. In this study, the problem was solved by setting the threshold of the angular summation at 350°. Grain boundary equivalent radius relative energy and pressure of STLN4 were successfully calculated using elementary facet methods. However only in the region of misorientation greater than approximately 30° are reliable since energy relations in the region misorientation lower than 30° are rarely found.CSL boundaries Σ3 Σ7 Σ9 and Σ11can be identified in the plot of relative energy versus misorientation of STLN4. In STLN3 amount of triple junctions seem inadequate to the calculation.

Chapter 6. Lattice constant measurement from Electron Backscatter diffraction Pattern

6.1 Introduction

Electron backscatter diffraction (EBSD) is principally used in measurement of lattice orientation of crystalline samples. However, as described in Chapter 1, Kikuchi band width in EBSP is related to lattice plane spacing in the sample. This could allow us to measure lattice constant from the band width. One of the advantages of measuring lattice constant from EBSP over the X-ray diffraction (XRD) technique is that the measuring can be performed on individual crystals. For a sparsely populated secondary phase, XRD peaks will generally not appear clearly and measuring lattice constant of such small amount phase might be possible by EBSP. However precision of measuring of this technique needs to be studied. Dingley and David (Dingley & Wright., 2009) used information from EBSPs to determine unit cell space group and unit cell parameters of some crystalline samples. But their work focused on determination of unit cell space group rather than precision of lattice parameters calculation. In this work, we focus on the accuracy of measuring of lattice constant from EBSP and compare this to results from XRD technique by employing composite samples from doped strontioum titanate (STN94) and doped zirconia (8YSZ), which both crystallize in cubic lattices but have slightly different lattice parameters [ref] . Further, STN94 will attain slightly different lattice parameters as a function of the vacancy concentrations level, which has been varied through sintering the material in both oxidizing and reducing atmospheres.

6.2 Calculation of lattice constant from Kikuchi band width

In EBSP Kikuchi bands are formed by backscattered electrons that satisfy the Bragg equation:

$$2d_{hkl} \sin\theta = n\lambda \qquad 10\text{-}1$$

Where d_{hkl} is lattice spacing of (*hkl*) plans, θ is Bragg angle, λ is electron wavelength and *n* is order of interference (in this case *n* is 1). Figure 1 illustrates schematic of projection of backscattered electron on a phosphor screen. EBSP capturing from the phosphor screen is a

projection of a spherical pattern on a flat plane. Spherical projection on a flat screen yields distortion of Kikuchi bands. Far from the pattern centre Kikuchi band width is wider than it at the pattern centre. To obtain the real band width at the distance of detector distance (*D*) from the sample the EBSP have to be re-projected to a sphere surface of radius *D* as shown in Figure 6-1. Assuming W_{hkl} is a band width of a (*hkl*) band on a flat screen and its real band width is the arc length A_{hkl} on the projection sphere. The arc length A_{hkl} relates to the Bragg angle (in radius) as equation 6-2 (see Figure 6-1)

$$A_{hkl} = 2\theta D \qquad 10\text{-}2$$

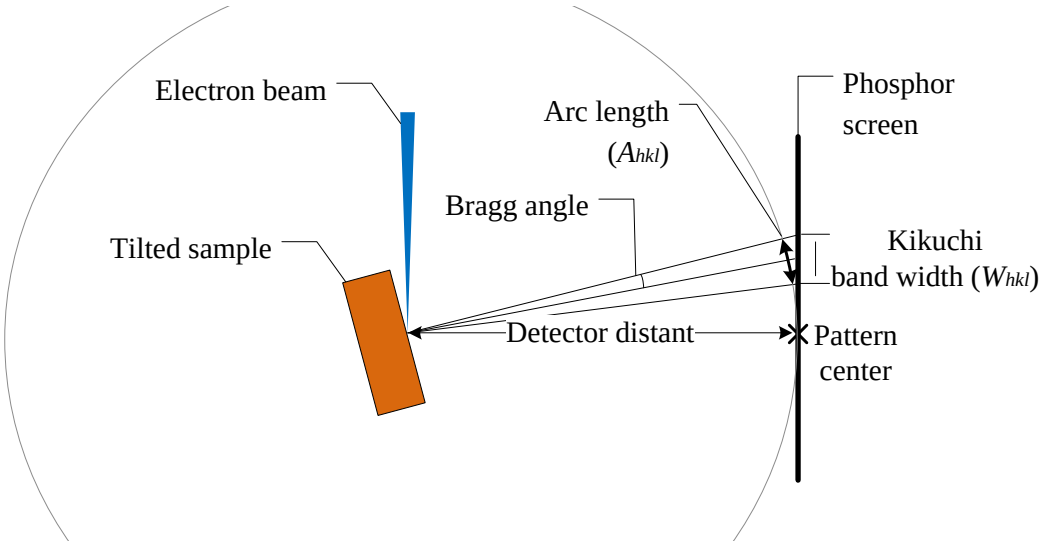

Figure 6-1 Schematic shows relationship of Kikuchi band width (W_{hkl}), Bragg angle (θ) of backscattered electrons and the arc length (A_{hkl}) which is a radial projection of the band width W_{hkl} on a sphere of radius equal detector distant, depicted by gray circle.

Since the Bragg angle in EBSD experiment is very small, the term $\sin\theta$ in equation 6-1 can be replaced by θ and equation 6-1 becomes

$$2\theta d_{hkl} = \lambda \qquad 10\text{-}3$$

Combining equations 6-2 and 6-3 to eliminate 2θ yields

$$d_{hkl} = \frac{\lambda D}{A_{hkl}} \qquad 10\text{-}4$$

The Lattice constant can be obtained from the spacing d_{hkl} if the Miller indices (*hkl*) are known. Equation 6-5 and 6-6 are the relationship of lattice constant, miller indices and inter planar spacing of cubic system and tetragonal systems.

(Cubic) $$\frac{1}{d_{hkl}^2} = \frac{h^2 + k^2 + l^2}{a^2} \qquad 10\text{-}5$$

(Tetragonal) $$\frac{1}{d_{hkl}^2} = \frac{h^2 + k^2}{a^2} + \frac{l^2}{c^2} \qquad 10\text{-}6$$

The relationship for other lattice systems can be found in (West 1996). Substitution of d_{hkl} from equation 6-4 into equation 6-5, the lattice constant of a cubic system is

$$a = \frac{\lambda D}{A_{hkl}}\sqrt{h^2 + k^2 + l^2} \qquad 10\text{-}7$$

The Electron wavelength λ is a function of SEM accelerating voltage. In practice the product λD can be treated as a calibration constant ($C = \lambda D$).

$$a = \frac{C}{A_{hkl}}\sqrt{h^2 + k^2 + l^2} \qquad 10\text{-}8$$

By using a well known lattice constant sample for calibration the constant can be measured. For tetragonal system equation 6-6 cannot be rearranged to find the lattice constants as it can be done in cubic system. Equation 6-6 can be solved by using advance fitting methods such as non-linear least square fitting.

6.3 Measuring real band width in an EBSP

First of all we need to covert EBSP image unit in pixels to the phosphor screen unit in millimetre. The EBSP resolution is 1344 x 1024 pixels and the phosphor screen size is 38 x 28

mm thus converting a distance in pixels to mm can done by multiply by 38/1344 = 0.02827 mm/pixels. Figure 6-2 shows a diagram of mapping units from the EBSP to the phosphor screen.

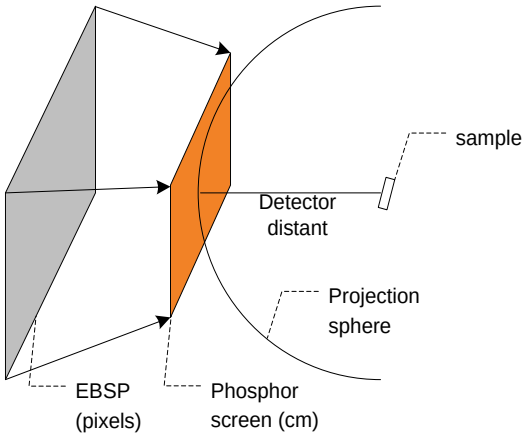

Figure 6-2 schematic shows mapping unit from EPSP to a pattern on phosphor screen.

To obtain the real band width we need to re-project the EBSP to the projection sphere then measure the width on the sphere surface. In practice we need not to project the whole EBSP sphere if we can define a capturing area that covers the portion we need. An example is given in Figure 3. Given the blue line in figure 3 is the central line of a selected band on the phosphor screen. $C1'$ and $C2'$ are the terminal points of the central line and their projection on the sphere surface are $C1$ and $C2$. The minimum arc length $C1$ - $C2$ on the sphere surface determines the length of the capturing area. The width of the capturing area can be chosen freely to cover the band. For any point p in the capturing area its intensity is the intensity of the point p', its projection on the phosphor screen.

To obtain the real band width we need to re-project the EBSP to the projection sphere then measure the width on the sphere surface. In practice we need not to project the whole EBSP sphere if we can define a capturing area that covers the portion we need. An example is given in Figure 3. Given the blue line in figure 3 is the central line of a selected band on the phosphor screen. $C1'$ and $C2'$ are the terminal points of the central line and their projection on the sphere surface are $C1$ and $C2$. The minimum arc length $C1$ - $C2$ on the sphere surface determines the

length of the capturing area. The width of the capturing area can be chosen freely to cover the band. For any point p in the capturing area its intensity is the intensity of the point p', its projection on the phosphor screen.

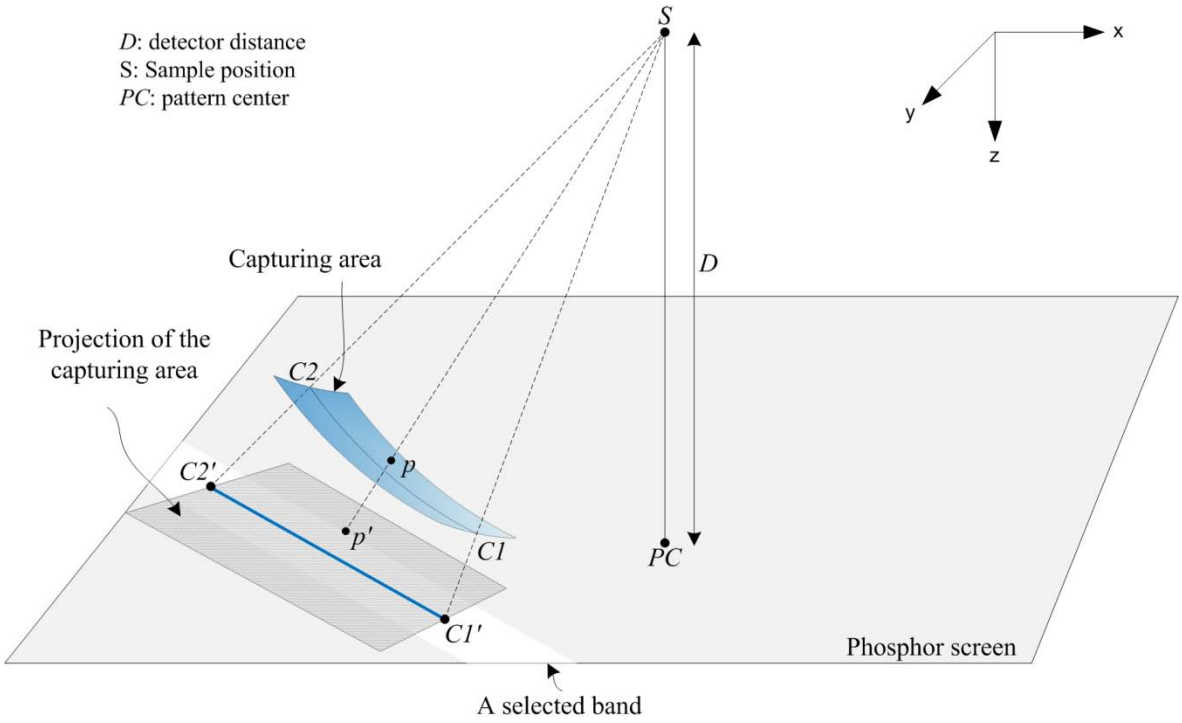

Figure 6-3 A Schematic shows a designing capturing area on the projection sphere surface (shaded blue) and it projection on the phosphor screen. The length of the capturing area is the arc length C1-C2.

Given the origin of the system is at the sample position. Data sampling in the capturing area is performed by scanning a position vector $\boldsymbol{r}$ (see Figure 6-4). The position vectors of the points $C1'$ and $C2'$ on the phosphor screen are

$$\boldsymbol{r'_1} = (C1'_x - PC_x)\hat{\boldsymbol{i}} + \left(C1'_y - PC_y\right)\hat{\boldsymbol{j}} + D\hat{\boldsymbol{k}} \qquad 10\text{-}9$$

$$\boldsymbol{r'_2} = (C2'_x - PC_x)\hat{\boldsymbol{i}} + \left(C2'_y - PC_y\right)\hat{\boldsymbol{j}} + D\hat{\boldsymbol{k}} \qquad 10\text{-}10$$

The position vectors $\boldsymbol{r_1}$ and $\boldsymbol{r_2}$ (see Figure 6-4) of the points $C1$ and $C2$ on the sphere surface (of radius *D*) can computed by resizing the vectors $\boldsymbol{r'_1}$ and $\boldsymbol{r'_2}$

$$\boldsymbol{r_1} = \frac{D}{|\boldsymbol{r'_1}|}\boldsymbol{r'_1} \quad 10\text{-}11$$

$$\boldsymbol{r_2} = \frac{D}{|\boldsymbol{r'_2}|}\boldsymbol{r'_2} \quad 10\text{-}12$$

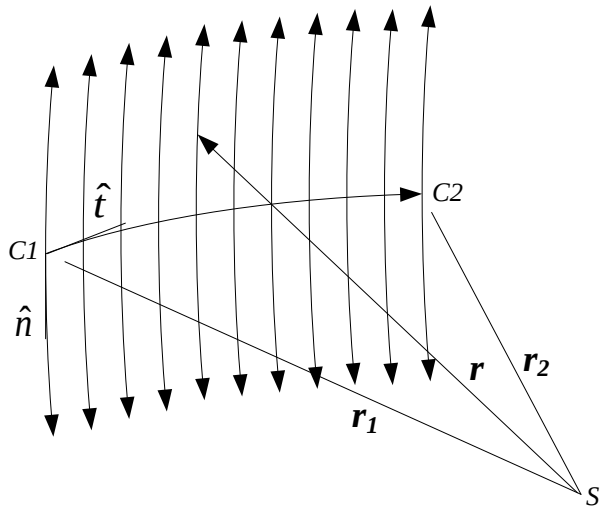

Figure 6-4 Sampling method in a capturing area on the projection sphere surface.

Given the scanning step is δ, *W* and *L* are the width and length of the sampling area, *i* and *j* are integers running in the following ranges.

$$-\frac{W}{2} \leq j\delta \leq \frac{L}{2} \quad 10\text{-}13$$

$$0 \leq i\delta \leq SL \quad 10\text{-}14$$

The *SW* we can assign to cover the selected band. The *LW* is the arc length from $C1$ and $C2$ can be calculated from dot product of vectors $\boldsymbol{r_1}$ and $\boldsymbol{r_2}$

$$LW = D.cos^{-1}(\frac{1}{|\boldsymbol{r_1}||\boldsymbol{r_2}|}\boldsymbol{r_1} \cdot \boldsymbol{r_2}) \quad 10\text{-}15$$

In Figure 6-4, $\hat{\boldsymbol{n}}$ is a unit normal vector to the plane of vectors $\boldsymbol{r_1}$ and $\boldsymbol{r_2}$ and $\hat{\boldsymbol{t}}$ is a unit tangential vector along the path from $C1$ to $C2$ on the projection sphere. At the starting point $C1$ (i = 0, j = 0) the scanning position vector $\boldsymbol{r}$ the normal vector $\hat{\boldsymbol{n}}$ and the tangential vector are $\hat{\boldsymbol{t}}$

$$\boldsymbol{r}(0,0) = \boldsymbol{r_1} \tag{10-16}$$

$$\hat{\boldsymbol{n}}(0,0) = \frac{\mathbf{1}}{|\boldsymbol{r_1}||\boldsymbol{r_2}|}(\boldsymbol{r_1} \times \boldsymbol{r_2}) \tag{10-17}$$

$$\hat{\boldsymbol{t}}(0,0) = \frac{\mathbf{1}}{|\boldsymbol{r_1}|}(\hat{\boldsymbol{n}}(0,0) \times \boldsymbol{r_1}) \tag{10-18}$$

Scanning of the position vector can run in three directions, i.e. positive $\hat{\boldsymbol{n}}$, negative $\hat{\boldsymbol{n}}$ and positive $\hat{\boldsymbol{t}}$. The scanning path will form a structure like a fish bone as in Figure 6-4. When the vector $\boldsymbol{r}(i,j)$ shifts to the positive $\hat{\boldsymbol{n}}$ direction (+j) the unit vector $\hat{\boldsymbol{n}}$ will change direction as well.

$$\boldsymbol{r}(i,j+1) = \boldsymbol{r}(i,j) + \delta\hat{\boldsymbol{n}}(i,j) \tag{10-19}$$

$$\hat{\boldsymbol{n}}(i,j+1) = \frac{1}{|\boldsymbol{r}(i,j+1)|}[\boldsymbol{r}(i,j+1) \times \hat{\boldsymbol{t}}(i,0)] \tag{10-20}$$

When the vector $\boldsymbol{r}(i,j)$ shifts to the negative $\hat{\boldsymbol{n}}$ (-j) the unit vector $\hat{\boldsymbol{n}}$ will change direction as well.

$$\boldsymbol{r}(i,j-1) = \boldsymbol{r}(i,j) - \delta\hat{\boldsymbol{n}}(i,j) \tag{10-21}$$

$$\hat{\boldsymbol{n}}(i,j-1) = -\frac{1}{|\boldsymbol{r}(i,j-1)|}[\boldsymbol{r}(i,j-1) \times \hat{\boldsymbol{t}}(i,0)] \tag{10-22}$$

When the vector $\boldsymbol{r}(i,j)$ shifts to the positive $\hat{\boldsymbol{t}}$ (+i) along the arc $C1-C2$ the unit vector $\hat{\boldsymbol{t}}$ will change direction as well.

$$\boldsymbol{r}(i+1,0) = \boldsymbol{r}(i,0) + \delta\hat{\boldsymbol{t}}(i,0) \tag{10-23}$$

$$\hat{\boldsymbol{t}}(i+1,0) = \frac{1}{|\boldsymbol{r}(i+1,0)|}[\hat{\boldsymbol{n}}(i,0) \times \boldsymbol{r}(i+1,0)] \tag{10-24}$$

By scanning the vector $\boldsymbol{r}(i,j)$ we can calculate it at any point $p(i,j)$ in the capturing area and its can be written in rectangular coordinate system as

$$\boldsymbol{r}(i,j) = X_{ij}\hat{\boldsymbol{\imath}} + Y_{ij}\hat{\boldsymbol{\jmath}} + Z_{ij}\hat{\boldsymbol{k}} \qquad 10\text{-}25$$

By extending the position vector $\boldsymbol{r}(i,j)$ from the sphere surface into the phosphor screen we can obtain the position vector point of the point p' (projection of the point $p(i,j)$)

$$\boldsymbol{r}'(i,j) = \frac{D}{Z_{ij}}(X_{ij}\hat{\boldsymbol{\imath}} + Y_{ij}\hat{\boldsymbol{\jmath}} + Z_{ij}\hat{\boldsymbol{k}}) \qquad 10\text{-}26$$

Thus coordinate of the point p' on the phosphor screen relative to the pattern center is

$$p' = (\frac{D}{Z_{ij}}X_{ij}, \qquad \frac{D}{Z_{ij}}Y_{ij}) \qquad 10\text{-}27$$

Therefore by scanning the position vector $\boldsymbol{r}(i,j)$ along the fish bone structure we can read the pixel intensity of the corresponding point p' on the phosphor screen to store in the capturing pixels on the projection sphere.

6.4 Experiment

6.4.1 Samples

Four samples used in this experiment are $Sr_{0.94}Ti_{1.0}Nb_{0.1}O_3$ (STN94) sintered at 1450 °C in air, 8% mol yttria-stabilised zirconia (8YSZ), dense binary mixture of STN94 and 8YSZ (50:50) sintered in noxal[2] (STN94-8YSZ 50% noxal) and a dense binary mixture of STN94 and 8YSZ (90:10) sintered in air (STN94-8YSZ 10% air)[3]. Silicon single crystal is used for calculation of calibration constant. The YSZ sample was carbon coated with an approximate thickness of 10-18 nm to improve it charge removing in SEM analysis.

[2] *Noxal is labeling a gas mixture from 9 vol% hydrogen and 91 vol% Argon*
[3] *The aim was to investigate STN94-8YSZ 50% in air to compare with STN94-8YSZ 50% in noxal but unfortunately a wrong sample (STN94-8YSZ 10% in air) was picked up. However, after running the EBSD-analysis the limitations of the technique made further runs obsolete.*

6.4.2 EBSPs acquisition

EBSD work was performed on a CrossBeam 1540XB™ (Zeiss, Oberkochen Germany) equipped with a Nordlys S™ EBSD detector (Oxford Instruments, Hobro Denmark). Flamenco of Channel 5 software suit (Oxford Instruments, London UK) was used for collection of EBSPs and indexing. To obtain the most precise lattice constant measurement Kikuchi bands in EBSP need to be as wide and exhibit as sharp contrast (high band slope) as possible. Kikuchi bandwidth can be increased by increasing EBSD detector distance and reducing SEM accelerating voltage. However increasing detector distant reduces field of view of the detector and yields more difficulty of EBSP indexing. For first time setup, the detector was repeatedly retracted with a small distance, around 2.0 mm, and indexing parameters refined until reaching an optimum distance. The refined indexing parameters of the final position were saved for later use. Decreasing SEM kV can reduce both band contrast and band slope of EBSP. However both band contrast and band slope can be improved by low kV FIB polishing (see section 3.2.2).

In this experiment sample surfaces were milled with a 30kV, 2 nA focused ion beam approximately 1 µm depth to remove residual stress and damage from mechanical polishing. The surfaces were then polished with the FIB 5kV 2.5 nA to remove possible amorphous layer from the high kV FIB milling. EBSD detector was retracted from normal used position 177.8 mm to 160.0 mm increases the detector distance from 17.727 mm to 35.527 mm. SEM accelerating voltage used for collecting EBSPs was 10 kV at an SEM working distance of 15 mm. The EBSD acquisition parameters were as follow:

- Pixel Binning 1x1
- Gain Amplification low
- Frame Averaging 20
- Integration Time was adjusted to obtain the best signal intensity. In this experiment the integration time is in the order of 300 -1000 ms

Summary of EBSPs data collection is list in table 1. Each pattern collected from different grain. A 10 kV EBSP and a 30 kV EBSP of the single crystal silicon was collected for calculating the calibration constant. The 30 kV EBSPs will be used for indexing purpose because they give a better band detection than in 10 kV EBSP samples. Totally 62 EBSPs were collected

as shown in Table 6-1.

Table 6-1 EBSPs collected for lattice constant measurement.

Sample	Phase	Number of patterns	
		SEM 10 kV	SEM 30 kV
STN94-8YSZ 50% (noxal)	STN	5	5
	YSZ	5	5
STN94-8YSZ 10% (air)	STN	5	5
	YSZ	5	5
SYN94	STN	5	5
8YSZ	YSZ	5	5
Silicon	Si	1	1

6.4.3 Lattice constant calculation

According to Equation 8 the real band width (arc length A_{hkl}) and miller indices (*hkl*) are needed for calculation of the lattice constant. In each EBSP, the five strongest bands were selected for the measuring. The Miller indices of each band can obtained by indexing the 30 kV EBSPs and compare the resulted zone to a simulated EBSP. The real band width (arc length A_{hkl}) were measured from bands in the 10 kV EBSPs. The detail in each step was described as the following.

1) Indexing EBSPs

In this step each EBSP was carefully indexed using the Flamenco software. The resulting zone axes of each EBSP will be used in next step, determining of Miller indices. 30kV EBSPs were used for indexing. The match units for STN YSZ and Si phases were created using the Twist program of Channel 5 software suite based on crystallographic information in Table 1 of Chapter 1: $SrTi_{0.875}Nb_{0.125}O_3$ (*Cubic*) for STN and $Zr_{0.84}Y_{0.16}O_{1.92}$ (*Cubic*) for YSZ. Space group of Si used is SG = 227 (Fd-3m) and its standard lattice constant (a) is $a = 5.43053$ Å (Toebbens *et al*., 2001). Band detection for the indexing was manually assigned to 8-10 bands. The indexed

EBSPs were then stored for further use. Figure 6-5 (a) shows an example of indexed pattern and the selected five bands in the pattern and (b) is the corresponding 30 kV that will be used to measure band width.

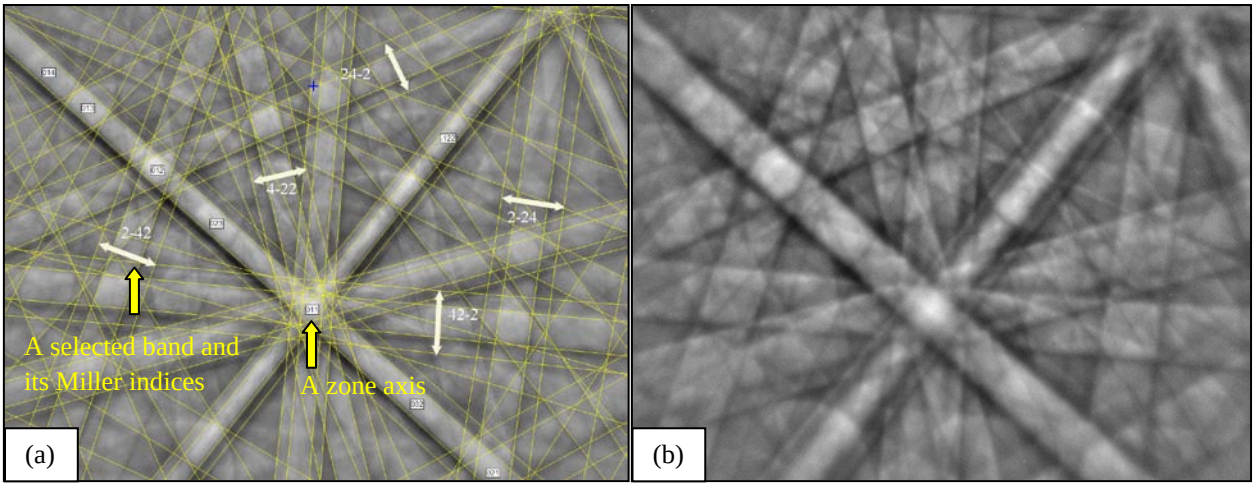

Figure 6-5 (a) an example of indexed EBSP (SEM 30 kV) of STN in STN-YSZ(Air) with selected five bands and their Miller indices. (b) The pattern collected at the same location of (a) but collected at SEM 10 kV used for measuring band width.

2) Determination of Miller indices (*hkl*).

In this step Miller indices of the select bands in each pattern were determined using the zone axis and a simulated spherical Kikuchi pattern of each phase as shown in Figure 6-6. The spherical Kikuchi pattern was rotated to the orientation that matches the zone axes appeared in the indexed EBSP. Then the Miller indices of the selected band can be identified by compare to the spherical pattern. The simulated Kikuchi sphere used in this experiment was generated by using HKL Fast acquisition software (Oxford Instruments, London UK) combine with the created match units.

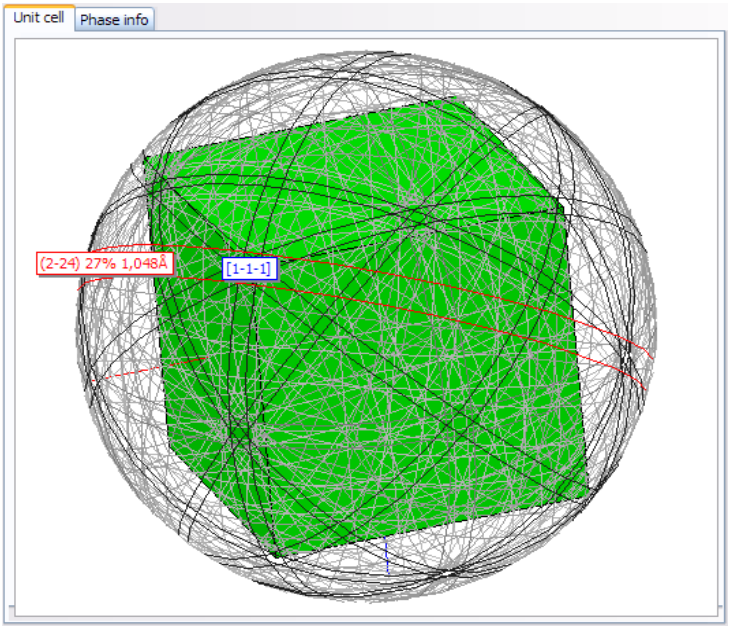

Figure 6-6 A simulated spherical Kikuchi pattern of $SrTiO_3$ captured from the HKL Fast acquisition used to determine Miller indices. The blue numbers [-1-1-1] is a zone axis and the red numbers, (2-24), is the miller indices of the selected red band.

3) Measuring band width

The arc lengths (A_{hkl}) of Kikuchi bands in 10 kV EBSPs were measured using an in-house developed program using Microsoft Visual C++ 2008 Express edition. Screen capture of the program is shown in Figure 6-4. A10 kV EBSP is loaded into the program, Figure 6-7 area (a), and a central line (blue line) of a selected band is drawn to specify the direction to capture the band. The distance *C1- C2* defines the length of the capture area and the width is given by pixels number in the box (d) in Figure 7. The EBSP is then radially back-projected on to surface of the sphere of radius *D* and the band is captured on the spherical surface as described in section 4.3. The resulting captured band is shown in area (b) of Figure 6-7. Then an average cross section intensity of the captured band is calculated by row averaging as illustrated in Figure 6-8. Subsequently, the slope, the blue line in Figure 6-7, of the intensity profile is calculated. The real width or the arc length (A_{hkl}) of the band is defined as the distance between negative and positive peaks in the slope. The unit of the arc length used in this work is in pixels.

If the drawing central line is not parallel to the band, the captured band will be off horizontally. The average cross section intensity will broaden. The peaks in slope graph will become blurred, however their position will not change. Therefore, even we cannot draw a strictly parallel central line to the band we can still measure the correct band width since the peak positions can be identified.

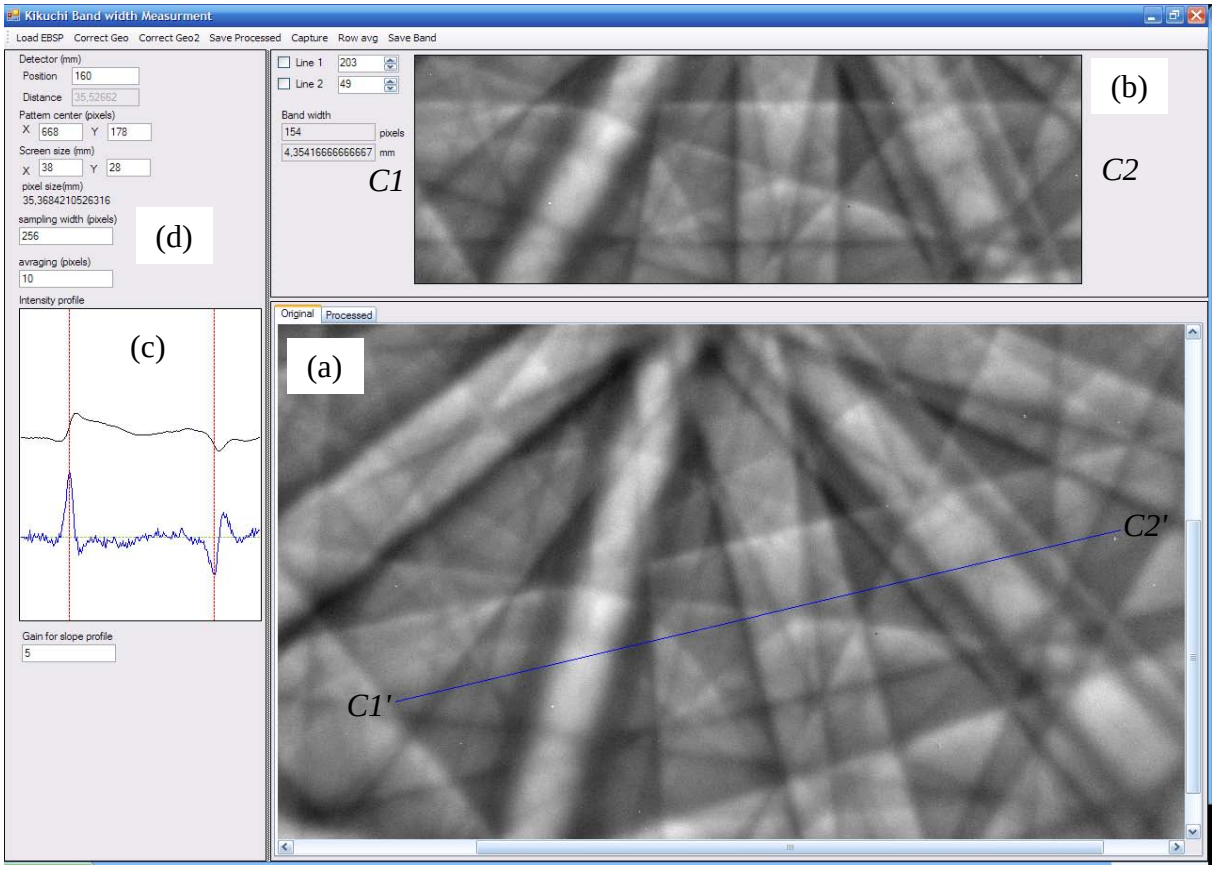

Figure 6-7 Determination of the arc length A_{hkl} using the developed program, (a) assigning band centre of the selected band (b) the band projected on the sphere of radius *D* is capture (c) average cross section intensity of the captured band in red and its slope in blue.

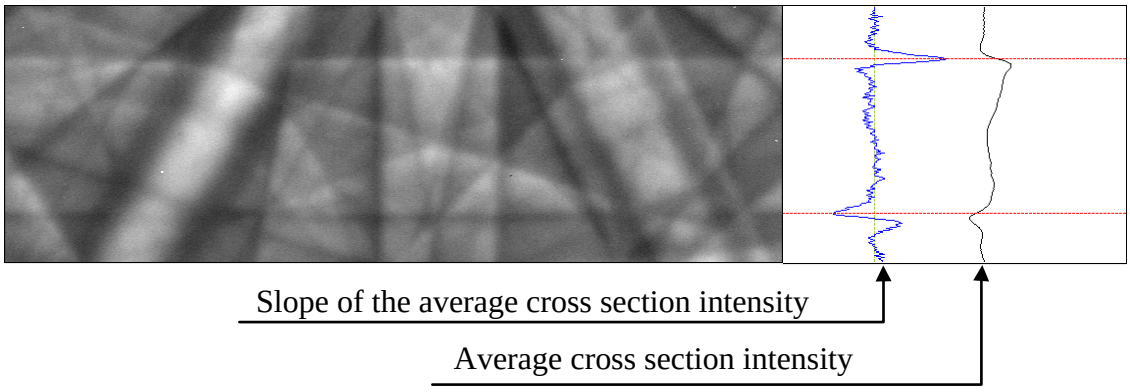

Figure 6-8 Row averaging of a capture band yields its average cross section intensity. Slope of the cross section intensity was used in determination of the real band width A_{hkl}.

4) Calculation of lattice constant

Five band widths of the Si were used to compute the calibration constant $C = \lambda D$ using the following equation.

$$C = \lambda D = \frac{aA_{hkl}}{\sqrt{h^2 + k^2 + l^2}} \qquad 10\text{-}28$$

$a = 5.43053$ Å is lattice constant of Si. Lattice constant of STN and YSZ in each sample can be computed from equation 8. Unit of the band widths in this calculation is pixels. The resulting lattice constants were compared to the resulting from XRD analysis.

6.5 Result and discussion

6.5.1 Collection of EBSPs

Figures 6-9 to 6-13 show SEM images of the milled and polished surface on the four samples and Si calibration sample and their sample EBSPs acquired at SEM 10 kV and 30 kV. The Figure 6-9, 6-11 and 6-12 also show positions of collecting EBSPs in each sample.

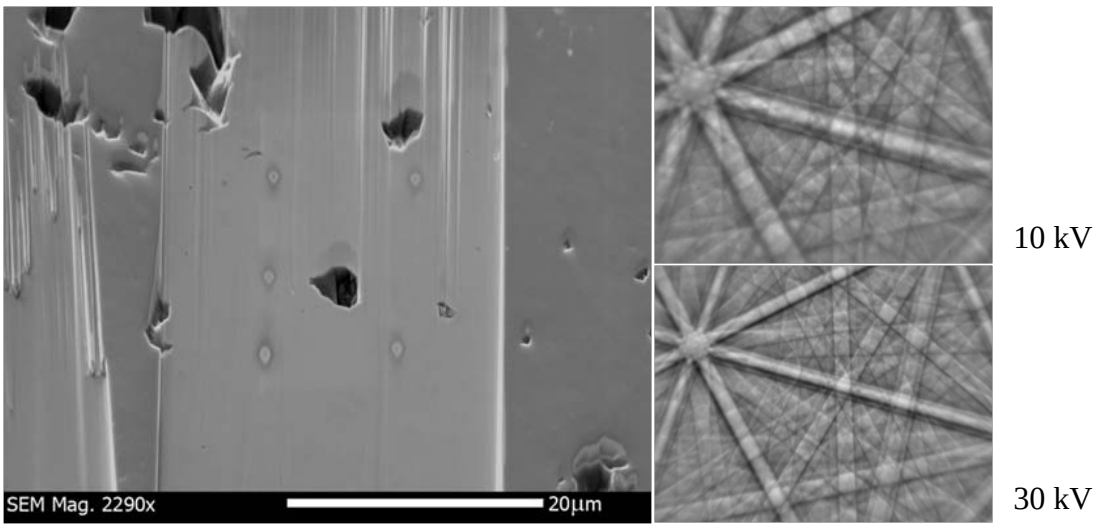

Figure 6-9 Five electron contamination marks in the SEM image reveal the collecting positions of EBSPs of STN in STN94 sample and an example 10kV EBSP and 30kV EBSP.

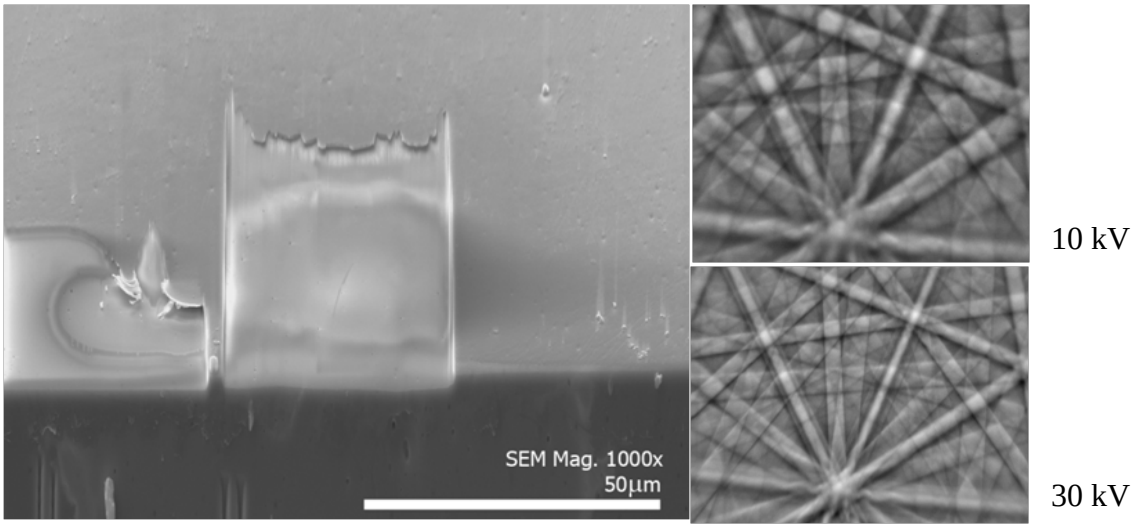

Figure 6-10 The five dots in the picture are collecting positions of EBSPs of YSZ in 8YSZ sample and its example 10kV EBSP and 30kV EBSP.

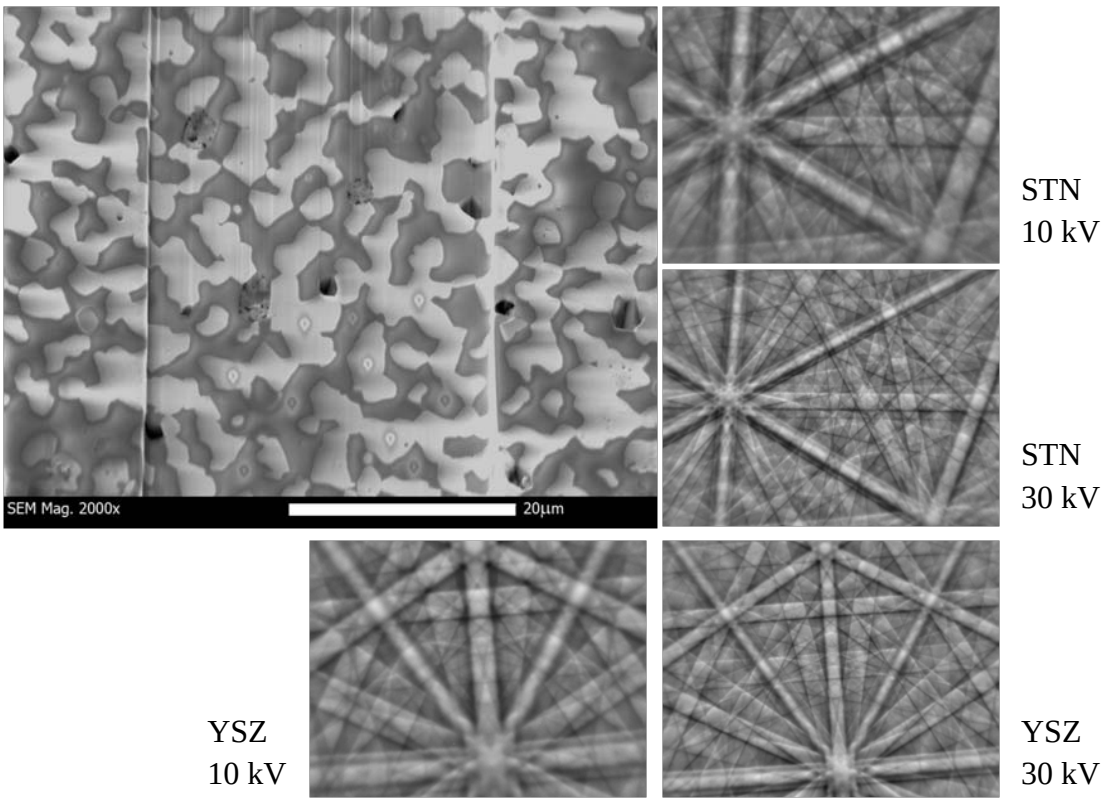

Figure 6-11 The five dots in the bright phase are collecting positions of EBSPs of YSZ in STN94-8YSZ 50% (noxal) sample and the five dots in the dark phase are the collecting position of EBSPs of STN in the sample and its example 10kV EBSP and 30kV EBSP.

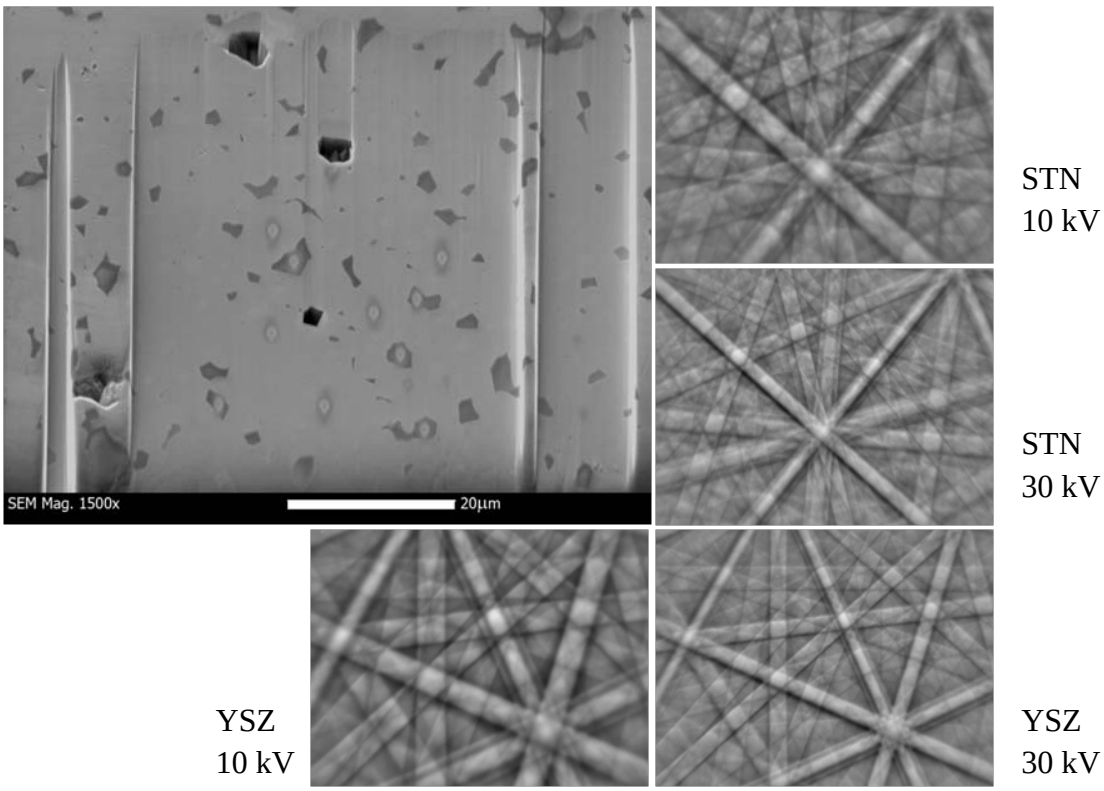

Figure 6-12 The five dots in the bright phase are collecting positions of EBSPs of YSZ in STN94-8YSZ 10% (air) sample and the five dots in the dark phase are the collecting position of EBSPs of STN in the sample and its example 10kV EBSP and 30kV EBSP.

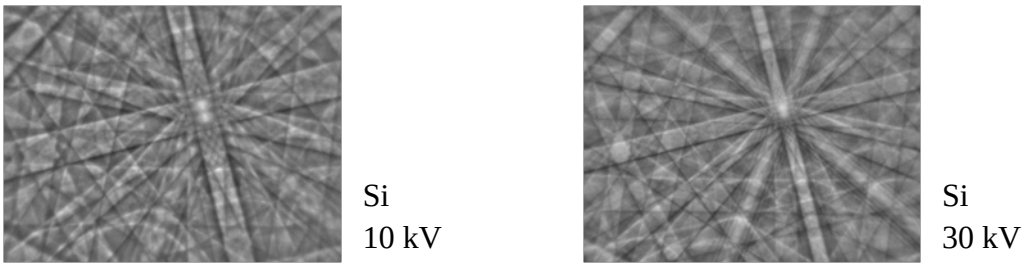

Figure 6-13 The EBSP collected from Si sample at SEM 10 kV and 30 kV.

6.5.2 Lattice constant measuring from XRD

Figure 6-14 and 6-15 are the XRD peaks of the STN94-8YSZ 50% (noxal) and STN94-8YSZ 10% (air) respectively. In STN94-8YSZ 50% (noxal) the XRD result indicated that both STN and YSZ phase lattice are cubic. While in STN94-8YSZ 90:10 (air) STN lattice is cubic but YSZ lattice is tetragonal. Measuring lattice constant from the XRD peaks was performed by using STOE WinXPow 2.20. Lattice constant of the cubic STN and YSZ in STN94-8YSZ 50% (noxal) are 3.9324 Å and 5.1224 Å respectively. In the STN94-8YSZ 90:10 (air) lattice constant of STN is 3.9163 Å. Since our calculation of lattice constant is limited to cubic systems for the time being, we neglected to investigate lattice constant of YSZ in STN94-8YSZ 90:10 (air).

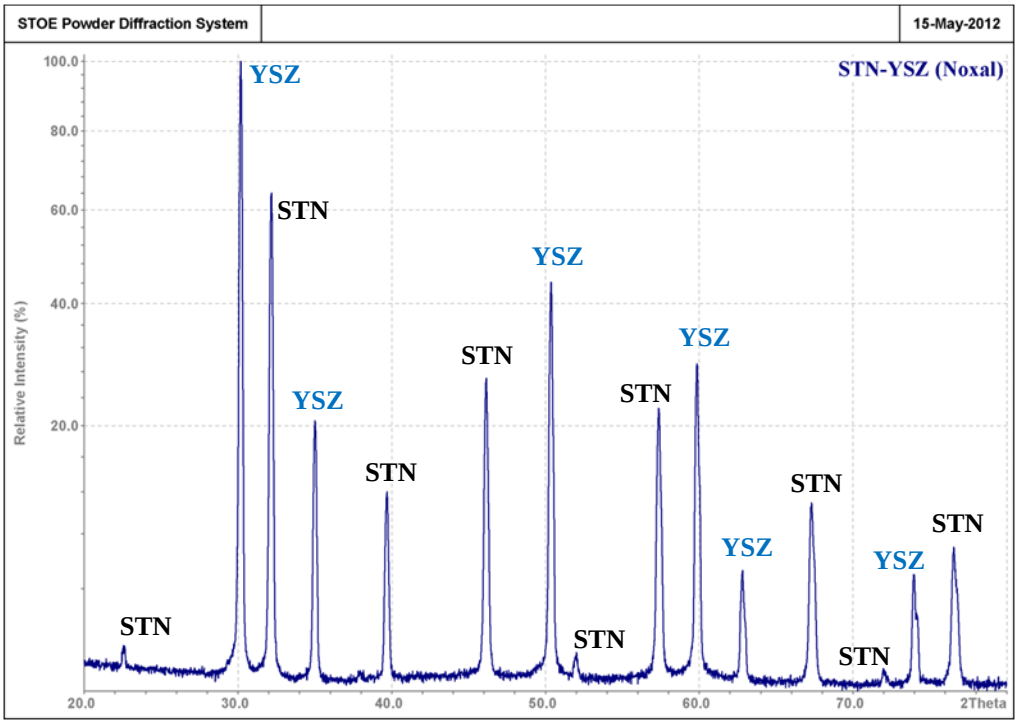

Figure 6-14 2θ plot of XRD peaks of STN94-8YSZ 50% (noxal) both STN and YSZ phases are cubic.

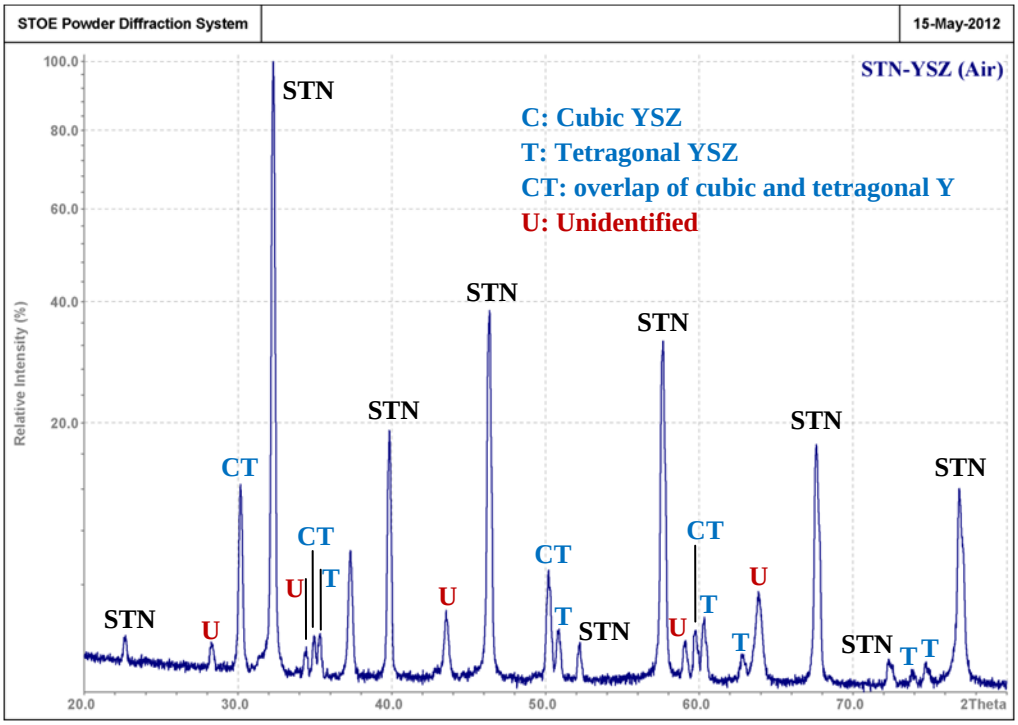

Figure 6-15 2θ plot of XRD peeks of STN94-8YSZ 10% (air). STN phase is cubic while YSZ phase is tetragonal.

6.5.3 Calculation of lattice constant from EBSP

The band widths measured using the developed program and their indices of STN and YSZ in the four samples and Si single crystal are listed in Table 6-2. Five band widths of Si single crystal in the last row of Table 6-2 were used in calculation the calibration constant using equation 6-28. The calculated results are shown in Table 6-3 and its average over the five bands is 164.0 $pixels$. Å. This constant was then used in calculation lattice constant of STN and YSZ in the four samples. STN and YSZ lattice constants of the four samples were calculated using the band widths in Table 6-2 and are listed in Table 6-4. Lattice constant from XRD results were also provided in Table 6-4 for comparison. Since the XRD graph of STN94-8YSZ 10% (air) indicates that YSZ phase in the sample is not all cubic its lattice constant cannot be derived through equation 6-8. Tetragonal or more complicated system always has two or more unknown lattice constants, thus an advanced method of data fitting is needed to solve the lattice constant. The calculated lattice constant of each phase in Table 6-4 was averaged over 25 bands (5 bands

in each 5 EBSP) and their standard deviations (SD) are in the range 0.03-0.04 Å. Using the lattice constants from XRD results as reference the standard deviation corresponds to error of 0.6 - 0.9 % (SD x 100/ lattice constant). Regardless of the SD values, the average lattice constant of STN in STN94 gives the best match to the XRD result with the error at 0.01% while the average lattice constant of YSZ in STN94-8YSZ 50% (noxal) is the worst match with the error at 0.67% error.

Table 6-2 Kikuchi band width measured from EBSPs of the four samples and of Si single crystal.

sample	Phase	EBSP	Band width in pixels and miller indices (*hkl*)				
			Band#1	Band#2	Band#3	Band#4	Band#5
STN94	STN	#1	207 (242)	204 (4-22)	188 (042)	185 (402)	185 (4-20)
		#2	206 (2-42)	206 (2-4-2)	207 (2-24)	186 (024)	188 (2-40)
		#3	204 (2-42)	206 (2-4-2)	207 (2-24)	189 (024)	187 (204)
		#4	204 (2-4-2)	207 (2-24)	203 (2-42)	185 (204)	203 (4-22)
		#5	203 (2-42)	207 (2-24)	186 (024)	184 (204)	145 (2-2-2)
YSZ	YSZ	#1	165 (11-5)	156 (4-22)	157 (4-2-2)	157 (2-24)	138 (3-1-3)
		#2	156 (2-24)	154 (42-2)	139 (3-13)	157 (22-4)	137 (31-3)
		#3	139 (133)	164 (1-1-5)	156 (42-2)	156 (242)	155 (2-2-4)
		#4	155 (4-2-2)	156 (2-42)	154 (42-2)	166 (5-1-1)	155 (24-2)
		#5	155 (24-2)	155 (242)	137 (133)	155 (224)	154 (42-2)
STN94-8YSZ 51% (noxal)	STN	#1	206 (242)	188 (20-4)	203 (22-4)	188 (240)	187 (024)
		#2	205 (2-42)	205 (2-4-2)	189 (2-40)	185 (024)	205 (224)
		#3	206 (4-2-2)	183 (40-2)	185 (042)	189 (402)	130 (3-10)
		#4	188 (204)	207 (2-4-2)	188 (024)	187 (2-40)	147 (2-2-2)
		#5	205 (242)	206 (22-4)	185 (20-4)	187 (024)	187 (042)
	YSZ	#1	156 (224)	165 (1-5-1)	156 (4-22)	139 (3-13)	139 (313)
		#2	156 (422)	156 (42-2)	154 (224)	137 (313)	138 (31-3)
		#3	164 (115)	156 (2-24)	155 (2-2-4)	155 (4-2-2)	139 (3-13)
		#4	156 (24-2)	165 (1-15)	156 (22-4)	156 (422)	152 (42-2)
		#5	155 (2-42)	164 (5-1-1)	154 (22-4)	155 (2-24)	156 (42-2)
STN94-8YSZ 10% (air)	STN	#1	205 (24-2)	204 (2-42)	204 (4-22)	203 (42-2)	199 (2-24)
		#2	205 (24-2)	205 (22-4)	186 (024)	206 (242)	185 (042)
		#3	207 (24-2)	204 (2-42)	206 (4-22)	188 (04-2)	187 (402)
		#4	204 (4-2-2)	166 (400)	187 (40-2)	206 (42-2)	185 (204)
		#5	206 (4-22)	207 (2-24)	189 (40-2)	184 (402)	186 (02-4)
	YSZ	#1	156 (2-4-2)	154 (422)	157 (242)	139 (331)	138 (3-3-1)
		#2	156 (2-4-2)	156 (2-2-4)	154 (22-4)	139 (1-3-3)	137 (13-3)
		#3	156 (224)	156 (422)	156 (42-2)	155 (2-2-4)	138 (331)
		#4	155 (42-2)	156 (242)	155 (2-2-4)	139 (1-3-3)	137 (133)
		#5	156 (2-42)	154 (4-22)	155 (422)	164 (15-1)	154 (2-24)
Si	Si	#1	150 (2-2-4)	149 (2-42)	148 (2-4-2)	190 (026)	188 (206)

Table 6-3 Silicon calibration constant

Bands (*hkl*)	(224)	(2-42)	(2-4-2)	(026)	(026)	average
Band width (pixels)	150	149	148	190	188	
Calibration constant ($pixels.$Å)	166.2	165.1	164.1	163.2	161.4	164.0

Table 6-4 Average lattice constants of YSZ and STN phases in STN94-8YSZ 10% (air) STN94-8YSZ 50% (noxal), STN94 and 8YSZ computed from EBSPs compare to XRD results.

Samples	Phases	Lattice constant measured from	
		EBSPs Average ± SD	XRD
STN94-8YSZ 10% (Air)	STN	a = 3.93 ± 0.04 Å	a = 3.9163 Å
	YSZ	No calculation	undetermined
STN94-8YSZ 50% (noxal)	STN	a = 3.94 ± 0.04 Å	a = 3.9324 Å
	YSZ	a = 5.18 ± 0.03 Å	a = 5.1224 Å
STN94	STN	a = 3.92 ± 0.03 Å	a = 3.9237 Å (Page *et al.*, 2008)
8YSZ	YSZ	a = 5.17 ± 0.03 Å	a = 5.14086 Å (YASHIMA *et al.*, 1994)*

Neutron diffraction*

6.5.4 Measuring precision

Even though the average lattice constant of STN in STN94 through EBSD differs only little to the XRD results, the standard deviation shows that the measuring error of this method using data acquired by this instrument is expected to be in the range 0.6 - 0.9%. Band size also affects the measuring precision. Since EBSP image is discrete the same number of pixel error of a smaller band will give a high error on calculated lattice constant than that of a bigger band according to equation 6-7 or 6-8. Figure 6-16 shows a simulated graph of error size of one pixel of different band width of cubic Si system. The simulation used equation 6-8 and the silicon

calibration constant $164.0\ pixels.$Å (Table 6-4) by changing the band width from A_{hkl} pixels to $A_{hkl} + 1$ pixels and calculated the different of the resulting lattice constants as the error size of one pixel. The bands used in the simulation and its width are listed in Table 6-5.

Table 6-5 Bands used in the simulation of error size of one pixel. The band widths were calculated by reversing equation 8 using the constant $C = 164.0\ pixels.$Å, $a = 5.43053$ Å and Miller indices as in the table.

bands(*hkl*)	(100)	(200)	(300)	(400)	(500)	(600)	(700)	(800)	(900)
A_{hkl} (pixels)	30	60	91	121	151	181	211	242	272

Since the calibration constant used in this simulation is the real value obtained from Si calibration of our acquisition system the graph in Figure 6-16 indicates the precision limit of our instrument. In the graph, error size of one pixel decreases as the band width increases. In practice it is almost impossible to observe a high miller indices band such as (700), (800) and (900) in EBSP. The widest bands we can observe in this experiment are in the order of 130 – 200 pixels which yield the error size of one pixel approximately 0.025 - 0.04 Å. This range agrees with the range of measuring standard deviations, 0.03-0.04 Å, which resulted from deviation of 1-2 pixels around its mean value of band width.

In principle, there are two possible methods to increase Kikuchi band width. The first method is to magnify the projected bands on phosphor screen by reducing SEM kV and increasing the detector distant. This method will be limited by signal strength and the size of region of interest. The second method is to increase resolution of CCD sensor. For a same size Kikuchi band on phosphor screen doubling the CCD censor resolution yield double size of the band in EBSP image.

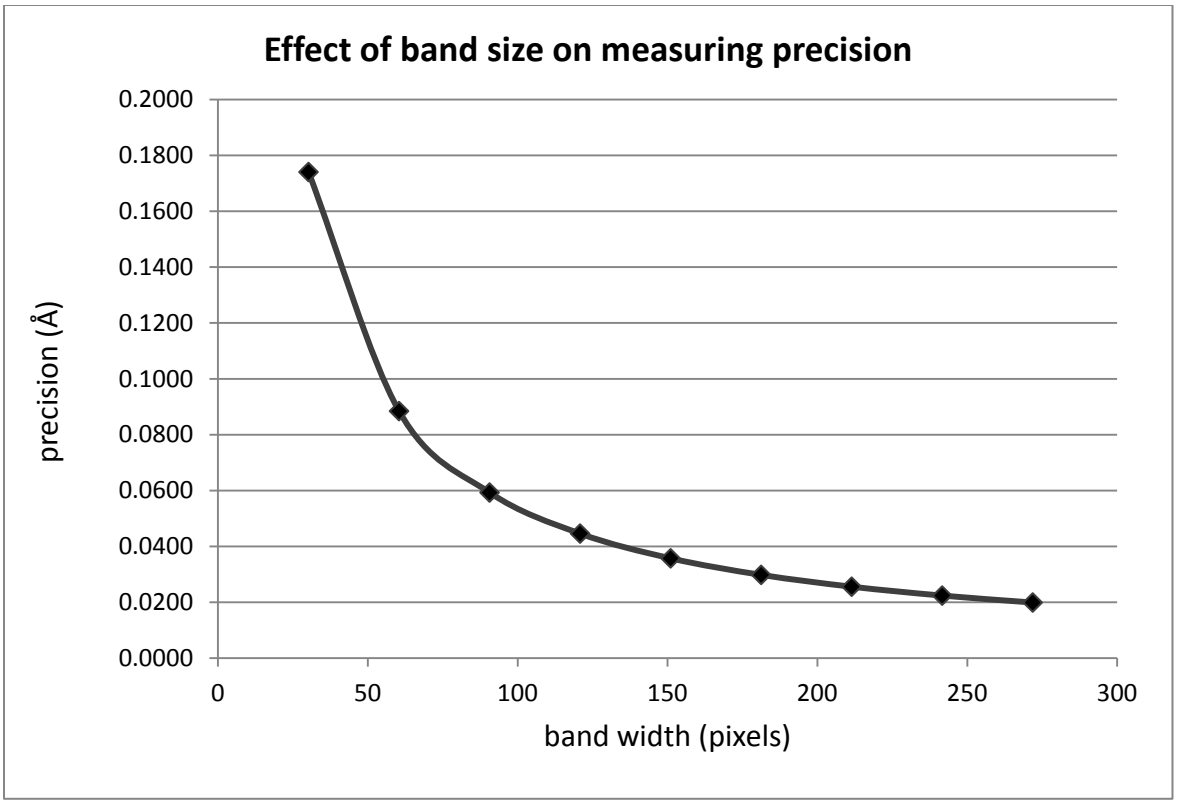

Figure 6-16 Simulation illustrates error size of one pixel of cubic Si system at SEM 10 kV detector distant 34.827 mm and pixel size 38/1344 = 0.02827 mm (on phosphor screen).

6.6 Conclusion

Lattice constants of cubic STN and cubic YSZ in STN94 STN94-8YSZ 50% (noxal) and STN94-8YSZ 10% (air) were successfully measured from SEM 10 kV EBSP. EBSP of size 1344x1024 pixels was map into plane of phosphor screen size 38 x 28 mm for measuring Kikuchi band widths. The measuring was performed on the projection sphere of a radius equal to the detector distance and centered at sample position by re-projection of the pattern on phosphor screen onto the spherical surface. Sampling step on the spherical surface is equal to pixel size on the phosphor screen, i.e. 38/1344 = 0.02827 mm. Average lattice constants measured by this method deviate approximately 0.01 - 0.67% from the lattice constant measured by XRD results. However their standard deviations are in the range 0.6 - 0.9% of the lattice constant from XRD results.

Chapter 7. Thesis outlook

The main objective of this work has been to develop methods for 3D-EBSD data acquisition and analysis as well as the ability of the technique to discriminate between two or more phases in a composite material through lattice constant measurements using EBSD, here exemplified by cubic forms of doped strontium titanate (STN) and stabilized zirconia (YSZ). The work can be divided into two main parts: data acquisition and data analysis.

Data acquisition

In 2D and 3D-EBSD data acquisition of STN and YSZ there are two serious issues to be considered: charging in low conductive ceramics and FIB milling damage. Pseudosymmetry is another subject that can be encountered when work with complicate lattice materials. The charging problem can be solved by applying a thin conductive coating. This method can be applied to both 2D and 3D-EBSD data collection. High accelerating voltage FIB milling (30 kV) can induce a significant reduction of EBSD signal in STN but less effect is seen on YSZ. Reducing the milling current trivially improve the signal quality. Low KV FIB polishing is a good alternative to improve the signal quality. In 3D-EBSD data collection FIB milling in combination with low kV-polishing has been proved to optimize the acquisition time and data quality. Two methods to further improve the FIB polishing are proposed.

Data analysis

Lattice constants of cubic STN and cubic YSZ in two dense binary mixture of STN and YSZ were successfully measured from SEM 10 kV EBSP. Precision of the measurement is limited by CCD camera resolution. Although the precision cannot be compared to standard methods such as x-ray diffraction, the advantage of this method is still that it enables the investigator to perform a sort of point analysis on well defined crystals and phases. For more complicated lattice structures than cubic and tetragonal and for very fine-grained structures, the method needs future development.

In 3D-EBSD grain growth analysis, elementary facet method is a new approach that utilizes less computer resource than e.g. finite elements method. The methods to calculate grain boundary equivalent radius, relative grain boundary energy and relative grain pressure have been

developed to a point where in the 3D-EBSD data may be applied to an essentially two-dimensional classical model. The consequences of this simplification have been evaluated. In order to develop this three-parameter model, which is equivalent to the calculation from 2D-EBSD, application of the full five-parameter model will be an interesting task for future development.

References

[Anonymous]. (2013) Kaczmarz method.

Abramov Y., Tsirelson V., Zavodnik V., Ivanov S. & Brown I. (1995) The chemical bond and atomic displacements in SrTiO3 from x-ray diffraction analysis. Acta Crystallographica Section B-Structural Science 51, 942-951.

Abrantes J.C.C., Feighery A., Ferreira A.A.L., Labrincha J.A. & Frade J.R. (2002) Impedance spectroscopy study of niobium-doped strontium titanate ceramics. J Am Ceram Soc 85, 2745-2752.

Abrantes J.C.C., Labrincha J.A. & Frade J.R. (1997) Combined effects of A-site deficiency and dopant content on the transport properties of Nb-doped strontium titanate. Ionics 3, 16-22.

Abrantes J., Labrincha J. & Frade J. (2000) Applicability of the brick layer model to describe the grain boundary properties of strontium titanate ceramics RID B-1788-2008 RID B-3984-2010. Journal of the European Ceramic Society 20, 1603-1609.

Adams B., Kinderlehrer D., Mullins W., Rollett A. & Ta'asan S. (1998) Extracting the relative grain boundary free energy and mobility functions from the geometry of microstructures. Scr. Mater. 38, 531-536.

Adams B.L., Ta'Asan S., Kinderlehrer D., Livshits I., Mason D.E., Wu C., Mullins W.W., Rohrer G.S., Rollett A.D. & Saylor D.M. (1999) Extracting Grain Boundary and Surface Energy from Measurement of Triple Junction Geometry. Interface Science 7, 321-337.

ALAM M., BLACKMAN M. & PASHLEY D. (1954) High-Angle Kikuchi Patterns. Proceedings of the Royal Society of London Series A-Mathematical and Physical Sciences 221, 224-&.

Bastos A., Zaefferer S. & Raabe D. (2008) Three-dimensional EBSD study on the relationship between triple junctions and columnar grains in electrodeposited Co-Ni films. J. Microsc. 230, 487-498.

Blennow P. (2007) Strontium Titanate-based Anodes for Solid Oxide Fuel Cell. Media-Tryck, Lund.

Blennow P., Hansen K.K., Wallenberg L.R. & Mogensen M. (2009) Electrochemical characterization and redox behavior of Nb-doped SrTiO3. Solid State Ionics 180, 63-+.

Blennow P., Hagen A., Hansen K.K., Wallenberg L.R. & Mogensen M. (2008) Defect and electrical transport properties of Nb-doped SrTiO3. Solid State Ionics 179, 2047-2058.

Chou C.T. & Gholinia A. (2010) Elementary facet method for grain boundary plane determination by 3D EBSD. Texture and Anisotropy of Polycrystals Iii 160, 217-222.

Dillon S.J. & Rohrer G.S. (2009) Characterization of the Grain-Boundary Character and Energy Distributions of Yttria Using Automated Serial Sectioning and EBSD in the FIB. J Am Ceram Soc 92, 1580-1585.

Dillon S.J. & Rohrer G.S. (2009) Three-Dimensional FIB-OIM of Ceramic Materials. Applications of Texture Analysis (edited by A.D. Rollett.), pp. 117-124. J. Wiley & Sons, Hoboken, NJ.

Dillon S.J., Helmick L., Miller H.M., Wilson L., Gemman R., Petrova R.V., Barmak K., Rohrer G.S. & Salvador P.A. (2011) The Orientation Distributions of Lines, Surfaces, and Interfaces around Three-Phase Boundaries in Solid Oxide Fuel Cell Cathodes RID A-9804-2008 RID A-9420-2008. J Am Ceram Soc 94, 4045-4051.

Dingley D.J. & Randle V. (1992) Microtexture determination by electron backscatter diffraction. J. Mater. Sci. 27, 4545-4566.

Dingley D.J. & Wright S.I. (2009) Determination of crystal phase from an electron backscatter diffraction pattern. Journal of Applied Crystallography 42, 234-241.

Drouin D., Couture A.R., Joly D., Tastet X., Aimez V. & Gauvin R. (2007) CASINO V2.42 - A fast and easy-to-use modeling tool for scanning electron microscopy and microanalysis users. Scanning 29, 92-101.

Gholinia A., Brough I., Humphreys J., McDonald D. & Bate P. (2010) An investigation of dynamic recrystallisation on Cu-Sn bronze using 3D EBSD. Materials Science and Technology 26, 685-690.

Hattori M., Takeda Y., Sakaki Y., Nakanishi A., Ohara S., Mukai K., Lee J. & Fukui T. (2004) Effect of aging on conductivity of yttria stabilized zirconia. J. Power Sources 126, 23-27.

Helmick L., Dillon S.J., Gerdes K., Gemmen R., Rohrer G.S., Seetharaman S. & Salvador P.A. (2011) Crystallographic Characteristics of Grain Boundaries in Dense Yttria-Stabilized Zirconia RID A-9420-2008. International Journal of Applied Ceramic Technology 8, 1218-1228.

Herring C. (1951) Surface tension as a motivation for sintering. The Physics of Powder Metallurgy. (edited by W.E. KINGSTON.), pp. 143-179. New York.

Humphreys F. & Hatherly M. (2004) Recrystallization and Related Annealing Phenomena. (Anonymous), pp. 121-167. Elsevier.

Jin H., Wu P., Ball M. & Lloyd D. (2005) Three-dimensional texture determination of 6111 aluminium alloy sheet by precise serial sectioning and EBSD measurement RID A-7009-2008. Materials Science and Technology 21, 419-428.

Klemenso T., Chung C., Larsen P. & Mogensen M. (2005) The mechanism behind redox instability of anodes in high-temperature SOFCs RID B-1852-2010. J. Electrochem. Soc. 152, A2186-A2192.

Khorashadizadeh A., Raabe D., Zaefferer S., Rohrer G.S., Rollett A.D. & Winning M. (2011) Five-Parameter Grain Boundary Analysis by 3D EBSD of an Ultra Fine Grained CuZr Alloy Processed by Equal Channel Angular Pressing. Advanced Engineering Materials 13, 237-244.

Khorashadizadeh A., Winning M. & Raabe D. (2008) 3D tomographic EBSD measurements of heavily deformed ultra fine grained Cu-0.17wt%Zr obtained from ECAP. Nanomaterials by Severe Plastic Deformation Iv, Pts 1 and 2 584-586, 434-439.

Konrad J., Zaefferer S. & Raabe D. (2006) Investigation of orientation gradients around a hard Laves particle in a warm-rolled Fe3Al-based alloy using a 3D EBSD-FIB technique RID A-6470-2009. Acta Materialia 54, 1369-1380.

Li J., Dillon S.J. & Rohrer G.S. (2009) Relative grain boundary area and energy distributions in nickel. Acta Materialia 57, 4304-4311.

Lin F.X., Godfrey A., Jensen D.J. & Winther G. (2010) 3D EBSD characterization of deformation structures in commercial purity aluminum RID G-4458-2010. Mater Charact 61, 1203-1210.

Liu T., Raabe D. & Zaefferer S. (2008) A 3D tomographic EBSD analysis of a CVD diamond thin film RID A-6470-2009. Science and Technology of Advanced Materials 9, 035013.

Marina O., Canfield N. & Stevenson J. (2002) Thermal, electrical, and electrocatalytical properties of lanthanum-doped strontium titanate. Solid State Ionics 149, 21-28.

Maitland T. & Sitzman S. (2007) Scanning Microscopy for Nanotechnology [electronic resource]: Techniques and Applications. (edited by W. Zhou and Z.L. Wang.)Physica-Verlag NetLibrary, Incorporated [Distributor], Heidelberg : Boulder. P53

Mateescu N., Ferry M., Xu W. & Cairney J.M. (2007) Some factors affecting EBSD pattern quality of Ga+ ion-milled face centred cubic metal surfaces. Mater. Chem. Phys. 106, 142-148.

Matteson T.L., Schwarz S.W., Houge E.C., Kempshall B.W. & Giannuzzi L.A. (2002) Electron backscattering diffraction investigation of focused ion beam surfaces. J Electron Mater 31, 33-39.

Michael J. & Giannuzzi L. (2007) Improved EBSD Sample Preparation Via Low Energy Ga+ FIB Ion Milling. Microscopy and Microanalysis 13, 926.

Michael J. & Kotula P. (2008) Low Energy Ga+ and Ar+ Ion Milling for Improved EBSD Sample Preparation. Microscopy and Microanalysis 14, 976.

Nishikawa S. & Kikuchi S. (1928) Diffraction of cathode rays by mica. Nature 121, 1019-1020.

Oxford Instruments. (2005) Oxford Instruments INCA Crystal EBSD.

Page K., Kolodiazhnyi T., Proffen T., Cheetham A.K. & Seshadri R. (2008) Local Structural Origins of the Distinct Electronic Properties of Nb-Substituted SrTiO(3) and BaTiO(3) RID C-9726-2009 RID B-3585-2009. Phys. Rev. Lett. 101, 205502.

PAN Y. & ADAMS B. (1994) On the Csl Grain-Boundary Distributions in Polycrystals. Scripta Metallurgica Et Materialia 30, 1055-1060

Pelaz L., Marques L.A. & Barbolla J. (2004) Ion-beam-induced amorphization and recrystallization in silicon. J. Appl. Phys. 96, 5947-5976.

Petrov R., Garcia O.L., Mourino N.S., Kestens L., Bae J.H. & Kang K.B. (2007) Microstructure - Texture related toughness anisotropy of API-X80 pipeline steel characterized by means of 3D-EBSD technique. Recrystallization and Grain Growth III, Pts 1 and 2 558-559, 1429-1434.

Porter D.A. & Easterling K.E. (1992) Phase Transformations in Metals and Alloys. Stanley Thornes.

Randle V. & Engler O. (2000) Introduction to Texture Analysis Macrotexture, Microtexture and Orientation Mapping. CRC Press LLC, N.W.

Rohrer G.S., Holm E.A., Rollett A.D., Foiles S.M., Li J. & Olmsted D.L. (2010) Comparing calculated and measured grain boundary energies in nickel. Acta Materialia 58, 5063-5069.

Rubanov S. & Munroe P.R. (2005) Damage in III-V compounds during focused ion beam milling. Microscopy and Microanalysis 11, 446-455.

S.C. Singhal , K. Kendall. (2003) High-temperature solid oxide fuel cells: Fundamentals, Design and applications. Elsevier Advanced Technology, Oxford.

Saowadee N., Agersted K., & Bowen J.R. (2012) Effects of focused ion beam milling on electron backscatter diffraction patterns in strontium titanate and stabilised zirconia. J. Microsc. (in press)

STEELE B., KELLY I., MIDDLETON H. & RUDKIN R. (1988) Oxidation of Methane in Solid-State Electrochemical Reactors. Solid State Ionics 28, 1547-1552.

Sutton A.P. & Balluffi R.W. (1995) Interfaces in Crystalline Materials. OUP Oxford.

Tsipis E.V. & Kharton V.V. (2008) Electrode materials and reaction mechanisms in solid oxide fuel cells: a brief review. Journal of Solid State Electrochemistry 12, 1367-1391.

Toebbens D.M., Stuesser N., Knorr K., Mayer H.M. & Lampert G. (2001) E9: The new high-resolution neutron powder diffractometer at the Berlin neutron scattering center. Mater. Sci. Forum 378-381, 288-293.

Upmanyu M., Smith R. & Srolovitz D. (1998) Atomistic simulation of curvature driven grain boundary migration. Interface Science 6, 41-58.

Wilkinson A.J. & Dingley D.J. (1991) Quantitative Deformation Studies using Electron Back Scatter Patterns. Acta Metallurgica Et Materialia 39, 3047-3055.

YASHIMA M., SASAKI S., KAKIHANA M., YAMAGUCHI Y., ARASHI H. & YOSHIMURA M. (1994) Oxygen-Induced Structural-Change of the Tetragonal Phase Around the Tetragonal-Cubic Phase-Boundary in Zro2-Yo1.5 Solid-Solutions. Acta Crystallographica Section B-Structural Science 50, 663-672.

Zaafarani N., Raabe D., Singh R., Roters F. & Zaefferer S. (2006) Three-dimensional investigation of the texture and microstructure below a nanoindent in a Cu single crystal using 3D EBSD and crystal plasticity finite element simulations RID A-6470-2009. Acta Materialia 54, 1863-1876.

Zaefferer S., Wright S.I. & Raabe D. (2008) Three-dimensional orientation microscopy in a focused ion beam-scanning electron microscope: A new dimension of microstructure

characterization. Metallurgical and Materials Transactions A-Physical Metallurgy and Materials Science 39A, 374-389.

Ziegler J.F., Ziegler M.D. & Biersack J.P. (2010) SRIM - The stopping and range of ions in matter (2010). Nuclear Instruments & Methods in Physics Research Section B-Beam Interactions with Materials and Atoms 268, 1818-1823.

Appendix

Facets convolution

Convolution of normal vector of a facet *j* is

$$\boldsymbol{n}_{con,j} = \frac{\sum_i A_i \boldsymbol{n}_i}{\sum_i A_i} \quad \text{(a1)}$$

Where A_i is the area of facet *i* covered by the convolution sphere and $\boldsymbol{n}_i$ is the normal vector of the facet *i*. In facet element method grain boundaries are assembled of three type facets that perpendicular to x, y and z direction, omit their normal direction. The following illustrates how to compute the area covering by the convolution sphere of a facet that parallel to the x-plane. For the facets parallel to y and z plane, the area can be computed using the same algorithm but cycle the coordinates from (x,y,z) to (y,z,x) for facets parallel to y-plane and (z,x,y) for facets parallel to z-plane.

Given:

- L_x, L_y, L_z are step size along x y and z direction.
- (x_j, y_j, z_j) is at the centre of facet *j* and is the central coordinates of the convolution sphere
- (x_i, y_i, z_i) is the centre of the facet *i* which to be calculate the covering area
- A_i is the area of facet *i* covering by the convolution sphere
- R_c is the radius of convolution sphere

On the plane of facet *i* divided the plan into 4 quarters origins at the centre of the facet *i*. Given #1 #2 #3 and #4 are the vertices of the facet *i* in quarter 1 2 3 and 4 respectively, see figure A1. Coordinates of the vertices in sample coordinate are

$$\#1 = \left(x_i, y_i + \frac{L_y}{2}, z_i + \frac{L_z}{2}\right) \quad \text{(a2)}$$

$$\#2 = \left(x_i, y_i - \frac{L_y}{2}, z_i + \frac{L_z}{2}\right) \quad \text{(a3)}$$

$$\#3 = \left(x_i, y_i - \frac{L_y}{2}, z_i - \frac{L_z}{2}\right) \quad \text{(a4)}$$

$$\#4 = \left(x_i, y_i + \frac{L_y}{2}, z_i - \frac{L_z}{2}\right) \quad \text{(a5)}$$

Four vectors point from centre of the convolution sphere (facet *j*), as shown in figure A2, to the four vertices of facet *i* are

$$\boldsymbol{V_1} = \left(x_i - x_j\right)\hat{\boldsymbol{i}} + \left(y_i + \frac{L_y}{2} - y_j\right)\hat{\boldsymbol{j}} + \left(z_i + \frac{L_z}{2} - z_j\right)\hat{\boldsymbol{k}} \quad \text{(a6)}$$

$$\boldsymbol{V_2} = \left(x_i - x_j\right)\hat{\boldsymbol{\imath}} + \left(y_i - \frac{L_y}{2} - y_j\right)\hat{\boldsymbol{\jmath}} + \left(z_i + \frac{L_z}{2} - z_j\right)\hat{\boldsymbol{k}} \quad \text{(a7)}$$

$$\boldsymbol{V_3} = \left(x_i - x_j\right)\hat{\boldsymbol{\imath}} + \left(y_i - \frac{L_y}{2} - y_j\right)\hat{\boldsymbol{\jmath}} + \left(z_i - \frac{L_z}{2} - z_j\right)\hat{\boldsymbol{k}} \quad \text{(a8)}$$

$$\boldsymbol{V_4} = \left(x_i - x_j\right)\hat{\boldsymbol{\imath}} + \left(y_i + \frac{L_y}{2} + y_j\right)\hat{\boldsymbol{\jmath}} + \left(z_i - \frac{L_z}{2} - z_j\right)\hat{\boldsymbol{k}} \quad \text{(a9)}$$

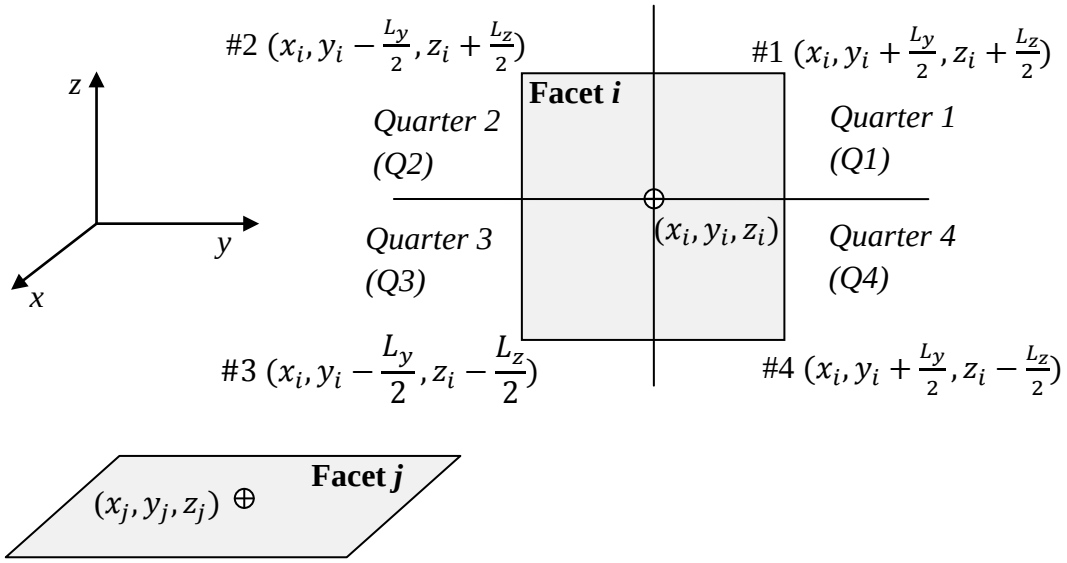

Figure A1 diagram shows the four vertices of the facet *i* and their coordinates.

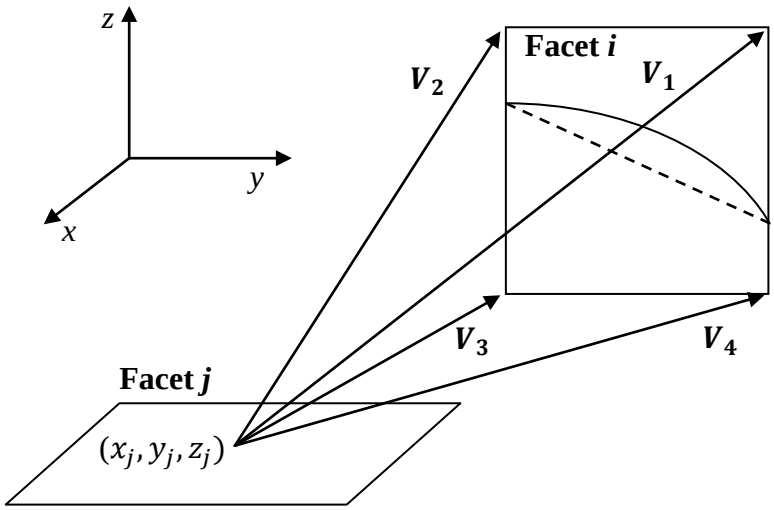

Figure A2 diagram shows the four vectors from centre of the convolution sphere (facet *j*) to the four vertices of a facet *i*.

To compute the area A_i it needs to check if any vertex of the facet *i* is in or out off the convolution sphere. This can be done by compare magnitude of the vectors $\boldsymbol{V_1}$ - $\boldsymbol{V_4}$ to the radius of the convolution sphere as following.

If $|\boldsymbol{V_1}| \leq R_c$ then vertex #1 is in the convolution sphere

If $|\boldsymbol{V_2}| \leq R_c$ then vertex #2 is in the convolution sphere

If $|\boldsymbol{V_3}| \leq R_c$ then vertex #3 is in the convolution sphere

If $|\boldsymbol{V_4}| \leq R_c$ then vertex #4 is in the convolution sphere

In figure A2, the arc on the facet *i* is the intersection line of the convolution sphere and the facet *i*. Assume that radius of the convolution sphere is large enough then the arc is estimated to be a straight line (the dash line in figure A2). Thus the resulting area is an under estimation of the true area and it will yield more error when the convolution sphere getting smaller. Figure A3 shows the area of facet *i* covering by the convolution sphere and two auxiliary vectors ($\boldsymbol{r_1}$ and $\boldsymbol{r_2}$) pointing from the centre of the convolution sphere to the intersection points of the facet sides and the convolution sphere. Magnitude of the vectors $\boldsymbol{r_1}$ and $\boldsymbol{r_2}$ is R_c since they point from the centre of the convolution sphere to the intersection points. Given y_1 y_2 z_1 and z_2 are the lengths shown in figure A3. The lengths are used to calculate the area A_i and can be compute from the auxiliary vectors and the vertices vectors $\boldsymbol{V_1}$ - $\boldsymbol{V_4}$. For example the length z_1 in the figure A3 can be determined from vector summation relation

$$\boldsymbol{r_2} = \boldsymbol{V_4} + z_1\hat{\boldsymbol{k}}$$

its square of magnitude is $$R_c^2 = {V_{4x}}^2 + {V_{4y}}^2 + (V_{4y} + z_1)^2$$

or $$\sqrt{R_c^2 - {V_{4x}}^2 - {V_{4y}}^2} - V_{4y} = z_1$$

or $$z_1 = \left| V_{4y} - \sqrt{R_c^2 - {V_{4x}}^2 - {V_{4y}}^2} \right|$$

where V_{4x} V_{4y} and V_{4z} are vector components of the vector $\boldsymbol{V_4}$.

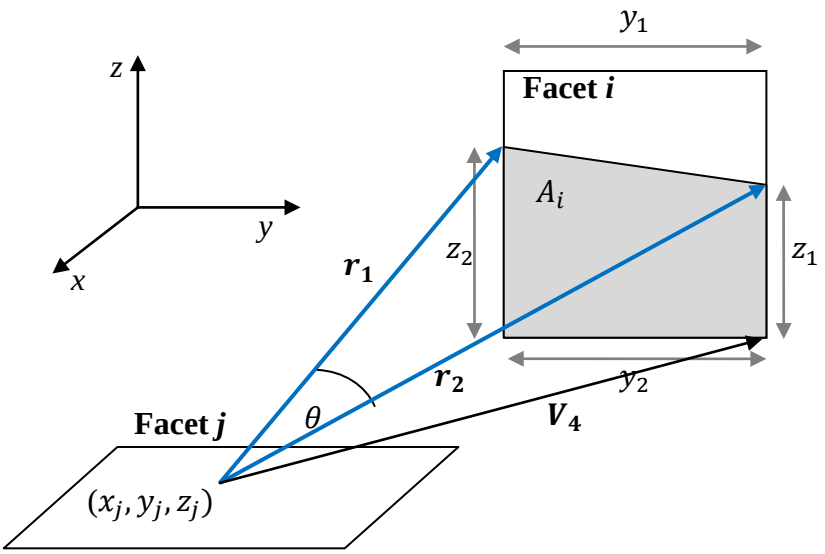

Figure A3 Schematic shows the area A_i and two vectors point from centre of the convolution sphere to the intersection points of the facet sides and the convolution sphere.

For convenient the author uses 1 and 0 to represent the status in and out the convolution sphere of a vetex. For example (1011) means only the vertex #2 is out of the sphere. Table A1 lists all possible case that can be happen and the formula to compute the area A_i of each case.

Table A1 The area A_i for each case of intersection of the convolution sphere and a facet *i*.

case	picture	shape	sides	Area A_i
1111	1 1 1 1	Rectangle		$L_y * L_z$
1110	1 1 1 0	Rectangle - triangle	$y_2 = \left\lvert V_{4y} - \sqrt{R_c^2 - {V_{4x}}^2 - {V_{4z}}^2} \right\rvert$ $z_1 = \left\lvert V_{4z} + \sqrt{R_c^2 - {V_{4x}}^2 - {V_{4y}}^2} \right\rvert$	$L_y * L_z - \frac{y_2 * z_1}{2}$
1101	1 1 0 1	Rectangle - triangle	$y_2 = \left\lvert V_{3y} + \sqrt{R_c^2 - {V_{3x}}^2 - {V_{3z}}^2} \right\rvert$ $z_2 = \left\lvert V_{3z} + \sqrt{R_c^2 - {V_{3x}}^2 - {V_{3y}}^2} \right\rvert$	$L_y * L_z - \frac{y_2 * z_2}{2}$

1100	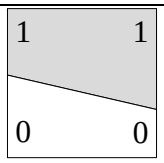	trapezoid	$z_1 = \left\lvert V_{1z} + \sqrt{R_c^2 - {V_{1x}}^2 - {V_{1y}}^2} \right\rvert$ $z_2 = \left\lvert V_{2z} + \sqrt{R_c^2 - {V_{2x}}^2 - {V_{2y}}^2} \right\rvert$	$\frac{L_y * (z_1 + z_2)}{2}$
1011	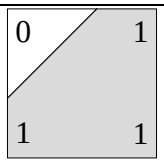	Rectangle - triangle	$y_1 = \left\lvert V_{2y} + \sqrt{R_c^2 - {V_{2x}}^2 - {V_{2z}}^2} \right\rvert$ $z_2 = \left\lvert V_{2z} - \sqrt{R_c^2 - {V_{2x}}^2 - {V_{2y}}^2} \right\rvert$	$L_y * L_z - \frac{y_1 * z_2}{2}$
1010	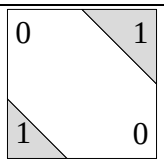			Forbidden case
1001	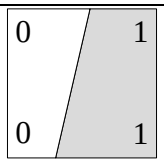	trapezoid	$y_1 = \left\lvert V_{1y} + \sqrt{R_c^2 - {V_{1x}}^2 - {V_{1z}}^2} \right\rvert$ $y_2 = \left\lvert V_{4y} + \sqrt{R_c^2 - {V_{4x}}^2 - {V_{4z}}^2} \right\rvert$	$\frac{L_z * (y_1 + y_2)}{2}$
1000	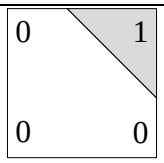	triangle	$y_1 = \left\lvert V_{1y} + \sqrt{R_c^2 - {V_{1x}}^2 - {V_{1z}}^2} \right\rvert$ $z_1 = \left\lvert V_{1z} + \sqrt{R_c^2 - {V_{1x}}^2 - {V_{1y}}^2} \right\rvert$	$\frac{y_1 * z_1}{2}$
0111	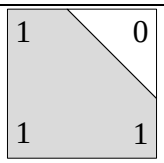	Rectangle - triangle	$y_1 = \left\lvert V_{1y} - \sqrt{R_c^2 - {V_{1x}}^2 - {V_{1z}}^2} \right\rvert$ $z_1 = \left\lvert V_{1z} - \sqrt{R_c^2 - {V_{1x}}^2 - {V_{1y}}^2} \right\rvert$	$L_y * L_z - \frac{y_1 * z_1}{2}$
0110	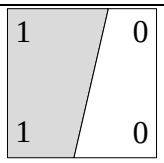	trapezoid	$y_1 = \left\lvert V_{2y} - \sqrt{R_c^2 - {V_{2x}}^2 - {V_{2z}}^2} \right\rvert$ $y_2 = \left\lvert V_{3y} - \sqrt{R_c^2 - {V_{3x}}^2 - {V_{3z}}^2} \right\rvert$	$\frac{L_z * (y_1 + y_2)}{2}$
0101	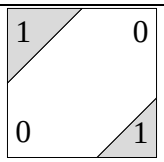			Forbidden case
0100	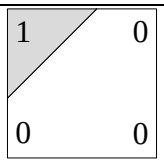	triangle	$y_1 = \left\lvert V_{2y} - \sqrt{R_c^2 - {V_{2x}}^2 - {V_{2z}}^2} \right\rvert$ $z_2 = \left\lvert V_{2z} + \sqrt{R_c^2 - {V_{2x}}^2 - {V_{2y}}^2} \right\rvert$	$\frac{y_1 * z_2}{2}$
0011	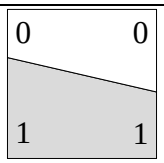	trapezoid	$z_1 = \left\lvert V_{4z} - \sqrt{R_c^2 - {V_{4x}}^2 - {V_{4y}}^2} \right\rvert$ $z_2 = \left\lvert V_{3z} - \sqrt{R_c^2 - {V_{3x}}^2 - {V_{3y}}^2} \right\rvert$	$\frac{L_y * (z_1 + z_2)}{2}$

0010	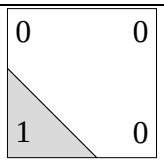	triangle	$y_2 = \left\lvert V_{3y} - \sqrt{R_c^2 - {V_{3x}}^2 - {V_{3z}}^2} \right\rvert$ $z_2 = \left\lvert V_{3z} - \sqrt{R_c^2 - {V_{3x}}^2 - {V_{3y}}^2} \right\rvert$	$\frac{y_2 * z_2}{2}$
0001	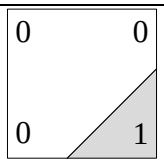	triangle	$y_2 = \left\lvert V_{4y} + \sqrt{R_c^2 - {V_{4x}}^2 - {V_{4z}}^2} \right\rvert$ $z_1 = \left\lvert V_{4z} - \sqrt{R_c^2 - {V_{4x}}^2 - {V_{4y}}^2} \right\rvert$	$\frac{y_2 * z_1}{2}$
0000	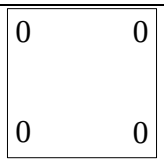	Off the convolution sphere		0